Fabrication and Characterization of Metal-support for Solid Oxide Fuel Cells (MSOFCs)

By

Kyung Sil Chung

A thesis
presented to the University of Waterloo
in fulfillment of the
thesis requirement for the degree of
Master of Applied Science
in
Chemical Engineering

Waterloo, Ontario, Canada, 2016

Author's Declaration

I hereby declare that I am the sole author of this thesis. This is a true copy of the thesis, including any required final revisions, as accepted by my examiners.

I understand that my thesis may be made electronically available to the public.

Abstract

Solid oxide fuel cells (SOFCs) can generate electricity with higher efficiency and reduced carbon emissions compared with conventional power generation systems. Unlike many other fuel cells, SOFCs are beneficial in terms of utilizing not only expensive hydrogen gases but also syngas and hydrocarbons. This flexibility in fuel options is one of the advantageous aspects that SOFC has over the other fuel cells. However, current research is challenged with reducing the operating temperature and finding more cost effect of ways of fabricating SOFCs. In order to widespread commercialization the high cost and stability issues associated with high temperature operation must be overcome. To address these issues, researches have aimed at reducing the operating temperature of SOFC. One option is to use alternative ceramic materials, by replacing conventional Yttria Stabilized Zirconia (YSZ) with materials possessing higher ionic conductivities at lower temperatures (e.g. 600-800°C), such as Samarium Doped Ceria (SDC). This is a critical step since reducing the operating temperature below 700°C allows the use of metal-supported cells. Use of porous metal-support made with stainless steel can provide benefits including increased durability, reduced cost, higher oxidation resistance, and tolerance to thermal resistance. This new generation of SOFC with metal as a support structure is called metal-supported solid oxide fuel cell (MSOFC). The porous metal support must satisfy several requirements: it must be porous enough (~20-40% porosity) to provide gas diffusion pathways, able to operate at high operating temperatures (600-800°C) without oxidation, and match the coefficient of thermal expansion (CTE) with that of ceramic materials (YSZ and SDC have CTE of 10-12 ppm K^{-1}). In this thesis, the main objectives are 1) to determine suitable fabrication methods for the porous metal support and 2) characterize the fabricated metal-support with various parameters to provide guidelines for determining compatible metal supports for MSOFC. The stainless steel 400 series satisfies the above requirement and in this thesis, SS430L (d_{50} = 44 µm) was chosen as support materials. The porous metal support is fabricated using various precursor formulations; such formulations comprise metal support powder (SS430L), plasticizer (DOP), pore former (PMMA), binder (PVB) and solvent (ethanol). Beside the precursor formulation, the sintering process is also critical. The sintering temperature profile was determined through thermogravimetric analysis (TGA) of individual components. The sintered porous metal support was characterized for oxidation resistance, porosity measurements, CTE

measurements, electronic conductivity, and SEM imaging. Correlations between precursor formulation, sintering results, the relative densities, porosities, and CTEs were established. These measurements can provide guidelines to fabricate compatible metal support for MSOFC.

Acknowledgements

I would like to express the deepest gratitude to my professor and a mentor Professor Eric Croiset. Thank you so much for your guidance, support, and help. It was a great experience studying and learning under your mentorship. Also I would like to thank my co-researcher and a PhD candidate Sannan Toor for his kind support and assistance throughout my studies. It was my pleasure to work in our SOFC research team and I truly appreciate all the great experiences and knowledge I have gained. I would like to thank Mark Whitney from the Mechanical engineering department for helping me with experiments. Your aid for equipment operation and data analysis provided a lot of valuable insights to my research.

I would also like to thank my parents and my sister for their unconditional love and support. With their love and blessing I was able to overcome hardships and difficult times in my life. My family has shown me what true love is and their continuous encouragements enabled me to accomplish my dream. Thank you Mom, Dad, and my beloved sister Eun Sil!

Last but not least, I want to thank my friends in Waterloo. You guys have gifted me with beautiful memories and I will always cherish our dearest friendships.

Table of Contents

List of Figures

List of Tables

Chapter 1 Introduction

Fuel cells are energy conversion devices that can generate electricity directly from fuels and oxygen through electrochemical reactions (Li, 2006). Unlike traditional power generation systems, fuel cells can convert chemical energy directly into electricity and therefore offer many advantages including improved efficiency, various fuel options for some fuel cells, and lower environmental impact (Clemmer, 2006).

There are few different types of fuel cells that are under commercialization and research and development stages. The present study focuses on one particular type of fuel cell which is solid oxide fuel cell (SOFC) and more specifically metal-supported solid oxide fuel cell (MSOFC). Solid oxide fuel cell is made of solid ceramics layers. In a conventional SOFC, the electrolyte is made of high temperature ionic conducting ceramic material known as yttrium-stabilized zirconia (YSZ). The anode component is usually made with a combination of YSZ and nickel as electrochemical catalyst. Common cathode materials include lanthanum strontium manganite (LSM), lanthanum strontium cobalt ferrite $La_{1-x}Sr_xCo_{1-y}Fe_yO_{3-\delta}$ (LSCF), and lanthanum strontium gallium magnesium oxide (LSGM). SOFC requires hydrogen and internally (or externally) reformed hydrocarbons as a fuel on the anode side and air as oxidant on cathode side to generate electricity.

SOFC has one of the highest operating temperatures ranging between 800°C-1000°C with conventional ceramic-supported designs including electrolyte supported cell (ECS), anode supported cell (ACS), and cathode supported cell (CSC). The main reason why SOFC requires such a high operating temperature is due to low ionic conductivity of the electrolyte at lower temperatures. YSZ can only provide sufficient oxide transfer (ionic conduction) at high temperatures such as 0.02S/cm at 800°C and 0.1S/cm at 1000°C. In addition, in an SOFC, because of the high operating temperature, the electorcatalyst is typically nickel, which is not poisoned by CO. This implies that, unlike other fuel cells, SOFC can operate on fuels other than pure hydrogen. Also, because nickel is a good reforming catalyst, it is possible for some hydrocarbon or alcohol fuels to undergo internal reforming. Having various fuel options is a

unique advantage that SOFC has. However, this high operating temperature brings many challenges regarding available choice of materials for SOFC and durability issues.

Recent research trends have focused on lowering the operating temperatures down to 650°C-850°C (intermediate temperature SOFC) and even further to 550°C-650°C (low –temperature SOFC). Lowered operating temperature enables the use of stronger and cheaper material such as metal as a support structure. This new design is called metal-supported solid oxide fuel cells (MSOFC) and this thesis focuses on the characterization and fabrication of the metal support layer. The use of metal shows promising benefits including reduced cost, increased mechanical strength and durability, higher tolerance to mechanical loading, thermal shock, and redox tolerance. Detailed advantages and new fabrication challenges in incorporating metal supports into conventional SOFC designs is delineated in Chapter 2, Literature Review.

1.1 Basic Principles of Solid Oxide Fuel Cells

The basic operation of an SOFC is illustrated in Figure 1.1. From the cathode side, the air as oxidant enters and reacts with electron from the external circuit to form oxide ions. The oxide ions travel through the electrolyte to reach anode sites. At the anode the fuel (e.g. hydrogen gas) reacts with oxide ions to form water and release electrons. Then, these electrons travel through the external circuit to reach the cathode, hence completing the cycle. While these electrons pass through the external circuit, they do work to the electric load thus forming the electric power output.

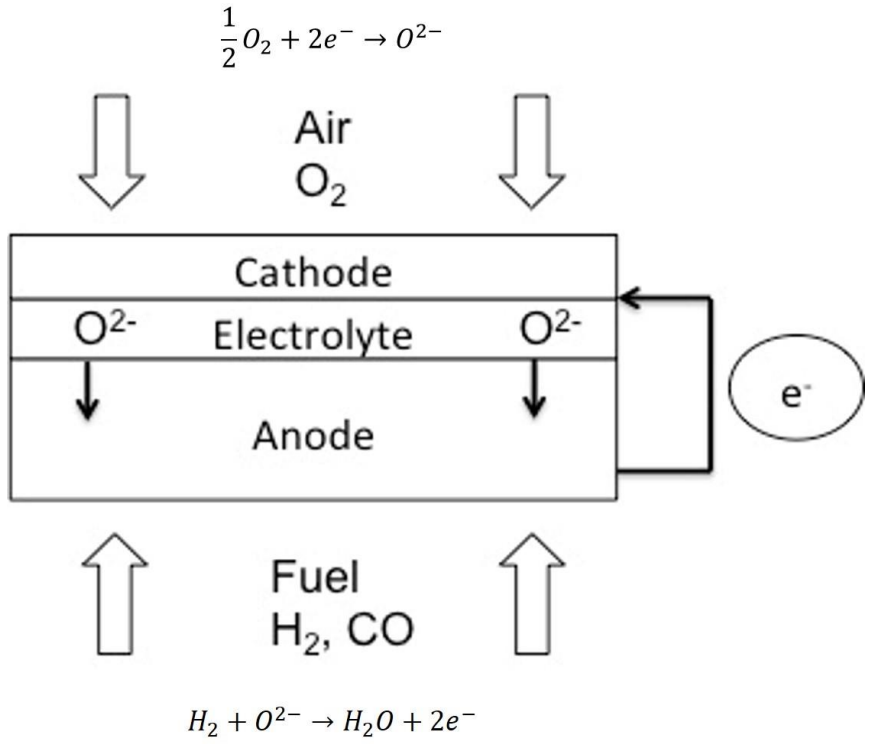

Figure 1-1 Schematic of solid oxide fuel cell illustrating its operational principle.

The overall electrochemical reaction occurring at each electrode can be written as follows

At the cathode:

$$\frac{1}{2}O_2 + 2e^- \rightarrow O^{2-} \tag{1.1}$$

and at the anode

$$H_2 + O^{2-} \rightarrow H_2O + 2e^- \tag{1.2}$$

so that the overall reaction is given by

$$\frac{1}{2}O_2 + H_2 \rightarrow H_2O + Waste\ Heat + Electric\ Energy \tag{1.3}$$

If carbon monoxide is present at the anode site, the following anode reaction occurs

$$CO + O^{2-} \rightarrow CO_2 + 2e^- \tag{1.4}$$

The cathode side reaction stays the same as given in Equation (1.1). Then the overall reaction becomes

$$CO + \frac{1}{2}O_2 \rightarrow CO_2 + Waste\ Heat + Electric\ Energy \quad (1.5)$$

As seen in Equation (1.5), carbon monoxide can be utilized directly as a fuel for electrochemical reaction whereas it requires additional fuel processing in other types of fuel cells like molten carbonate fuel cell. SOFC has wide range of fuel options including coal-derived gases or reformed natural gases that both contain hydrogen and carbon monoxide. For "a" moles of hydrogen and "b" moles of carbon monoxide, the combined anode reaction can be written as

$$aH_2 + bCO + (a+b)O^{2-} \rightarrow aH_2O + bCO_2 + 2(a+b)e^- \quad (1.6)$$

and the combined cathode reaction is

$$\frac{1}{2}(a+b)O_2 + 2(a+b)e^- \rightarrow (a+b)O^{2-} \quad (1.7)$$

Consequently, the combine overall reaction can be shown as

$$\frac{1}{2}(a+b)O_2 + aH_2 + bCO \rightarrow aH_2O + bCO_2 + Waste\ Heat + Electric\ Energy \quad (1.8)$$

In SOFC operation, the cathode and anode electrode reactions occur at the triple phase boundary (TBP) between the electrode, electrolyte, and void space. This requires the electrode to be both electronically and ionically conductive which is known as mixed conducting electrodes. The literature review in the next chapter describes recent development on materials for electrolyte, anode, and cathode regarding the electrochemical properties.

1.2 Metal-supported Solid Oxide Fuel Cells Structures

The basic structure of a solid oxide fuel cell consists of a solid electrolyte, and two electrodes called anode and cathode. Since all the cell components are made of solid materials the design of SOFC can be made into three main structures: tubular, monolithic, and planar. In this study only planar design is considered and discussed since the fabrication method used in this thesis is that

of planar design. Planar cells are also referred to flat-plate design which has a simple geometry and present fabrication flexibility. A single cell model using planar design is shown in Figure 1.2.

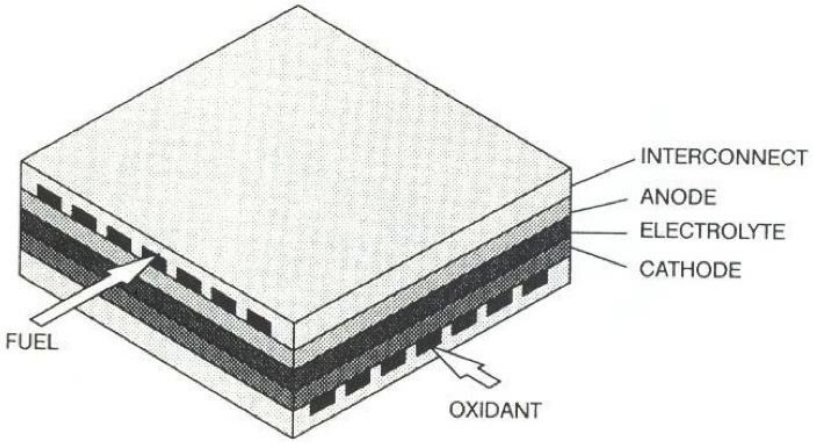

Figure 1-2 Planar SOFC structure (Nguyen & Takahashi, 1995)

The planar cell structure stacks up flat anode, electrolyte and cathode with interconnects. Advantages of planar design include lower fabrication cost, ease in flow arrangements, and higher power density compared to tubular and monolithic designs. On the other hand, disadvantages include requirement for high-temperature gas-tight sealing, high assembly effort and cost, stricter requirement on thermal expansion match (Li, 2006). Based on the planar design, there are three main types of conventional SOFC designs, as shown in Figure 1.3, depending on which layer is the supporting one (i.e. which one is thickest).

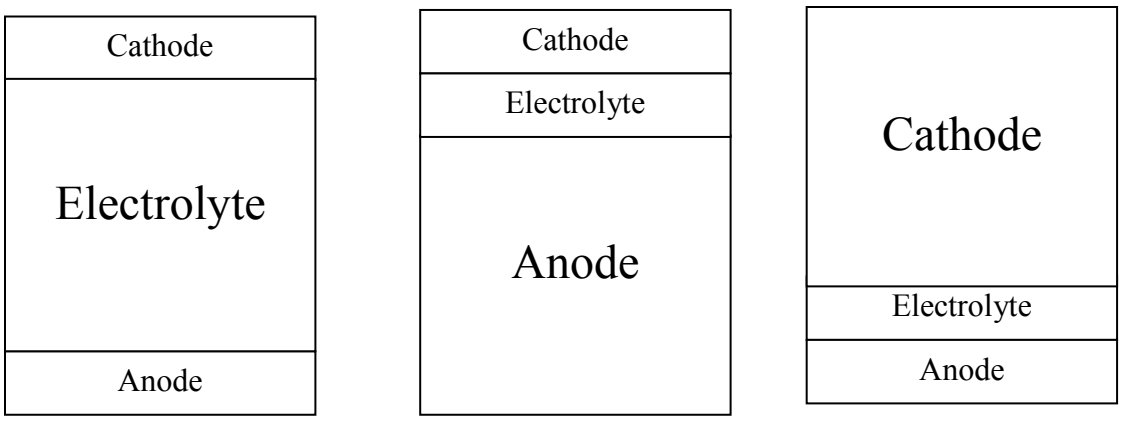

a. Electrolyte-supported cell (ESC) b. Anode-supported cell (ASC) c. Cathode-supported cell (CSC)

Figure 1-3 Conventional SOFC designs

ESCs are used for high-temperature SOFCs and both ACS and CSC are developed for lower temperature SOFCs. The thick electrolyte layer in the ESC structure causes high ohmic overpotential due to the high resistance of the oxide ion transport through the thick electrolyte. In an effort to reduce ohmic resistance, anode and cathode supported cells are developed with thicker electrode and thin electrolyte. However, similar results of high resistance to mass transport through the porous electrode lead to large concentration overpotential. Furthermore, the use of expensive and brittle ceramic as a support material is both not cost effective and not mechanically reliable. Thus, with the use of lower operating temperature, materials such as metal can be also used for cell structure. This way, metal can replace the support structure with cheaper cost and enhanced strength. The structure transition from ACS to MSOFC is shown in Figure 1.4.

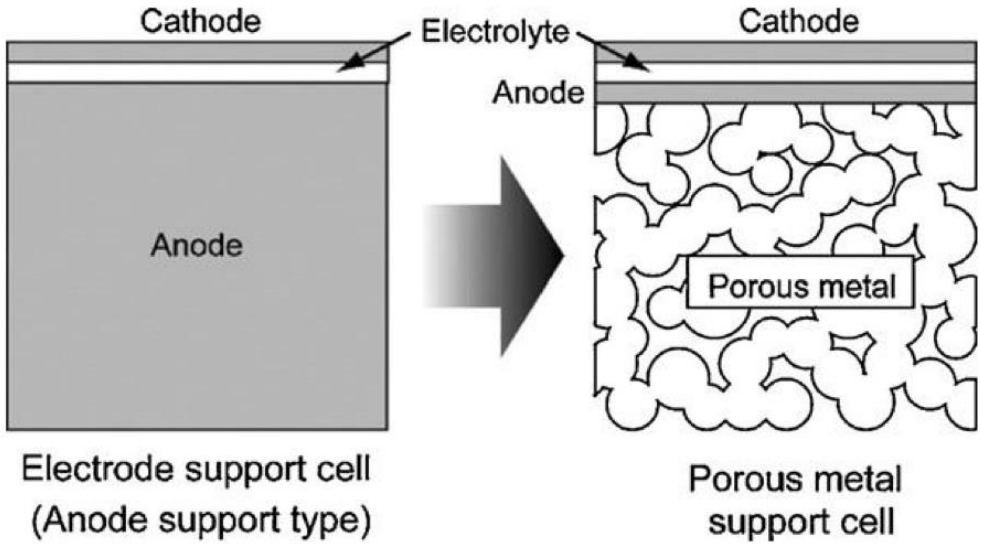

Figure 1-4 Schematic representation of anode-supported cell (ACS) and metal-supported cell (MSOFC) (Tucker, 2010).

As seen in Figure 1.4. MSOFC design requires only thin layers of anode, electrolyte, and cathode while the support is provided by much stronger and cheaper porous metal substrate. This design enables to save material usage of expensive ceramics to only the necessary portion and thus reducing the cost. Also porous metal is mechanically stronger and less susceptible to material handling and manufacturing process. Application of metal support shows various benefits as well as new challenges in the fabrication process. In the next chapter, literature review of recent MSOFC development is discussed regarding characteristics, material choices, and fabrication methods.

1.3 Research Objective

In this study, the main focus is on the fabrication and characterization of the metal support layer. Use of metal support layer into SOFC can provide increased durability, reduced cost, and tolerance to thermal resistance. In order to deliver these benefits, the porous metal support must satisfy several requirements: it must be porous enough (~20-40% porosity) to provide gas diffusion pathways, able to operate at high operating temperatures without severe oxidation, and match the coefficient of thermal expansion (CTE) with that of ceramic materials (YSZ and Samarium Doped-Ceria (SDC) have CTE of 10-12 ppm K^{-1}). Since stainless steel is susceptible to high temperature oxidation, low to intermediate temperature ranges are used for MSOFC

applications. For this temperature range, an alternative mixed ionic conductor, SDC can be used as an electrolyte material since it has higher ionic conductivity at lower temperature than YSZ. It was reported that the conductivity of SDC at 750˚C is similar to that of YSZ at 1000˚C (Toor & Croiset, 2015). The current challenge in this research is to find compatible and economical fabrication methods that satisfy all the mentioned criteria. Stainless steel powder, SS430L (d50=44μm) (Alfa Aesar) was chosen as the base metal supports material. The metal support layer is composed of SS430L and organics including pore former (poly methyl methacrylate (PMMA)), binder (polyvinyl butyral (PVB)), and plasticizer (di(n-octyl)amine,(DOP)). The porous metal support was fabricated using conventional powder metallurgy with die pressing. Details about the fabrication process are described in the experimental section of this thesis. The objective of this research is to assess the overall fabrication process and characterize parameters such as sintering profile, porosity, and CTE values. This research is expected to contribute towards a better understanding and improvement of the fabrication process for metal support to be used with intermediate temperature MSOFCs.

Chapter 2 Literature Review

2.1 Introduction to Metal-supported Solid Oxide Fuel Cells

Solid oxide fuel cell is a type of fuel cell composed of all solid ceramic components including anode, electrolyte, and cathode. It uses fuels on the anode side and oxidant on the cathode side to convert chemical energy directly into electrical energy with reduced intermediate steps compared to conventional power generations and therefore producing energy with much higher efficiency, up to 50-65% (Li, 2006). It has one of the highest operating temperatures, between 800°C-1000°C. Such high operating temperature exhibits benefits as well as disadvantages. One of the advantages, as mentioned in the Introduction section, is the fuel flexibility for SOFC and the possibility of internal reforming. The absence of extensive fuel processing can save up energy with better balance of plant. The reason for fuel flexibility is the high operating temperature that can provide sufficiently fast electrochemical kinetics at the electrodes without the need of noble metals as catalysts and with low activation polarization. Nickel is a typical electrocatalyst used in SOFC, which is not poisoned by carbon monoxide and which is also an excellent reforming catalyst. However, despite the aforementioned advantages, such high operating temperatures create significant limits as to the choice of materials that can be used as the cell components. The main reason for the solid oxide fuel cell to require such high temperature is because of the electrolyte material that can only conduct oxide ions sufficiently at high temperatures. The common material for such electrolyte is yittrium-stablized zirconia known as YSZ (As mentioned previously, YSZ has ionic conductivity of 0.1S/cm at 1000°C and 0.02S/cm at 800°C). Research and development focuses on reducing the operating temperatures to 650°C-850°C (intermediate temperature SOFC) and even further to 550°C-650°C (low temperature SOFC). One option to lower the operating temperature is to change the cell structures. The fist conventional SOFC design was electrolyte supported cell (ECS) where the electrolyte layer was fabricated as the thickest layer to provide mechanical support. However thick electrolyte combined with high ohmic resistance requires high temperatures around 1000°C to overcome the ohmic loses. The next conventional SOFC designs are anode supported cells (ACS) and cathode supported cells (CSC). These designs use thick electrodes and thin electrolyte to decrease the ohmic resistance within the electrolyte. However, even the use of thin YSZ still circumvents lowering of the temperature below 800°C to maintain adequate ionic conductivity. Additionally,

the use of expensive ceramics as a support material is not cost effective. Furthermore, the use of ceramic materials as a support shows poor mechanical durability and stability upon harsh operating conditions and fabrication process. In order to lower the operating temperature to 550°C-800°C range new materials for electrolyte have been suggested which possess higher ionic conductivity at lower temperatures (550°C-800°C). Ceria-based electrolytes are such materials, which can be used in their stable form as samarium-doped ceria (SDC), and gadolinium-doped ceria (GDC or CGO). Conductivity of SDC and CGO at 750°C is ~0.08S/cm which is similar to that of YSZ at 1000°C (Toor & Croiset, 2015). As mentioned before all ESC, ASC, and CSC are brittle and use extra quantity of expensive ceramics. Ferritic stainless steel alloys can be used instead as a support material to replace the brittle and expensive ceramics. This new design is called metal-supported solid oxide fuel cells (MSOFCs). MSOFC has a number of advantages over the conventional designs (ESC, ASC, and CSC). First, it minimizes the use of expensive ceramics to functionality only and keeps the thickness only necessary for the electrochemical reactions. This results in both saving of the materials and increase in performance due to reduced ohmic resistance. Second, stainless steels and similar ferritic alloys show much higher strength and durability upon harsh operating conditions. Stainless steel can withstand rapid thermal cycling, mechanical stress, and redox cycling. The better strength of metal supported cells is beneficial to applications where the cell or stack can experience vibration, mechanical loading, and thermal shock. This enhanced ruggedness can also improve the manufacturing process as cells can handle more mechanical loading (Tucker, 2010).

2.2 Choice of Materials for Metal Support Layer

Most commonly used materials for metal support in SOFC application are ferritic stainless steels due to their high temperature oxidation resistance and relatively close match of the coefficient of thermal expansion (CTE) values with that of the SOFC ceramic materials. Ferritic stainless steel alloy 400 series is one of the most widely used materials for the metal support application. The types included are 430, 410, 409, and 441 (Tucker, 2010). As seen in Table 2-1. 400 series show good oxidation resistance and close CTE values with YSZ, CGO, and SDC materials. Stainless steel 400 series contain mainly iron and 10-26wt% of chromium to form a continuous chromia scale that can prevent iron oxidation (Tucker, 2010).

Table 2-1 Summary of material information (Tucker, 2010)

Metal	**CTE ($ppmK^{-1}$)**	**Cost ($/kg 2009)**	**Relative oxidation resistance**
NiCrAlY	15-16	63	Excellent
Hastelloy-X	15.5-16	22	Excellent
Ni	16.5	18	None
Ni-Fe (1:1)	13.7	9	None
300-Series stainless steel	18-20	2	Poor
400-Series stainless steel	10-12	2	Very good
YSZ, CGO, LSGM	10-12	305, 1475, 765 (FuelCellMaterials, 2016)	Not available
SDC (FuelCellMaterials)	12.7	1475 (FuelCellMaterials, 2016)	Not available

However a build-up of chromia scale can cause formation of brittle oxide phase and poor electronic conductive layers. Even though chromia scale is beneficial for preventing oxidation, it can also cause reduction of electronic conductivity and buildup of mechanical stress which are not ideal for metal support applications. Thus the chromium content is one of the important parameters to be considered when choosing appropriate metal support materials. Stainless steel 300 series were studied as potential candidates for MSOFC application as well. In the 300 series the chromium content is in the 18-30wt% range and nickel in the 6-20% range. However, based on Table 2.1, stainless steel 300-series shows poor oxidation resistance compared to 400-series and also a poor match of CTE values to that of electrolyte materials. This indicates that the 400 series is currently the most appropriate base metal material for MSOFC application.

Addition of specific elements to ferritic alloys can enhance certain properties. Alloys often include Ni, Mo, Si, Ti and Al. Addition of Ni can be beneficial for better CTE match since anode of the SOFC is commonly made with Ni and YSZ composites. In fact, few groups use Ni-alloys as a metal support to investigate material properties and potential for SOFC applications.

Research group from the Institute of Nuclear Energy Research in Taiwan reported the development of a novel metal substrate using porous Ni-Mo metal support (Hwang et al., 2016; Yang et al., 2015). Molybdenum (Mo)-containing nickel (Ni) based porous alloy was fabricated using powder metallurgy with different area densities of straight gas flow channels to improve hydrogen fuel gas and the water byproduct diffusion in the anode and supporting substrate. The power densities at 0.8V and 750°C was 1,161 mW/cm^{-2} which is quite a promising performance (Hwang et al., 2016). Research group from Gdansk University of Technology in Poland has reported on using IN625 alloys (Ni22Cr) and P1600 (Ni:Cr:Fe=74:16:9 wt%) for metal support SOFC applications. High temperature corrosion resistance of these materials were studied with addition of the yttrium containing precursor to further reduce the corrosion rate so that the lifetime of the infiltrated alloy can be greatly extended (Karczewski et al., 2015; Molin et al., 2011). However, there are also disadvantages of using Ni including the high cost of Ni, poor CTE match to the electrolyte, and low redox tolerance (Tucker, 2010). Additionally, low oxygen partial pressure atmosphere is required for the sintering process in order to prevent Ni coarsening and agglomeration. When Ni is coarsened and agglomerated this reduces both the triple phase boundary length and Ni-particle connectivity when used as cermet (metal +ceramic) layer to perform anode functionality as well (Knibbe et al., 2013).

Addition of Al to Fe-alloys can improve the oxidation resistance by forming protective alumina oxide Al_2O_3 similar to chromia scale Cr_2O_3. A Fe21Cr7Al1Mo0.5Y alumina-forming stainless steel was designed and evaluated as a material for porous supports for oxygen transport membranes for electrochemical device application by Riso DTU Energy Conversion (Glasscock et al., 2013). It was found that FeCrAl steel showed vastly superior oxidation resistance compared with a FeCr steel of similar composition and porosity. Oxidation of metal support with 20-40% porosity at 850°C and oxygen partial pressure of 10^{-11} kPa showed sub-parabolic kinetics and stability over 3000h. It was presented that Fe21Cr7Ml1Mo0.5Y has desirable properties and is a potential material to be used as porous metal support for electrochemical devices (Glasscock et al., 2013). Addition of Si can improve adhesion of chromia scale to the surface of the steel by forming SiO_2 between the scale and bulk. From Jablonski & Sears, (2013) the detailed behavior of SiO_2 subscale was studied on 430-type stainless steel. It was reported

that even at very low Si content of 0.017wt% can start to form a Si-rich subscale between chromia scale and the metallic substrate during oxidation at high temperature (800°C). Despite the improved oxidation resistance, these metal oxides are electronically non-conductive and buildup of such scale can significantly compromise performance. Overall it was found that the amount of Cr should not exceed more than 26t wt% and the content of Al, and Si needs to be minimized to prevent excessive formation of electronically insulating layers. It is obvious that fine tailoring of special elements is required to optimize the material properties specific to MSOFC application. For all the aforementioned reasons, stainless steel 400 series is the most common choice of metal-support for the MSOFCs (Tucker, 2010). Based on these results special FeCr alloys were developed to further improve CTE match and oxidation resistance. Fe-Cr-Mn alloy (Fe as base element, 22 wt% Cr, 0.4 wt% Mn) was used as the porous metal support at Riso DTU with their unconventional anode structures to avoid high temperature Ni agglomeration and interdiffusion of Fe, Cr, and Ni (Blennow et al., 2011). Special alloy developed by Plansee SE Austria is the ODS (oxide dispersive strengthened) Ferritic FeCr-alloy ITM Fe-26Cr-(Mo, Ti, Y2O3). This material was used to form porous metallic substrate by powder metallurgy and known to provide the required long-term corrosion stability. Again the oxidation resistance is provided by the formation of well adherent protective oxide scale during cell operation and such characteristics can increase both the corrosion stability and creep resistance(Franco et al., 2009). Special metal alloy Crofer® 22APU by ThyssenKrupp VDM GmbH (under license from Froschungszentrum Julich) is a high temperature ferritic stainless steel especially developed for application in solid oxide fuel cells. At temperatures up to 900°C a chromium-manganese oxide layer is formed on the surface of Crofer® 22APU which is thermodynamically very stable and possesses high electrical conductivity. The low coefficient of thermal expansion is matched to that of ceramics typically used for high-temperature fuel cells in the range from room temperature to 900 °C. This material is characterized by excellent corrosion resistance, low rate of chromium vaporization, ease of processing, low coefficient of thermal expansion, and good electrical conductivity of the oxide layers. Chemical composition is the following: Fe:Cr:C:Mn:Si:Cu:Al:S:P:Ti:La=bal:24:0.03:0.8:0.5:0.5:0.5:0.02:0.05:0.2:0.2 (VDM materials Material Data Sheet, 2010). This material was used to from a novel design, alternative to the conventional MSOFC, honeycomb microstructure metal supported solid oxide fuel cells (Fernández-González et al., 2014). Use of this special alloy showed easy processing and good

performance. Hastelloy-X is another metal alloy that can be used for the MSOFC application. It has higher CTE than the ceramic layers of the SOFC but shows excellent oxidation resistance. National Research Council of Canada has reported on use of Hastelloy-X as the metal support with plasma thermal spray deposition techniques to apply ceramic layers on top. This method can prevent oxidation of the metallic substrate during the fabrication process. The detailed fabrication approach will be discussed later (Hui et al., 2009). In order to match the CTE values with the electrolyte and reduce the oxidation of the metal at high operating temperatures, some research groups introduced cermet layer where the metal is mixed with ceramics. Commonly FeCr-alloy is mixed with YSZ to from porous cermet layer (Hanifi et al., 2011). From Riso DTU, FeCr-alloy was mixed with ceramic such as Nb-doped SrTiO3 (STN) to provide close CTE values to ScYSZ electrolyte and to reduce oxidation of the metal (Blennow et al., 2013). However in this case the application was slightly different since the cermet layer was used as an additional anode backbone on top of the original Fe-Cr-Mn metal support layer. Based on these results, stainless steel power 430L (Alfa Aesar) was chosen for the base metal support material for this thesis. It was affordable and reported with good reviews of its physical properties. Its composition (by mass) is Fe:Cr:Si:C = 82.9:16.5:0.5:0.02 (Alfa Aesar, Canada).

2.3 Metal Support Fabrication Methods

Use of metal support in solid oxide fuel cell shows promising benefits compared to conventional ceramic-based SOFCs. These benefits, as mentioned before, are lower cost, improved durability, better workability, good thermal conductivity, quicker start-up, better thermal shock resistance, and tolerance towards vibrations and redox cycling (Tucker, 2010; Wang et al., 2008). However the introduction of metal such as stainless steel raises new challenges with respect to cell fabrication since the usual oxidizing atmosphere can no longer be used for high temperature sintering (Nielsen et al., 2012). Conventional ceramic based SOFC requires temperatures in the range 1200C-1400C for the electrolyte (YSZ) to be sintered (Nielsen et al., 2012; Hwang et al., 2016). This is because the electrolyte layer requires a high densification process which is achievable at these high temperatures. Densification of the electrolyte layer is critical for the performance since only a gas-tight and dense-electrolyte provides high ionic conductivity. However, this high temperature sintering can lead to serious oxidation problems for the metal

support. It is difficult to incorporate metallic substrate without oxidizing while also matching shrinkage between ceramic SOFC layers (Hwang et al., 2016). There are several processing techniques for processing the porous metal substrate, but the most common is powder metallurgy and high temperature co-sintering in reducing atmosphere. Processing steps include mixing of metal powder (FeCr, Fe-alloys, special types of alloy powders, Ni-alloys) with binder, plasticizer, pore former, and organic solvents to form slurries. These slurries can be ball-milled for 4-24hrs and be dried as a powder for die-pressing or used as a slurry for tape-casting applications (Blennow et al., 2009; Rose et al., 2009; Clemmer, 2006). Both methods are easy to implement and affordable for manufacturing. For the powder processing, it can be pressed by isostatic pressing with a die set to form a green pellet (Tucker et al., 2007; Rose et al., 2009). Metal slurries can be used for a tape-casting/ molding to form a green film and then cut into appropriate sizes (Peter Blennow et al., 2009; Molin et al., 2011; Karczewski et al., 2015; Hwang et al., 2016; Yang et al., 2015). In both cases the processed green pellets and green tapes require multi-step heat treatments. The first step is to burn-out in air (or oxygen present atmosphere) between 400°C-600°C to combust organics in the substrate. Then the second step is high temperature sintering at reducing atmosphere (e.g. 96%Argon and 4%H_2) above ~1100°C- 1200°C (Blennow et al., 2009; Molin et al., 2011 ; Karczewski et al., 2015; Hwang et al., 2016; Yang et al., 2015).

Numerous studies have focused on co-sintering metal support with cermet (metal plus ceramic) and electrolyte layers in a reducing atmosphere to avoid oxidation of the metal and agglomeration/diffusion of electrode catalyst materials (Ni). The reason is, when Ni-based anode is deposited in direct contact with a FeCr-based metal support, the system may suffer from interdiffusion of Ni, Fe, and Cr (Blennow et al., 2009; Blennow et al., 2011) at this high temperature sintering process. Interdiffusion can cause a lot of detrimental effects to both the metal support and the anode layers. The formation of Ni-Fe-Cr alloy or insulating oxides in the metal support and anode layer can reduce the electronic conductivity, increase oxidation, and increase the coefficient of thermal expansions in the support. In all cases, both performance and lifetime of the cell decrease. Various fabrication methods have been explored to avoid both oxidation of the metal support at high sintering temperature required for the electrolyte densification as well as to avoid interdiffusion of electrode catalyst and FeCr on the metal support boundaries. To solve this problem, few research groups developed unconventional cell design where the abovementioned problems can be avoided by use of infiltrated anode structure.

The design is to form a porous anode backbone with mixture of metal and ceramic (e.g. YSZ) (Blennow et al., 2009). The half-cell structure developed by Riso DTU is the following: porous metal support/porous cermet backbone/ dense electrolyte. In this unconventional design, the three layers are tape casted separately and laminated together to be co-sintered at high temperature under reducing atmosphere. Then after the high temperature sintering process, the anode catalytic material, such as CGO20+10wt%Ni slurry, is infiltrated to the porous cermet backbone (Klemenso et al., 2011). A similar approach of using infiltration of electrode materials was also reported by LBNL (Tucker et al., 2007; Tucker et al., 2007b). LBNL used five-layer structure consisting of porous metal support / porous YSZ interlayer / dense YSZ electrolyte film / porous YSZ interlayer / porous metal current collector. After high temperature co-sintering of the metal support and electrode backbone layers together, Ni and LSM ($(La,Sr)MnO_3$) were infiltrated into a porous YSZ backbone structure at the anode and cathode, respectively. This type of infiltration approach can avoid coarsening of Ni or LSM and interdiffusion between Ni, Fe, and Cr during the fabrication process (Tucker et al., 2007). Fernandez-Gonzalez et al. (2014) also focused on avoiding high temperature sintering for Ni and oxidation of FeCr alloys while using a particular metal support design. An anode material based on Ni-YSZ was applied on a porous metal honeycomb (proprietary design) support via slurry form (modified tape casting) after the high temperature co-sintering process for the metal support and YSZ dense electrolyte (Fernández-González et al., 2014). For the same purpose, a different approach was used by the Korea Electric Power Research Institue, and KIAST Korea where the anode and electrolyte were prepared separately and already sintered at high temperature in air. Then the stainless steel STN430L plate was prepared separately with channels for gas pathways. Using an adhesion layer composed of NiO, YSZ and STN430 powder, the metal support was glued to the anode and electrolyte layer and subsequently sintered at 1400°C in reducing atmosphere. To solve fabrication challenges, different processing methods, other than co-sintering, to fabricate electrodes and dense electrolytes on the metallic substrate have been explored as well. Such methods include atmospheric plasma spray processing (APS), vacuum plasma spraying (VPS), suspension plasma spraying, high-velocity oxy-fuel (HVOF) spraying of liquid suspension feedstock, pulsed laser deposition (PLD) or Electrophoretic deposition (EPD) (Blennow et al., 2011; Hwang et al., 2011; Hwang et al., 2016).

In this study, powder metallurgy with powder and press techniques were used due to simplicity and easy manufacturability. Detailed experimental procedures for the metal support synthesis are discussed in Chapter 3 experimental section.

2.4 Metal Support Characterizations

Metal support layer needs to satisfy several criteria to be used for the SOFC applications. These aspects include sintering characteristics, coefficient of thermal expansion behavior, porosity, oxidation behavior, and electrical conductivity. Sintering characteristics are important in terms of obtaining a strong and porous structure with minimized oxidation. Depending on the metal support precursor contents, multi-step heat treatments and sintering in different atmospheres is necessary to achieve the desirable final products. Also, recent fabrication routes involve high temperature co-sintering of metal support with electrolyte and anode layers. Thus sintering parameters, including temperature, time, and type of gases, affects the results of metal support as well as the ceramic layers of the SOFC. Furthermore, sintering is the primary fabrication process for metal support which affects other properties of the metal support. For example CTE, porosity, oxidation behavior, and electrical conductivity are all influenced and dependent on the sintering profile. A good CTE match is one of the most significant properties to be accomplished. The CTE values or shrinkage rate between metal-support (FeCr-alloys) and ceramics must be similar to each other to prevent delamination and cracking of the layers in both fabrication and operation. For that reason stainless steel 400 series is chosen since it has similar CTE values with YSZ, and SDC. Dilatometry is commonly used to analyze linear expansion of the materials at different temperatures. Based on this results one can determine the CTE behavior of the materials over desired temperature range and atmosphere. Porosity is important since the metal structure must render sufficient pathways for fuel gases to reach the electrodes for electrochemical reactions. There isn't a set standard for an acceptable porosity range but the common porosities reported are in the range of 20-40%. Sufficient porosities of the metal support can affect the performance of the full cell and, therefore, further performance analysis needs to be conducted to draw conclusions about adequate porosity for the metal support (Hwang et al., 2016). Typical operating temperatures for MSOFCs are much lower than those for the conventional SOFC. However, even the lowered temperature range of 600-800˚C is still high

enough to cause oxidation of the metal support layers. Corrosion resistance is an important criterion to investigate in order to verify long term performance and stability of the cells. Continuous build of oxide scale within the metal support layer can cause detrimental effects to long-term performance. Lastly, the electronic conductivity is also important. Since the oxide scale formation can lower the electronic conductivity significantly, electronic conductivity is related to both performance and durability, as well. Maintaining a good electronic conductivity and strong oxidation resistance are aspired. In this section, a detailed literature review of sintering characteristics, CTE analysis, and porosity measurements are discussed.

2.4.1 Sintering Characteristics

Sintering is an essential step required for both metal support and ceramic components in order to construct a strong porous metal support and to provide sufficient strength to the final cells. Sintering by definition is a thermal treatment for bonding particles into a coherent solid structure via mass transport events that occur on the atomic scale. The bonding leads to improved strength and a lower system energy (German, 1996). When using metal powders, there are void spaces between particles. Powders in general initially remain porous and do not pack efficiently. This initial structure is called the 'green' state. Green state reflects the unfired condition of the powder. The shaped or pressed unfired powder is termed 'compact'. Most compacts are prepared by applying pressure to the powder to increase density and invoke shape to the powder (German, 1996). A green compact is prepared prior to sintering. Many groups use this powder pressing method for preparing the metal support. LBNL showed preparation of the metal support by isostatically pressing a mixture of ferritic stainless steel powder, polymer, binder, and pore former (Tucker et al., 2007b). In the work of Rose et al. (2009) a porous stainless steel substrate was prepared by powder-metallurgy with dry isotatic pressing. The metal powder can also be prepared in a slurry form for tape casting. In this case, the tape is called the green film/tape. Blennow et al. (2009) used slurry, based on Fe-Cr power with organic additives, to make green films. In most cases these green compacts/tapes are heat treated in air first to burn off the organics then sintered in high temperature above ~1100°C-1300°C in reducing atmosphere (Blennow et al., 2009; Tucker et al., 2007). Depending on the organic additives included, the first burn out stage can be conducted in the temperature range of 400°C-700°C (Villarreal et al.,

2003). A temperature of 700°C was used when carbon/graphite is used as a pore former (Hanifi et al., 2011). For metal support, sintering atmosphere is important to prevent oxidation, and thus reducing atmosphere is most commonly used such as 4%H_2 and 96% Argon gas mixtures. Since high temperature sintering is also critical for densification of the electrolyte, it is preferred to sinter the metal support and electrolyte together by co-sintering method. Blennow et al. (2011) used co-sintering of metal support anode back bone cermet layer, and ScYSZ electrolyte in reducing atmosphere (H_2/Ar) above 1000°C. YSZ electrolyte are usually sintered at 1350°C for 4 hours in air or reducing atmosphere when sintered with metal support (Matus et al., 2005). For SDC and CGO electrolytes sintering temperature is ~1400°C - 1500°C (Yoshida & Inagaki, 2006). For anode materials the sintering temperature varies depending on the fabrication methods. When anode catalytic material such as Ni and CGO is infiltrated into a cermet anode backbone after high temperature co-sintering, calcination is conducted at 350°C for 2 hours in air (Blennow et al., 2011). When Ni-YSZ is applied on a metal support it is fired at 600°C in air (Villarreal et al., 2003). When Ni is infiltrated into porous YSZ+metal layers it is fired in air at 650°C for 15min to convert nitrate salts to metal oxides (Tucker et al., 2007). When an anode slurry was used to fill honeycomb hexagonal holes in the metallic frame, sintering was conducted at 1250°C for 4 hours in reducing atmosphere (Fernández-González et al., 2014; Ruiz-Morales et al., 2010; Ruiz-Morales et al., 2009). The cathode is usually applied at the last stage of the fabrication and has less impact on the metal support sintering process. In order to provide a reference for the cathode sintering condition, the following is mentioned: for cathode materials using LSCF/CGO, LSC, and LSC/CGO, the process commonly uses in-situ sintering at the 750-800°C in air (Klemensø et al., 2011; Nielsen et al., 2014).

2.4.2 The Coefficient of Thermal Expansion (CTE)

Stainless steel 400 series was chosen as one the metal support materials due to similar coefficient of thermal expansion values (10-12 ppm/K) as that of the ceramic layers. It was found that the CTE of 400-series alloys are close to that of the yttiria-doped zirconia (10-12ppm/K) (Tucker, 2010) and ceria-based electrolyte materials (SDC has 12.7 ppm/K, FuelCellMaterials). However, a complete match is still necessary for fabrication without delamination and operation upon rapid thermal cycling (Tucker et al., 2011). In order to measure the CTE values, dilatometry is

commonly used to measure the linear expansion and shrinkage of a material over the certain range of the temperatures. Only few studies have focused on the CTE measurements of the various metal alloys for SOFC application and comparison with the ceramic materials. In the work of Matus et al. (2005) FeCr containing 30 wt% of chromium was mixed with 6 vol% (~3 wt%) of aluminum titanate (AT) with a CTE of less than $0.5x10^{-6}\ K^{-1}$ to match the CTE of an 8YSZ electrolyte. This addition of ceramic additive can provide almost exact match of CTE values to 8YSZ while not compromising the electronic conductivity and brittleness. The new porous cermet layer called Fe30Cr3AT was fabricated and the thermal expansion of YSZ, Fe30Cr, Fe30Cr3AT, and Ni/YSZ were measured using dilatometry. The thermal expansion of the materials was recorded between room temperature and 1475 K and it is shown in Figure 2.1

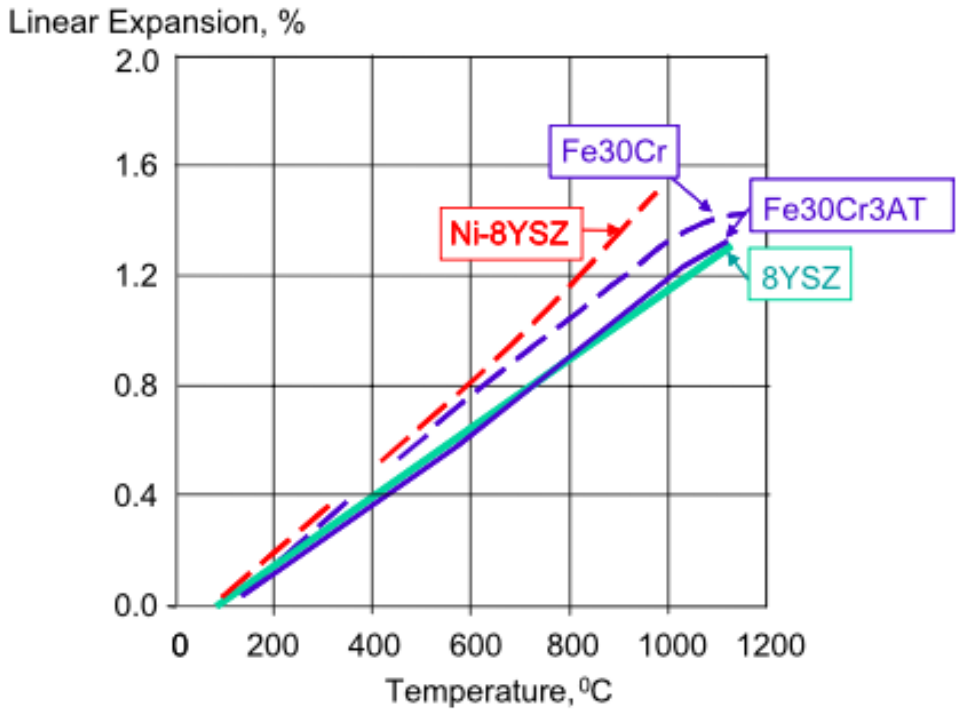

Figure 2-1 Thermal expansion of 8YSZ electrolyte, Fe30Cr metal support, Fe30CrAT cermet, and Ni-8YSZ anode (Matus et al., 2005)

It is shown that the thermal expansion of the metal/ceramic composite (Fe30CrAT) substrate fully matched that of 8YSZ electrolyte. This type of exact match of CTE is beneficial when the metal support is co-sintered with thin electrolyte layer in reducing atmosphere. Also, once the cell is under operating condition with rapid thermal cycling at approximately rate of 50K/min

between 201 and 580°C, a good CTE match can mitigate thermal stress. Hui et al. (2007) briefly mentioned the importance of CTE match since the mismatch can often cause cracks, severe warping, or cell fracture during high temperature firing steps. It also reported that the CTE criteria for the metal support to be around ~11 x 10^{-6} K^{-1} between 30-1000°C. There are not many groups that investigated the sintering characteristic of the metal support only. Commonly, the CTE values are compared between those of metal-support and ceramic components. In this thesis, CTE values of metal supports with different porosities were investigated to observe any trend or impacts. The detailed experimental methods and results will be discussed in the later chapters.

2.4.3 Porosity Measurement

The metal support has to be porous enough to deliver sufficient fuel gases to the anode sites while maintaining durable structures. Porous structures can be produced by various fabrication routes including mold, meshes, laser machining, and powder metallurgy (PM) (Rose et al, 2009). As introduced earlier, the honeycomb design mold with modified tape casting was used to provide porous structures with reduced material usage (Fernandez-Gonzalez et al., 2014). Baek et al. (2011) used ferritic stainless steel (STS430) as the metal- support; the gas channel was fabricated in a serpentine shape with a channel width of 500μm by using wire cutting equipment to modify the metal-support structure (Baek et al., 2011). Powder metallurgy is widely used due to the simplicity of the process and cheaper manufacturing cost. In all cases, the porosity measurement can be useful to determine whether sufficient gas transfer is possible or not. Rose et al. (2009) investigated four different methods of porosity measurement on porous metal support fabricated with AISI 430L (Stainless steel 430L grade) via powder metallurgy methods. The first method is the Archimedes methods based on ASTM standard C373-88. The second method was using mercury porosimetry. The third test was using X-ray diffraction (XRD) where physical substrate mass and dimension combined with calculations of theoretical density from XRD can determine the cell volume (XRD/weight). The fourth method was gas permeation using dry helium and measuring the mass flow. Based on the results, it was reported that the four measurement methods differed by up to 10% from each other. Brunauer–Emmett–Teller (BET) surface area analysis (SA3100, Beckman Coulter, Fullerton, CA, USA) was also tried to

determine the surface area of the samples and porosity however it was not possible due to the equipment measurement limit (Rose et al., 2009).

Image analysis can be used to measure porosity with optical microscope on polished cross section of the porous metal support samples as well. This method was used by Rose et al. (2009) and Harrisa et al. (2011). Another method is to back calculate the porosity based on weight and dimensions of each substrate knowing the full density of the metal sample (Waldbillig & Kesler, 2009). The detailed equation for calculating the porosity using this method can be found in the experimental section. Based on the literature reviews on how to measure porosity, there is no universally accepted standard on how porosity should be measured. Thus various test methods exists and it is important to have more than one measurement available to verify the results.

Chapter 3 Experiments

In this chapter synthesis of starting material, fabrication steps of the metal support, and characterization methods are discussed. Synthesis of starting material refers to the mixing of stainless steel powder to form a precursor solution with organics. The fabrication methods explains the die pressing step to form a green compact pellet and heat treatment process, including burn-out and reducing atmosphere sintering. Characterization methods include various techniques used as the following. First is the determination of burn-out and sintering temperature profile using thermal gravimetric analysis (TGA). Second is the characterization of the sintering behavior by measuring the relative green density, relative sintered density, and change in mass before and after sintering. Third is to measure the porosity using three approaches including Archimedes method based on ASTM standard (C373-88), optical analysis, and back calculation based on solid density of SS430L sample. Fourth is to determine the CTE values of the sintered porous metal support. For this test, different solid loading samples were tested in dilatometer under argon atmosphere with a specified temperature profile. Fifth is to measure the electronic conductivity of the metal support. The existing SOFC testing station was used to measure the electronic conductivity of the metal support in the operating temperature ranges 550-800°C. Lastly, SEM images were taken to assess the micro structure of sintered metal supports. The procedures and the experimental set-ups are discussed in this chapter.

3.1 Synthesis of Metal Powder

Stainless steel metal powder SS430L (Alfa Aesar) with particle size of d50=44μm (~325 mesh size) and composition of Fe:Cr:Si:C=82.9:16.5:0.5:0.02 wt% is chosen as the base powder. In order to form a precursor solution, SS430L is mixed with organics consisting of pore formers (two types: poly methyl methacrylate (PMMA) (Scientific Polymer) or graphite (Alfa Aesar)), binder (polyvinyl butyral (PVB), Scientific Polymer), and plasticizer (di (n-octyl)amine (DOP), Sigma-Aldrich), and solvent ethanol (UW Chemstore). Table 3-1 summarizes information about materials and their providers. Different compositions of precursor solution were prepared by varying SS430L weight percent (wt%) from 80, 85, 87, 90, to 95wt%. All of these 5 different

solid loading compositions were prepared in the same manner. The reason for using two different types of pore former is because PMMA is supposed to create bigger pores and graphite is supposed to create smaller and finer pore structures. At the beginning stage of the experiments it was not clear which pore former will be more suitable for fabricating metal support for SOFC applications thus both pore formers were tried separately. Two types of solutions were prepared. The first type is with PMMA as a pore former and the organics mass ratios is PVB: DOP: PMMA = 1:1:3. The second type is with graphite as a pore former and the organics mass ratio is PVB: DOP: Graphite = 1:1:3 respectively. Organics mass ratios for both solutions were kept constant for different SS430L solid loading samples. In Table 3-2 the metal support powder composition is listed in weight percent (wt%).

Once the precursor solutions (SS430L and organic mixture) are prepared, they are ball-milled with zirconia balls for 24 hours. After ball milling, the solution is transferred into mortars for drying process. There are two types of mortars available: ceramic mortar and stainless steel mortar. The reason for using two types of mortar is because ceramic mortar might have contaminated the metal powder with excess amount of silicon oxide (mortar material) and stainless steel mortar can avoid such contamination. Mortar containing precursor solution is dried on a hot plate to evaporate the solvent (ethanol) at 60-70°C for 5-6 hours. In the next chapter, the effect of using different mortars was investigated further but the results showed that there is basically no difference. When the powder is made with ceramic mortar it is labeled with C#, where the number indicating batch number of the powder and when the powder is made with stainless steel mortar it is labeled with S#. The dried powder is hand grinded further in the mortar to be sieved below particle size of 177 µm (mesh size 80). It is important to achieve most of the particles (95% by mass) into this size (<177µm) since particle size can affect compositions, green density, and sintering behaviors. It was noted that particles tend to agglomerate during the drying process and there is a limit for breaking the particles into smaller sizes below 177µm by hand grinding process. It is possible to use smaller sieve/mesh (80µm or 44µm) to further separate the particle size distribution. However, separating powders into smaller than 177µm changes the powder compositions. It was observed that powders with size less than 80µm have more organics because the organics break down to smaller particles more easily than the metal powder. This results in deviated wt% of the precursor powder when the powder particle size was separated below <80 µm compared to the expected wt%. Thus sieve with 177µm particle size

was used to ensure uniform mixture of SS430L and organics. Once the powder is sieved it can be stored in a glass vial with a cap to be used for the next processing steps.

For the characterization of the metal support, three batches of powders were used and each batch includes all 5 different solid loading of SS430Lwt%:80, 85, 87, 90, and 95. The first batch was made with ceramic mortar and was labeled C1. The second batch is a repeat of the first batch, was also made with the ceramic mortar, and was labeled C2. The third and last batch was made with the stainless steel mortar and labeled S1. In the results section, synthesized powders are referred to with labels C1, C2, and S1.

Table 3-1 Material information and supplier

Materials	**Function**	**Provider**
SS430L	Base powder	Alfa Aesar (product#47290)
Polyvinyl butyral (PVB)	Binder	Scientific Polymer(CAT512)
Poly(methyl methacrylate) (PMMA)	Pore former (bigger pore)	Scientific Polymer(CAT037D)
Graphite	Pore former (smaller pore)	Alfa Aesar(product#40795)
Di-n-octyl phthalate (DOP)	Plasticizer	Sigma-Aldrich
Ethanol	Solvent	UW Chem store

Table 3-2 Metal support compositions in weight percent (wt%).

Precursor Solution Compositions		**Individual Organics wt% (Mass ratio is PVB:Plat:PMMA=1:1:3)**		
SS430L wt%	Organics wt%	PVB	Plasticizer	PMMA or Graphite
95	5	1	1	3
90	10	2	2	6
87	13	2.6	2.6	7.8
85	15	3	3	9
80	20	4	4	12

3.2 Fabrication of Porous Metal Support via Solid-State Sintering of Powders

Once the metal powder mixture is sieved, it is pressed isobarically using a hydraulic hand press at 300 MPa for 3 minutes to form 20mm diameter green pellet. The 20mm metallic dry die set was purchased from Across International (USA). The quantity of powders used to press one disk differs based on the SS430L solid loadings. Table 3-3 shows the powder weight required for different SS430L compositions to keep the base metal content constant as 2.175g. This process is applied in the same way for both PMMA and graphite precursor solutions. Once the green compact pellet is made, the weight and dimensions are measured. Dimensions include diameter and height and they are measured with a caliper 5 times each and averaged to improve the accuracy of the measurements. Measurement details can be found in section 3.3.1. The next step is the heat treatment process involving burn-out of the organics in air and high temperature sintering in reducing atmosphere (4%H_2/Ar). The pressed green compact pellets are placed on a porous flat alumina sample holder (2cm width x 5cm length) and inserted inside a furnace quartz tube (50cm OD x 44cm IDx 1219cm L, MTI Corp, USA) that is placed inside a Mellen Furnace (The Mellen Compnay Inc. USA). This furnace has three heating zones (left, center, and right) and can operate between room temperature up to 1200°C. When the precursor powder with PMMA is used to form green pellets, it was found that the organics mixture start to burn off at 300-400°C based on the TGA results. Thus the burn out was set in air at 400°C for 5 hours. After the burn-out, the furnace gas is switched to argon at 400°C to purge oxygen for 1 hour prior to introducing 4%H_2/Ar reducing atmosphere. Here, reducing atmosphere was used to prevent oxidation of the metal at high temperature and to reduce metal oxides that may have formed in the previous step. Ar was chosen instead of N2 because N_2 can form nitrides with iron and chromium. After purging, reducing atmosphere 4%H_2/Ar is applied and the temperature increases from 400 to 600°C at 10°C/min and stays for 30 min. Then the temperature is ramped, still in 4%H_2/Ar, from 600 to 1000°C at 5°C/min and stays for 10min. Then the temperature is ramped from 1000 to 1100°C at 2°C/min and it stays for 5 hours for sintering. The detailed sintering profile is shown in Table 3-4 and it was carefully chosen based on the TGA analysis of each organic components to determine sufficiently high temperature for burn-out but low enough temperature to minimize oxidation of the metallic support. On the other hand, when powder with graphite is used, the burn-out temperature needs to be increased to 700°C since graphite requires much higher temperature to be combusted. However, 700°C in air causes the metal

support to be oxidized which is not desirable. Further analysis using TGA results showed that the use of graphite as pore former is not suitable for low temperature burn-out and minimized oxidation sintering. Therefore the use of graphite precursor solution was not pursued for the fabrication and characterization of metal support.

Table 3-3 Powder base load for different SS430L wt%

SS430L wt%	SS430L (g)	Base load (g)
95	2.175	2.289
90	2.175	2.417
87	2.175	2.500
85	2.175	2.559
80	2.175	2.719

Table 3-4 Burn-out and sintering temperature profile

Steps	Start Temp	Set Temp	Ramping rate (°C/min)	Time (min)	Gas	Gas
1	0	400	10	40	Air	
2	Hold	400		330	5hr Air	1hr Ar
3	400	600	10	20	4%H_2/Ar	
4	Hold	600		30	4%H_2/Ar	
5	600	1000	5	80	4%H_2/Ar	
6	Hold	1000		10	4%H_2/Ar	
7	1000	1100	2	50	4%H_2/Ar	
8	Hold	1100		300	4%H_2/Ar	
9	1100	25	3	330	4%H_2/Ar	
10	end				4%H_2/Ar	

Once the metal support is sintered, weight and dimensions are measured in the same way as before sintering. A series of characterizations were conducted to analyze the sintering results, porosity, coefficient of thermal expansions, electronic conductivity, and microstructures. As

mentioned above, only the solution with PMMA as a pore former is characterized. Figure 3-1 shows the process flow of the metal support fabrication.

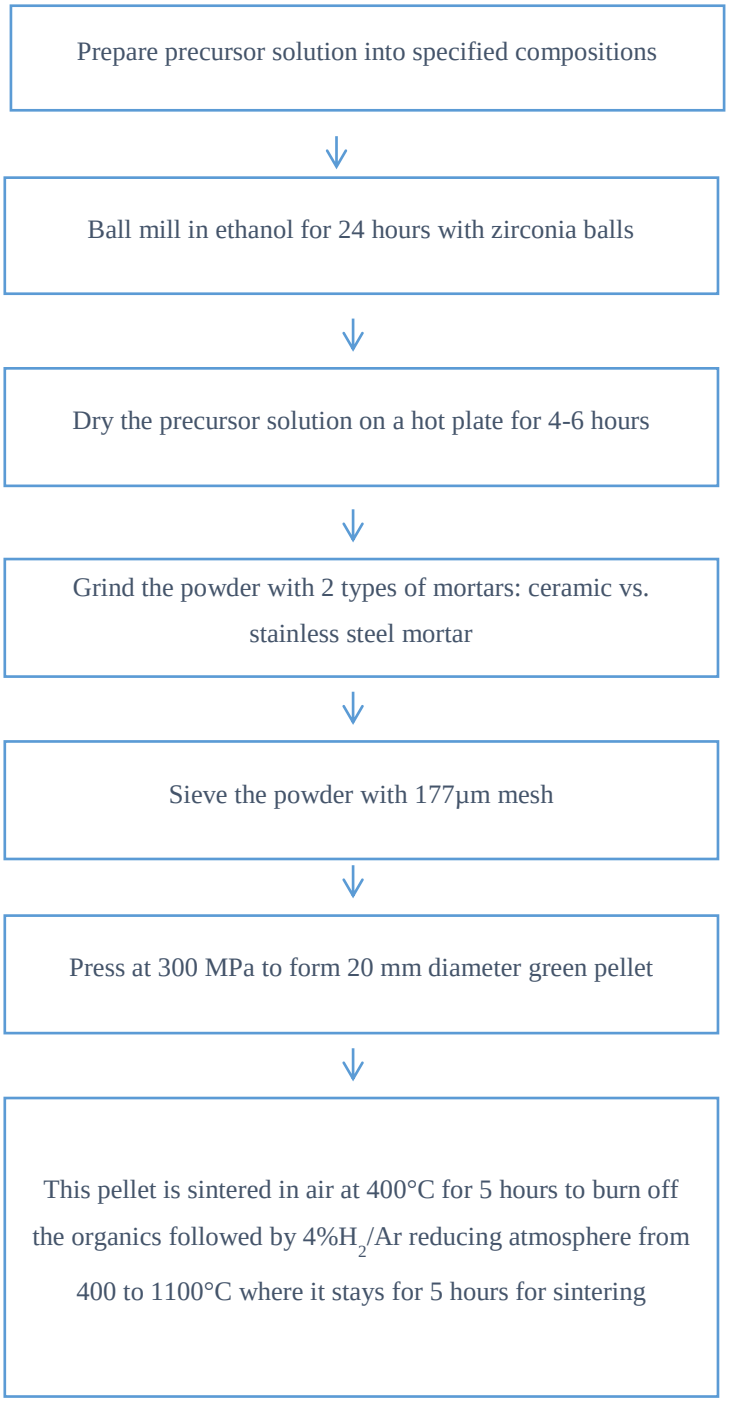

Figure 3-1 Material synthesis and fabrication process flow.

3.3 Characterization of Metal Support Layer

3.3.1 Sintering Results

In order to quantify the sintering results, the relative green density and the relative sintered density of the metal support samples were measured. Since the metal supports were pressed with a 20mm dry die set, the pressed pellets come out as a disk form with varying heights and a fixed diameter (~20mm). For the green and sintered density measurements, diameters and heights of the metal pellets were measured 5 times each with a caliper and averaged. The mass of the pellets was measured before and after sintering using a high precision scale. Equations 3.1 and 3.2 were used for measuring the average diameter and the average height, respectively.

$$D_{avg} = \frac{D_1 + D_2 + D_3 + D_4 + D_5}{5} \tag{3.1}$$

Where D_{avg} is the average diameter and $D_{\#}$ indicates number of measurements.

$$H_{avg} = \frac{H_1 + H_2 + H_3 + H_4 + H_5}{5} \tag{3.2}$$

Where H_{avg} is the average diameter and $H_{\#}$ indicates number of measurements.

The volume of the pellet (V_{pellet}) was calculated, based on the results of Equations 3.1 and 3.2, as follows:

$$V_{pellet} = \frac{(D_{avg})^2 * \pi * H_{avg}}{4} \tag{3.3}$$

Then, the green density and the sintered density of the metal support pellets can be found using the next equations (3.4) and (3.5), respectively.

$$Green\ density = \frac{m_{green}}{volume_{green}} \tag{3.4}$$

$$Sintered\ density = \frac{m_{sintered}}{V_{sintered}} \tag{3.5}$$

Knowing the reference density of solid SS430L metal, the relative density can be calculated as below:

$$Relative\ density = \frac{Measured\ density}{Reference\ density\ of\ solid\ SS430L\ \left(\frac{7.65g}{cm^2}\right)} \quad (3.6)$$

3.3.2 Effects of Organics (PMMA, PVB, and DOP)

In the synthesis of metal powder it was mentioned that the organic mass ratio was kept constant such that PVB: DOP: PMMA = 1:1:3 for varying SS430Lwt%. This ratio was determined based on the analysis of how each organic component affects the final powder quality. Hence the study of each organics is included to show the individual effect on fabrication and sintering results. In order to investigate the effect of individual PVB, DOP, and PMMA the following compositions of metal powder solutions were prepared. In this experiment, the SS430L solid loading was kept constant at 87wt%. The synthesis process is the same as described in 3.1 and 3.2.

In Table 3-5, the composition of varying PMMA content is shown. The PMMA mass ratio differs from 1 to 5 with increment of 1 while keeping PVB and DOP ratio constant at 1.

Table 3-5 Compositions for varying pore former, PMMA, content

By mass ratio			**By wt% (for constant SS430L 87wt%)**		
PVB	Plasticizer	PMMA	PVB	Plat	PMMA
1	1	1	4.33	4.33	4.33
1	1	2	3.25	3.25	6.50
1	1	3	2.60	2.60	7.80
1	1	4	2.17	2.17	8.67
1	1	5	1.86	1.86	9.29

In Table 3-6, varying binder, PVB, composition is studied. The PVB mass ratio varies from 1 to 5 with an increment of 1 while keeping DOP ratio at 1 and PMMA ratio at 3.

Table 3-6 Compositions for varying binder, PVB, content

By mass ratio			By wt% (for constant SS430L 87wt%)		
PVB	Plasticizer	PMMA	PVB	Plat	PMMA
1	1	3	2.60	2.60	7.80
2	1	3	4.33	2.17	6.50
3	1	3	5.57	1.86	5.57
4	1	3	6.50	1.63	4.88
5	1	3	7.22	1.44	4.33

In Table 3-7, varying amount of plasticizer, DOP, content is examined. The mass ratio of DOP is varied from 1 to 5 in increment of 1 while keeping PVB ratio as 1 and PMMA ratio as 3.

Table 3-7 Compositions for varying plasticizer, DOP, content

By mass ratio			By wt% (for constant SS430L 87wt%)		
PVB	Plasticizer	PMMA	PVB	Plat	PMMA
1	1	3	2.60	2.60	7.80
1	2	3	2.17	4.33	6.50
1	3	3	1.86	5.57	5.57
1	4	3	1.63	6.50	4.88
1	5	3	1.44	7.22	4.33

3.3.3 TGA Analysis and Sintering Results

Using thermal gravimetric analyzer (TGA), burn-out and sintering temperature profiles were established as mentioned earlier. TGA was able to determine the burn-out temperature for individual organic component including PVB, PMMA, and graphite. Precursor powder with SS430L 75wt% was also tested in TGA to find when the oxidation starts to occur so that the sintering profile can be adjusted accordingly. TGA analysis detected susceptible range for oxidation of stainless steel SS40L. Based on these results, burn-out temperature and duration were determined. Finally, the oxidation resistance of sintered metal disk was analyzed using TGA as well in the operating temperature ranges of 600, 700, and 800°C for 12 hours in air. For these measurements, solid loading of 80 and 95wt% samples were used.

3.3.4 Porosity Measurements

Porosity is an important parameter to make sure sufficient amount of fuel gases can travel through the metal support and reach the anode site for the electrochemical reactions. Based on literature reviews it was found that porosity of 20~40% were commonly used in many of MOSFC designs (Rose et al, 2009). The fundamental purpose of this measurement is to verify the presence of sufficient pores that provide gas diffusion path ways while maintaining a strong structure. Three types of measurements were taken to determine porosity. The first is Archimedes method based on ASTM Standard C373-88. The detailed procedure of this ASTM method is included in Appendix 2. According to this ASTM standard, the sintered metal support disks with SS430Lwt% of 80, 85, 87, 90, and 95 were boiled in water for 5 hours and then soaked in water for 24 hours to make sure all pores were penetrated with water, after which a measurement was made, followed by another 24 hours soaking.. The mass of saturated sample with water was measured after soaking in water for 24 hours and then again after another 24 hours. Based on the difference of dry sample weight and saturated sample weight the porosity was determined. The average values of porosity measured after 24 hours and 48 hours were used. In total 2 samples were measured per given SS430Lwt%.

The second method is using an optical microscope (Olympus-BH2-UMA with Roper Scientific-Photometric digital camera) to examine the polished microstructures of sintered porous metal support samples. SS430Lwt% of 80, 85, 87, 90, and 95 were mounted into epoxy (Struers Specifix-20). The samples were cured overnight and removed from the mounting cups. The edges of the samples were grounded using silicon carbide grit paper (220 to 600 grit American Standard). Then these samples were polished with 3μm diamond suspension. Using the microscope, a matrix of 3×3 images at 5x magnification were taken per sample surface. Sample images are shown in Figure 3-2.

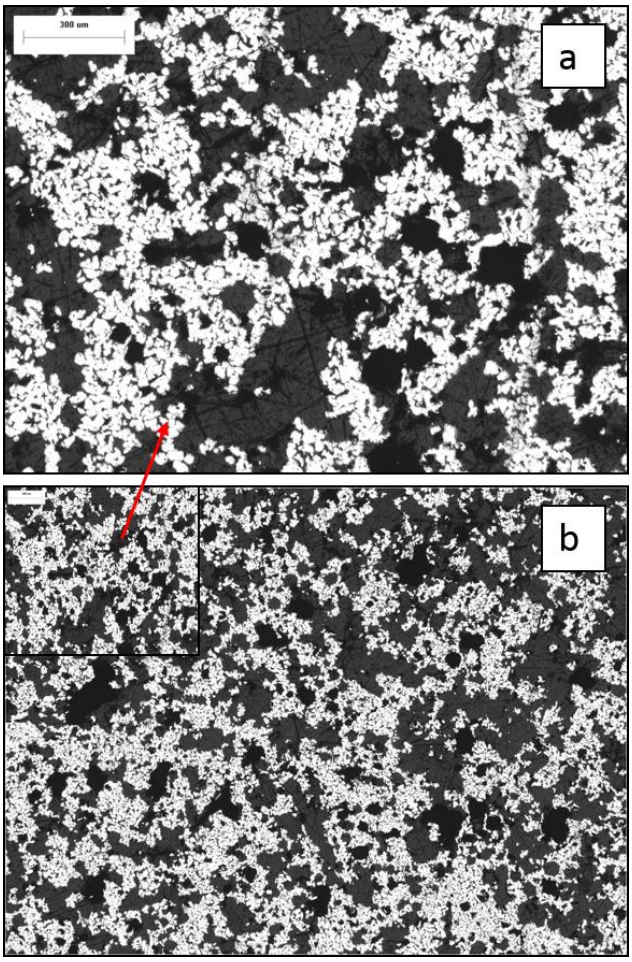

Figure 3-2 a) Optical analysis images at 5x magnification. b) Matrix of 3x3 images at 5x magnification including image 'a' in the upper left corner.

The first image a) is included in the second image b) as part of a 3x3 matrix. The Image Pro Software was used to calculate the area fractions of dark and bright colour contrast to estimate the porosity. The dark area represents pores. It is important to keep in mind that this method is performed on the fraction of sample surface and it does not represent the porosity of the entire sample volume.

The last method was back calculating the porosity knowing the full density of the solid SS430L which is 7.65 g/cm^3 (Ametek). The following equation is used to calculate the porosity.

$$\varepsilon = 1 - \left(\frac{\rho_{sint}}{\rho_{ref}}\right) \tag{3.7}$$

Where $\varepsilon\ is\ porosity$

$\rho_{sint}\ is\ sintered\ density\ of\ sample$

$\rho_{ref}\ is\ full\ density\ of\ stainless\ steel\ 430L$ (7.65 g/cm^3)

The value of ρ_{sint} can be determined by measuring the dimensions of the sintered metal support using caliper to find the volume and balance to find the weight. In order to measure the diameter and height of the metal support accurately, 5 measurements were taken for diameter and height separately and then averaged. The results of three different porosity measurements are compared in Chapter 4.

3.3.5 Coefficient of Thermal Expansion Measurements

The coefficient of thermal expansion (CTE) was measured using a dilatometer (Netzsch 402C Dilatometer) to determine compatibility of metal support CTE to anode and electrolyte materials (SDC/nickel oxide and SDC, respectively). It is important to have similar CTE values between materials in order to prevent cracking, warping, and delamination during high temperature co-sintering and operating conditions. High temperature dilatometer can measure the dimensional changes of a sample with respect to time and temperature. Changes in dimension are recorded by a push rod that is in contact with the sample with a small force of 0.20 N which is to ensure good contact while not interfering with the sample expansion/shrinkage. Through the push rod the changes in linear displacement is measured and recorded by a computer. This particular dilatometer was able to detect changes up to ±2.5mm with sensitivity of 1.25nm/1 digit (Clemmer, 2006). The Netzsch 402C dilatometer is equipped with an alumina push rod, sample holder, sapphire plug (alpha-Al_2O_3), and sapphire crucible (alpha-Al_2O_3) and a schematic is shown in Figure 3-2. The sample is placed inside the sapphire crucible and fixed with the sapphire plug. The alumina push rod is in contact with the sapphire plug and the change in linear dimension is measured. The ambient environment can be controlled and for this study argon gas was used as an inert atmosphere. The dilatometer components such as sample holder, rod, plug, and crucible can also experience thermal expansion and shrinkage upon operation under high temperature profile. To eliminate this expansion/shrinkage behavior of the dilatometer components a ‘blank’ test (without sample) is used with alumina standard (reference sample)

under the same test conditions as the actual samples to be measured. Those blank tests are actually repeated at least 3 times to make sure that the last two runs are the same. When the data for the actual samples are recorded, the data can be corrected by removing the effects of dilatometer components from the raw measurement data, thus revealing the true CTE values of the sample (Clemmer, 2006).

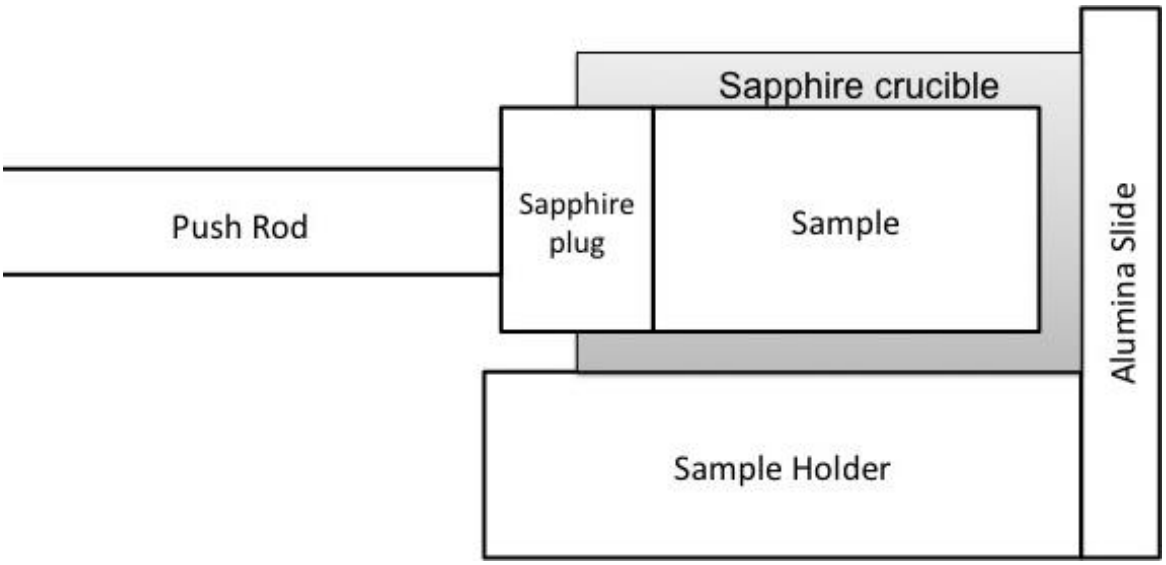

Figure 3-3 Schematic diagram of dilatometer set-up.

The sintered metal support samples with PMMA as a pore former were used for CTE measurements. Different solid loadings of SS430L samples: 80, 85, 87, 90, and 95wt% were used to make green pellets with 6.45 mm diameter at 650 MPa for 3 minutes under the hydraulic press. These pellets were then sintered using the sintering profile described in Table 3-4. Sintered pellets were analyzed for CTE values in the dilatometer in argon atmosphere with temperature profile of: 10°C/min heating rate from 25°C to 1100°C and isothermal hold at 1100°C for 5 hours. This profile was chosen because the final hold temperature is what is potentially required for electrolyte sintering in the application considered here. Argon gas was chosen as inert and thus it will not change the metallic substrate chemically. The results of CTE values with varying SS430Lwt% samples are shown in Chapter 4.

3.3.6 Electronic Conductivity Measurements

The electronic conductivity of sintered metal support pellets with SS430Lwt% of 85, 87, and 90 were measured by potentiodynamic test. The sintered metal supports were pressed and sintered using the aforementioned fabrication method with precursor using PMMA as a pore former. The mass and thickness of the sintered disk after sintering was measured. 6 layers of scotch tape were prepared by layering each scotch tape strip on top of one another to create an adequate height for painting the Ag paste on the sintered disks. Then a hole was punched though the 6-layer with an he area of 0.283cm^2. An Ag paste (ESL ElectroScience, USA) was applied on both sides of the sintered disk by painting it through this hole cut into 6 layers of scotch tapes. The Ag paste was painted in the middle of the disk on both sides. Then the painted disk was baked for 1hr at 700˚C in the muffler furnace in air. The current collectors used were composed of Ag wire and Ag mesh. The Ag wire and mesh are connected to the silver paste on the sintered metal support as shown in Figure 3.4.

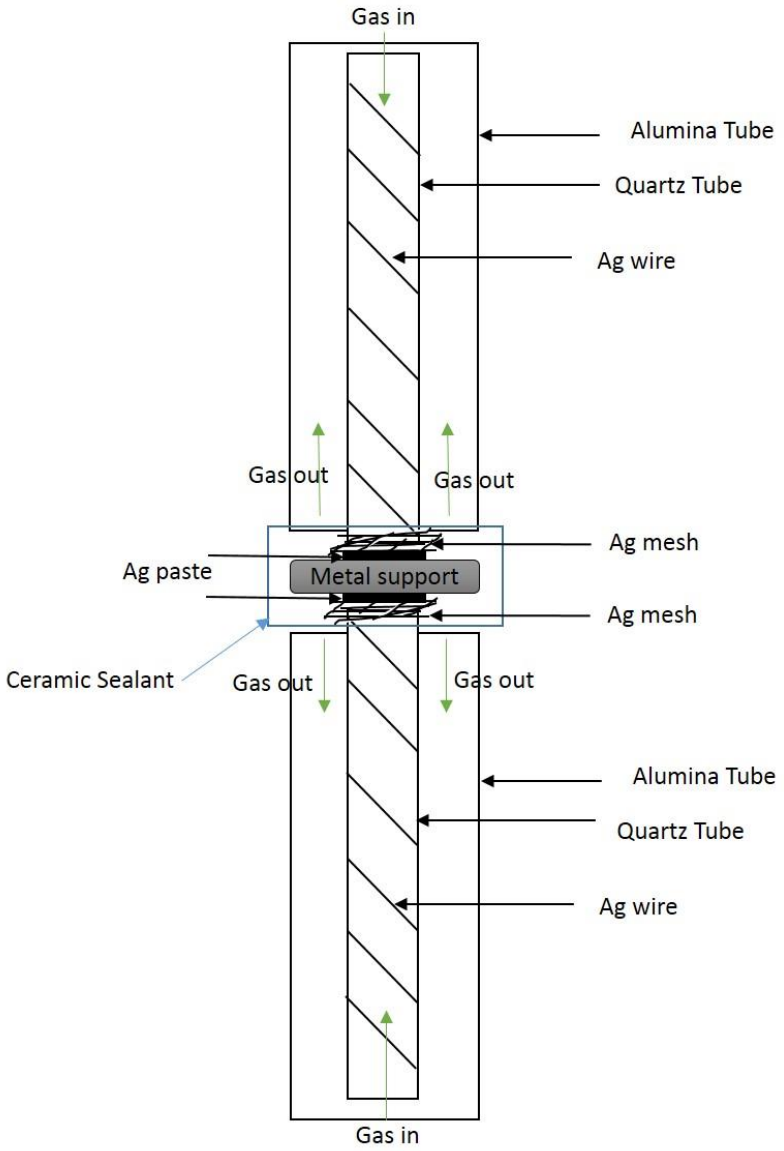

Figure 3-4 Schematic of the electronic conductivity measurement set-up.

The Ag mesh provides direct contact between the Ag paste on the metal support and the Ag wire. The metal disk was fixed with a ceramic sealant to an alumina tube in the test apparatus. The measurements were conducted in two types of atmosphere: argon and air from 550 to 800˚C at 50˚C intervals with 5˚C /min ramping which provides 6 measurement points: 550, 600, 650, 700, 750, and 800˚C. At each measurement the temperature was hold for 30 minutes to reach steady-state. Argon gas was used first and the conductivity was measured in increasing temperature and repeated in decreasing temperature from 800 to 550˚C at 50˚C intervals with -

5˚C /min rate. Once the argon run was completed in both forward and reverse temperatures, then the gas was switched to air to examine if oxidation affects the conductivity. The same measurements were taken for both argon and air system and the temperature profile is shown in figure 3-5.

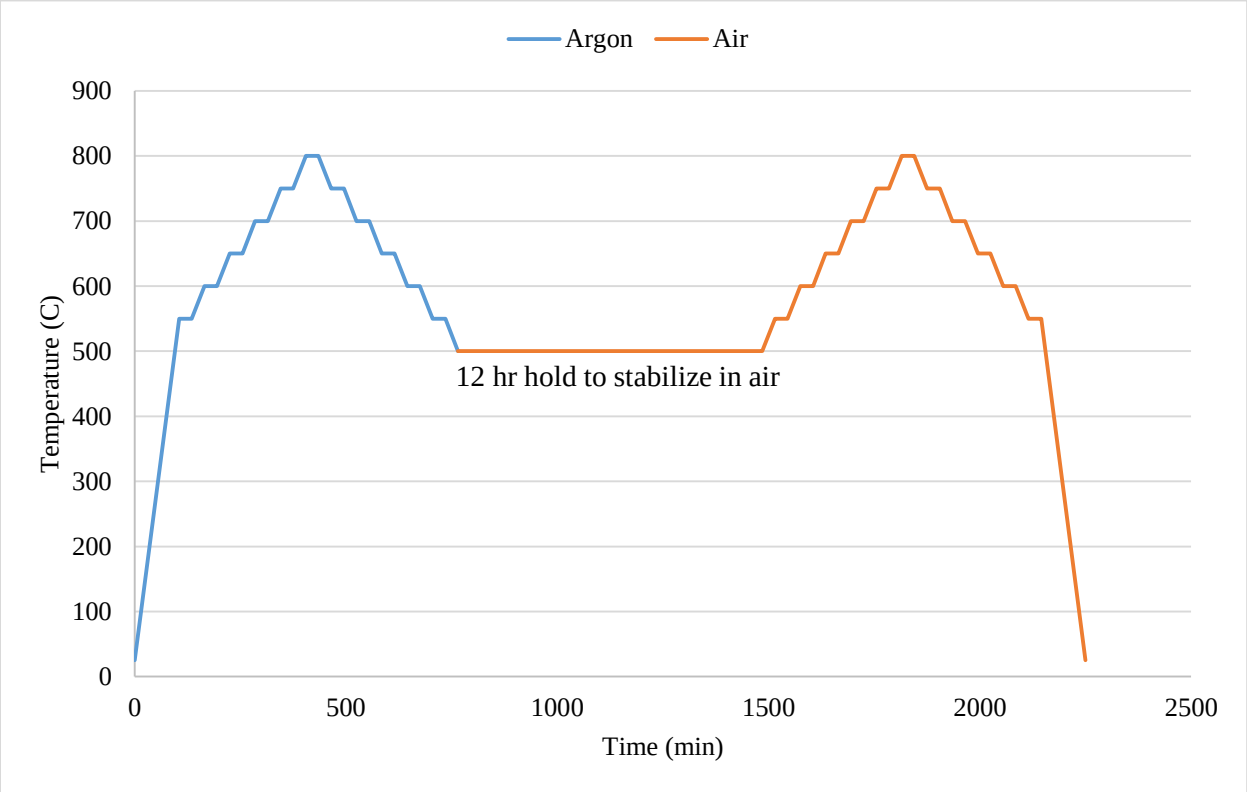

Figure 3-5 Temperature profile used for the electronic conductivity measurements.

However, before initiating the air-run, the system was stabilized in air at 500˚C for 12 hours prior to recording conductivity measurements. Then the same measurements were conducted in air first going up in the temperature from 550 to 800˚C at 50˚C intervals with 5˚C/min ramp and then reverse.

Potentiodynamic test measured I-V curve at each temperature and showed linear plot of voltage versus current and the slope was used to calculate electronic conductivity. A sample I-V curve is shown in figure 3-6.

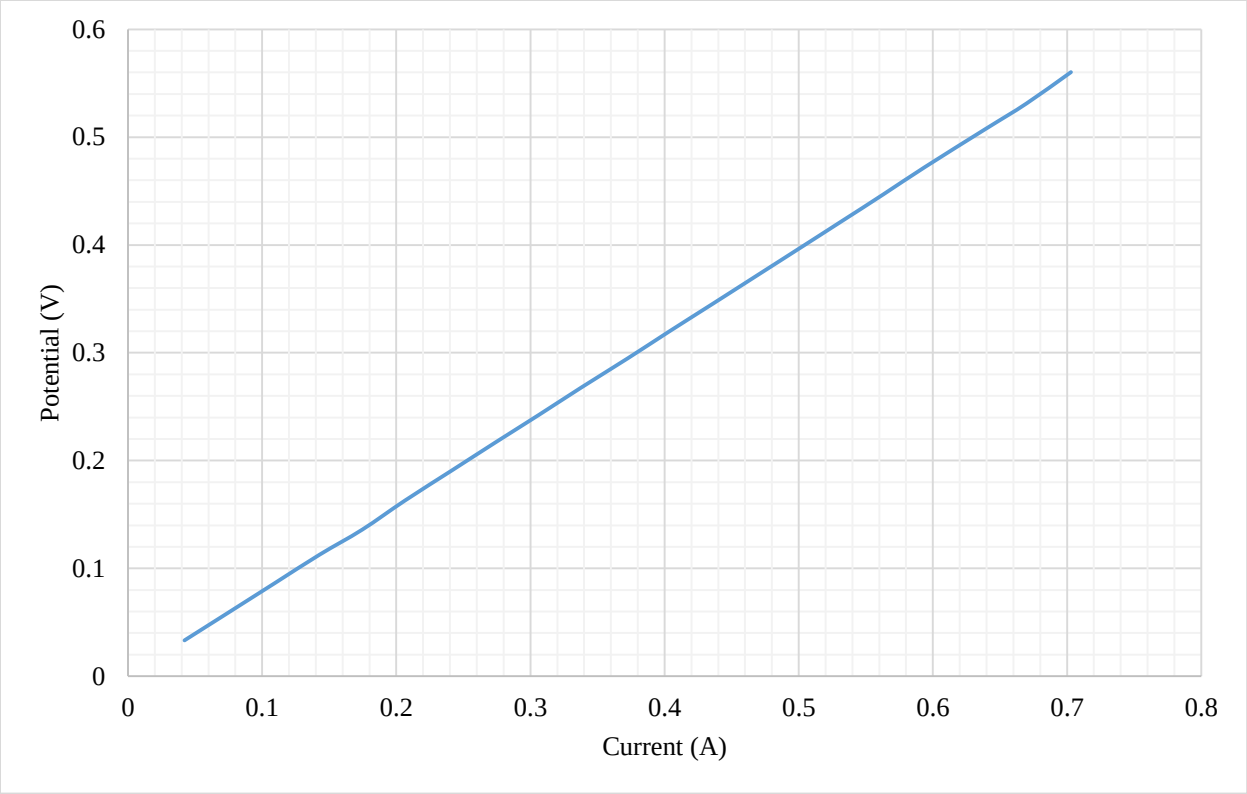

Figure 3-6 Sample I-V curve in argon for C1-90wt% sample

Using the linear relationship in I-V curve, the resistance, R, is defined as the slope and can be determined by the following equation:

$$R = \frac{V}{I} \tag{3.8}$$

Where R is resistance in (Ω)

V is voltage in volt (V)

I is current in amps (A)

Electronic conductivity and resistance R is related by inverse relationship as below

$$\sigma = \frac{L}{RA} \tag{3.9}$$

Where σ is conductivity $\left(\frac{S}{cm}\right)$

L is height of the metal support (cm)

R is resistance from equation (3.8) in Ω

A is area of the silver paste which is 0.283cm^2

Once the electronic conductivity is measured from an I-V curve, measurements are gathered to plot electronic conductivity versus temperature graph.

3.3.7 Scanning Electron Microscopy (SEM) Analysis

SEM images were taken for different solid loading of SS430Lwt% samples to assess microstructures of porous metal supports. The analysis was conducted in the Waterloo Advanced Technology Lab (WATLab) in Chemistry Department using model LEO 1530 FE-SEM scanning electron x-ray analyzer (EDX). Some analysis was conducted in mechanical materials lab in E3 (Mechanical and Mechatronics Engineering) using model JEOL JSM-6460 SEM. The EDX was used to analyze the elemental composition of the material. Samples were prepared in both surface imaging and cross-sectional imaging. Prior to the analysis, a ~20mm sintered metal support disk was broken down to ¼ piece and mounted on a 70° pre-tilt stub holder (Ted Pella Inc., USA) for a cross-section and on a flat sample holder for a surface images. Carbon conductive tapes (Ted Pella Inc., USA) were used to fix the samples on to both tilted and flat sample holders. Since the metal support is electronically conductive gold sputtering was not required. SEM images were taken at various magnifications using 10kV -20kV energy beams.

Chapter 4 Results and Discussions

In this chapter the results of metal support characterizations are discussed. First, the burn-out temperature and sintering profile were determined based on the TGA analysis. Then, the oxidation behavior of the sintered metal support was investigated in the TGA to determine the appropriate operating temperature ranges. Second, was the determination of suitable metal support compositions by examining the effect of organics. Once the most suitable organics ratio was found, the sintering results of varying SS430Lwt% were studied. Third, was the measurement of porosity and determine a relationship between the porosity and SS430L loadings. Fourth, was the measurement of the CTE of varying SS430L loadings and determine the expansion and shrinkage behavior of the metal support. Fifth, was the measurement of the electronic conductivity at various temperatures. Last, was the analysis of the microstructure using SEM and EDX.

In this chapter, three batches of powders for different solid loadings of SS430Lwt% were used. As mentioned in the experimental section, the first batch was made with the ceramic mortar and labeled C1. The second batch was made with the ceramic mortar as a repeat of C1 and labeled C2. The third batch was made with the stainless steel mortar and labeled S1.

4.1 Determination of Burn-out and Sintering Profile via TGA Analysis

Using thermogravimetric analysis (TGA), burn-out temperatures of the organics, sintering profile, and oxidation behavior of the support were analyzed. In this study the objective was to find the temperature range within which the organics burn off at sufficient rate while minimizing the effect of oxidation of the SS430L metal. The first tests were to test individual organics including binder PVB and two types of pore former, PMMA, and Graphite. Then, the precursor metal powder with C1-SS430L 75wt% was also tested inside the TGA to see at what temperatures the organics burns out when mixed as a precursor metal powder. It was found that the burn-out temperature for graphite is quite high, around 700˚C; and more detailed burn-out tests were conducted to see if graphite can be used as a pore former or not. Lastly, a fraction of

the sintered metal support was tested inside the TGA to examine the oxidation behavior at operating temperatures at 600, 700, and 800˚C.

A 5˚C/min ramp from room temperature to 650˚C was used for PVB, PMMA, and DOP and a 5˚C/min ramp from room temperature to 800˚C was used for graphite. Figure 4-1 shows the TGA results for change in wt% of organics as a function of temperature.

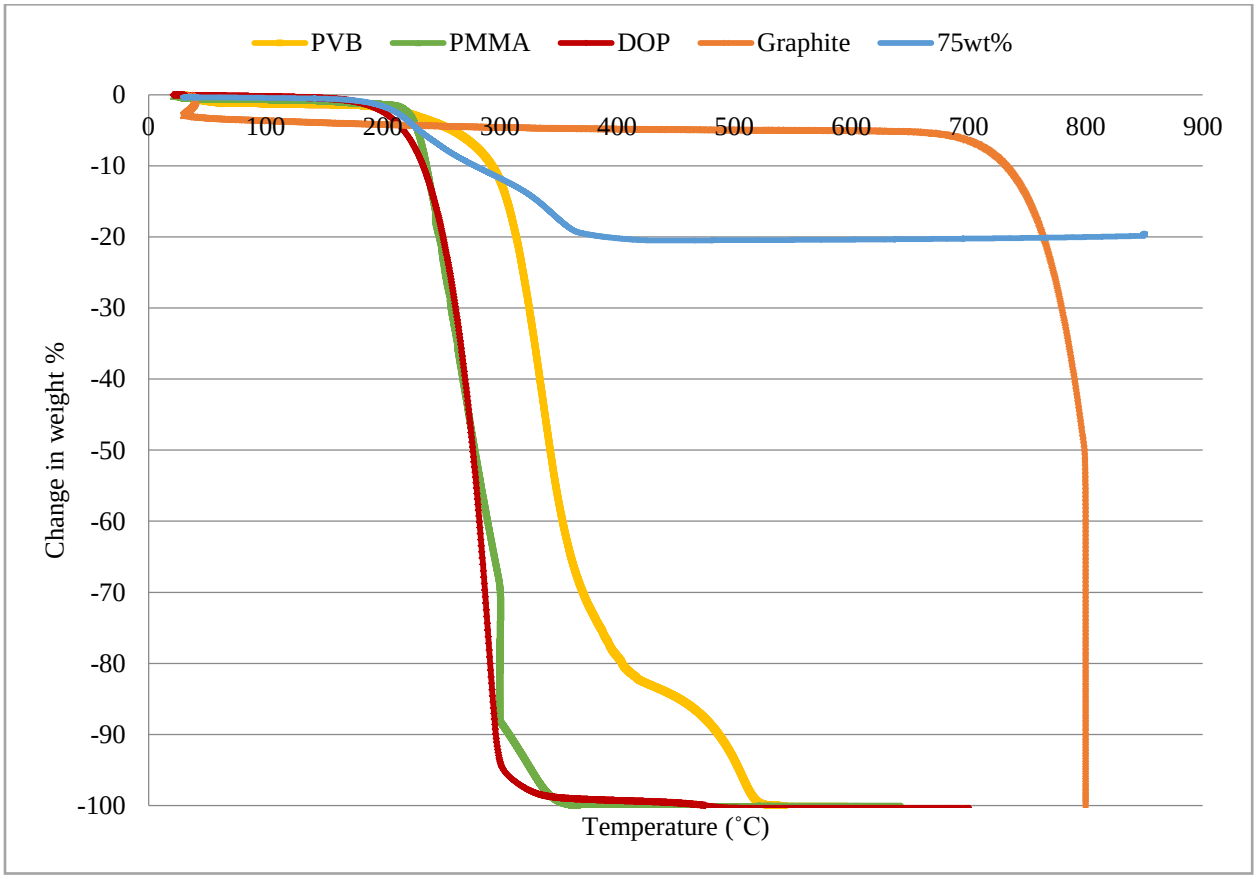

Figure 4-1 Burn-out results of PVB, PMMA, DOP, Graphite, and SS430L 75wt%

From Figure 4.1 it is seen that the PMMA is completely burned off at 400˚C and PVB rapidly starts to combust at 300-400 ˚C and slows down between 400 and 500˚C. DOP starts to burn out at 200 ˚C and is completely gone at 300 ˚C. However, when graphite is used, it only starts to burn-out at ~700˚C where SS430L rapidly oxidizes (see the next results). In order to see how the organics mixture behaves when mixed as a precursor solution, 75wt% powder made with PMMA as pore former was also tested inside the TGA. The temperature profile started from room temperature and ramped to 850˚C at a rate of 5˚C/min. It is shown that the organics mixture

consisting of PVB, DOP, and PMMA starts to burn off at 300 and completes the burn-out around 400-450˚C. Based on this result, the burn-out temperature for the organics with PMMA as a pore former was chosen to be 400˚C for 5 hours. It was also found that the change in weight starts to increase again at ~520˚C, which can be an indication of metal oxidation. Therefore, this burn-out profile at 400˚C ensures sufficient burn-out and limits the oxidation of the metal as much as possible.

Since the burn-out temperature of graphite alone was found to be ~700˚C, a detailed study of precursor solution with graphite as a pore former was tested inside the TGA. Figure 4-2 shows the TGA results of powder burn-out at 4 different temperatures: 400, 450, 500, and 600˚C.

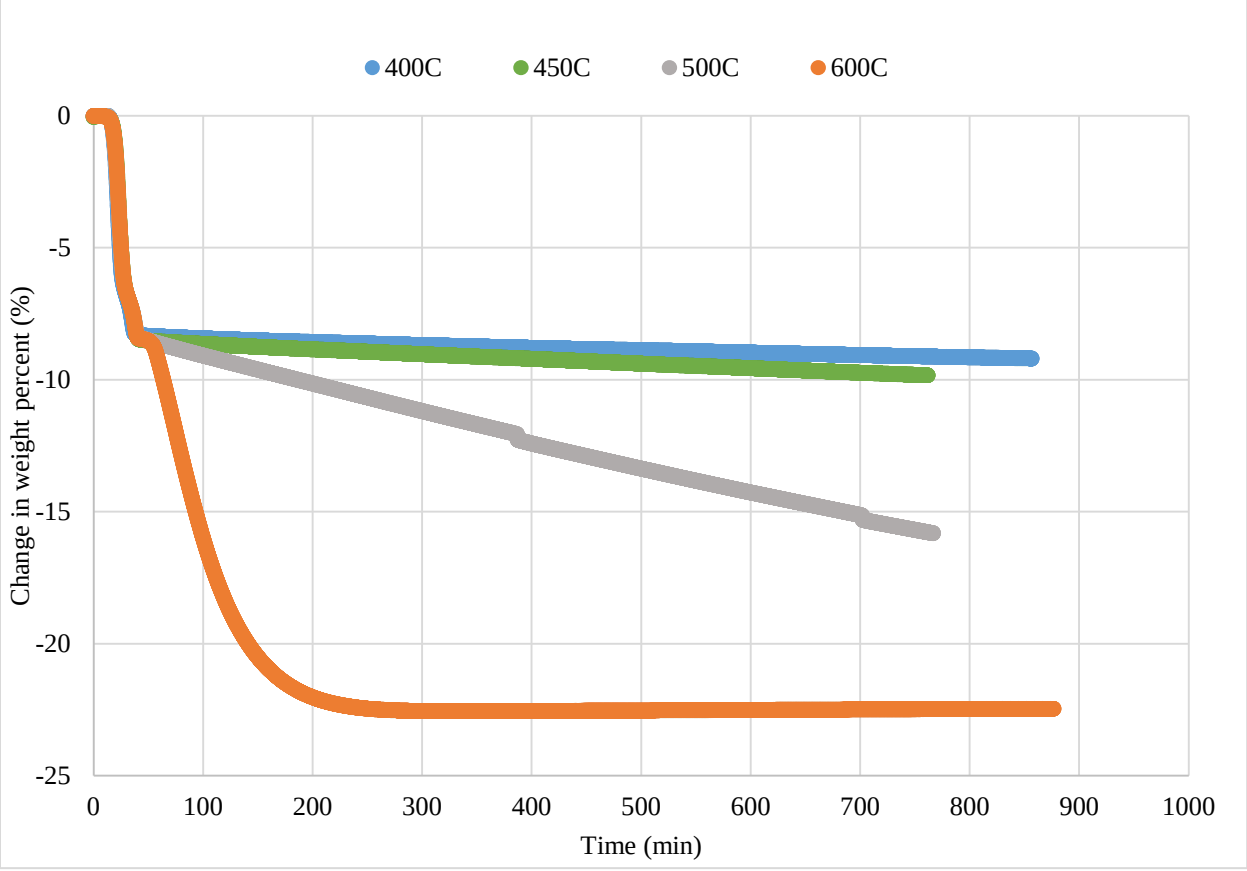

Figure 4-2 Burn-out of graphite precursor powders at various hold temperatures.

In this experiment, the burn-out rate of powder mixture with graphite as a pore former at various temperatures: 400, 450, 500, and 600˚C were tested in air. All experiments started from room

temperature with a ramping rate of 5˚C/min up to the hold temperatures and stayed for 10-12 hours. Solid loading was 75wt% and thus, the expected weight change due to burn-out is approximately −25wt%. As seen in Figure 4-2, −25% is not reached for all 4 temperatures. Also result for temperatures 400, 450, and 500˚C show that the burn-out rate was to too slow to be practical. Based on the rate of the burn-out at the given temperature the estimated time to complete burn-out was calculated with linear extrapolation and the results are shown in Table 4-1.

Table 4-1 Predicted complete burn-out times for temperatures of 400, 450, and 500˚C

Burnout Temperature (C)	Rate (wt%/min)	Time required to reach 75%
400	-0.001014	51 days
450	-0.001809	28 days
500	-0.01026	5 days

Only at 600˚C the combustion was carried out fast enough but even at the end it did not reach -25wt% and remained at -22~23wt%. This is possibly due to the remaining graphite or the deviation in powder compositions, and oxidation that also occurred. Nonetheless, 600˚C is still too high and should be avoided to prevent oxidization of the metal. Therefore, the use of graphite as a pore former was not pursued.

The next result in Figure 4-3 shows the oxidation behavior (i.e. experiments in air) of powder with PMMA as a pore former at 700, 800, and 900˚C. For this experiment, SS430L 75wt% powder was used. The temperature profiles are shown in Figure 4-3 as a secondary axis. Each profile started from room temperature, ramp to 400˚C at 5˚C/min, hold at 400˚C for 30 min and ramp to the final hold temperatures at 5˚C/min where it stayed for 8 hours.

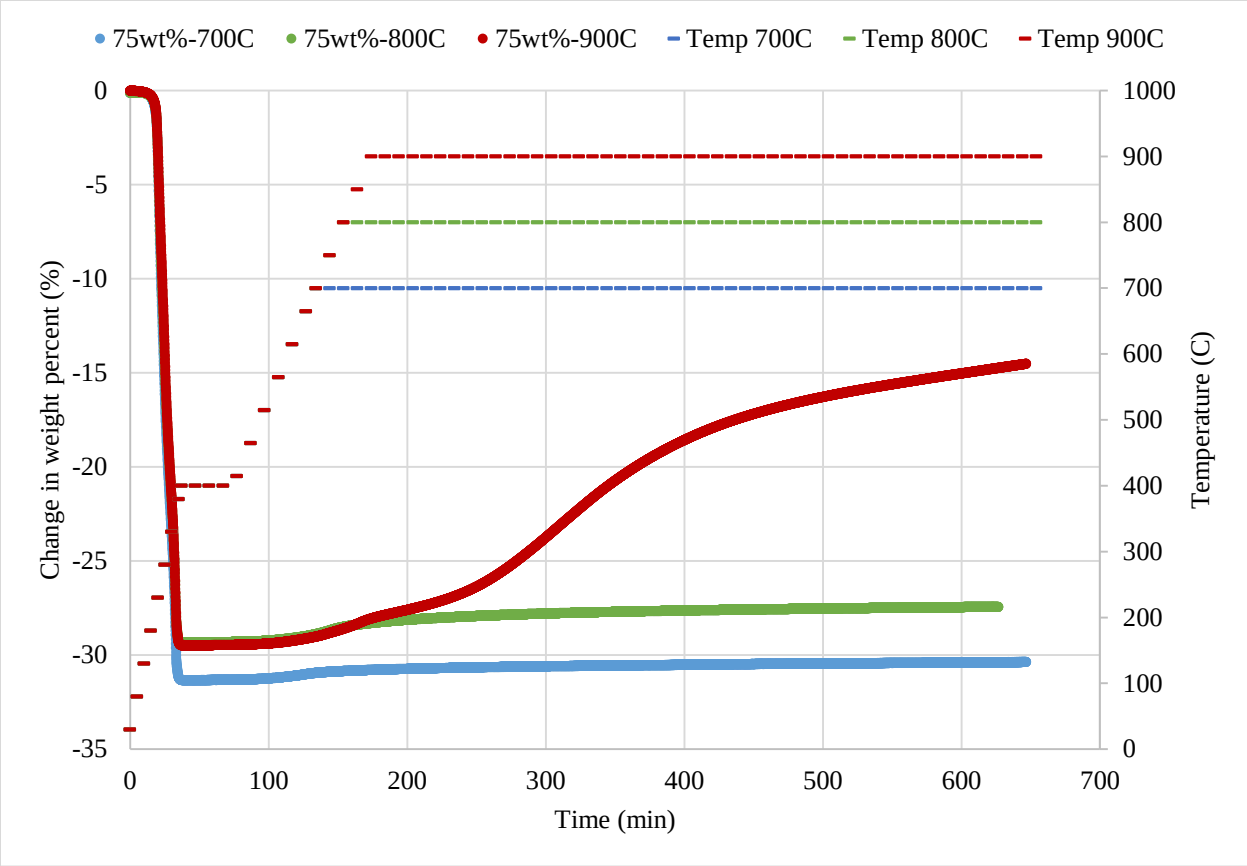

Figure 4-3 Oxidation behavior of precursor powder with PMMA as a pore former.

From this analysis it was found that the precursor powder can start to oxidize as low as ~520˚C and the oxidation reaction continues to increase at 700˚C. This confirms that the burn-out should be kept below 500˚C. It is important to switch the furnace gas to reducing atmosphere for the temperatures above 450˚C.

The last experiment conducted using the TGA was to analyze the oxidation of sintered metal supports at temperatures of 600, 700, and 800˚C. Those temperatures were chosen because those would be typical of intermediate temperature metal-supported SOFC operation. For these experiments, metal supports were made with PMMA as a pore former with stainless steel mortar. Two SS430L solid loadings: 80 and 95wt% samples were sintered inside a Mellen furnace using the temperature profile mentioned in Table 3-5. Once the sintering was properly completed the 20mm porous metal support disks were broken into smaller chunks (~1mm x ~1mm x ~1mm) to fit inside the TGA sample holder. Then these samples were tested in air starting from room

temperature with 5˚C/min ramp to the final hold temperature where it stayed for 12 hours. The results are shown in Figure 4-4.

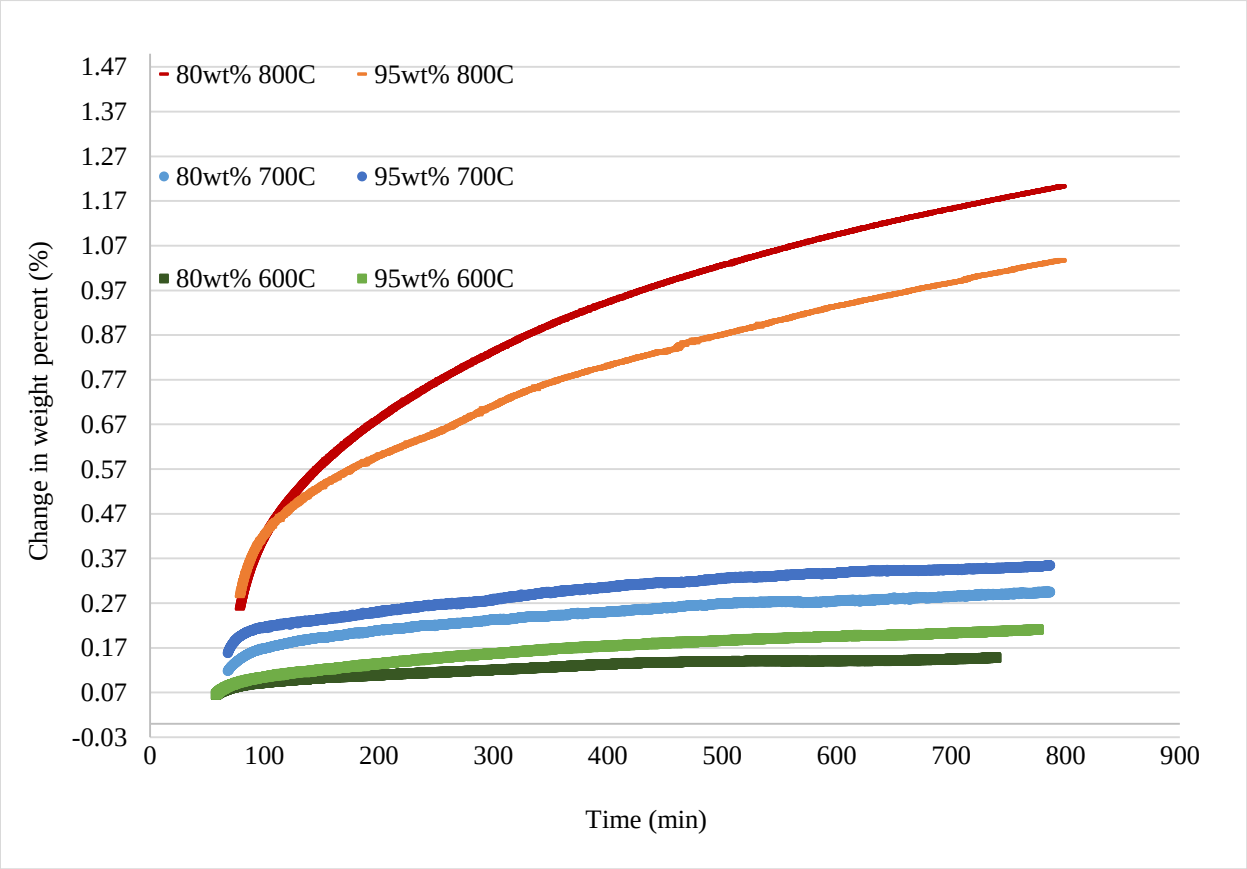

Figure 4-4 Oxidation resistance of sintered metal support with 80 and 95wt% at operating temperatures: 600, 700, and 800˚C.

Up to 700˚C the oxidation behaviour shows a relatively slower rate towards the end of 12-hour period compared to 800 ˚C. After 12 hours, at 600˚C the weight percent change is 0.15 and 0.21% for 80 and 95wt% respectively; at 700˚C it is 0.29 and 0.35% for 80 and 95wt% respectively, and 800˚C the oxidation is most rapid with maximum weight percent change of 1.2% and 1.05% for 80 and 95wt%, respectively, which is almost 8 times more than 80wt% at 600˚C and 5 times more than 95wt% at 600˚C. Assuming an almost linear increase in weight change after 12hours the rate of weight change is determined and shown in Table 4-2.

Table 4-2 the rate of weight change in different temperatures after 12hours

Temperature	Rate of weight change for SS430L 80wt% $\left(\frac{wt\%}{min}\right)$	Rate of weight change for SS430L 95wt% $\left(\frac{wt\%}{min}\right)$
600˚C	$6.36 * 10^{-5}$	$3.12 * 10^{-5}$
700˚C	$2.39 * 10^{-4}$	$1.03 * 10^{-4}$
800˚C	$3.43 * 10^{-4}$	$1.21 * 10^{-4}$

As seen in Figure 4-4, the rate of weight change after 12 hours (>720 min) is very slow for all temperatures and both compositions. However, the rate of weight change is still bit faster at 800˚C than 600˚C in magnitude of 5.4 times more for 80wt% and 3.9 times more for 95wt%. Also keep in mind that the metal support is likely to be on the anode side which it will not operate under air. Nonetheless a good redox cycle is still a desirable feature and these results show the operating temperature between 600-700˚C is ideal for SS430L metal support.

Study of burn-out and oxidation behaviour at various temperatures showed that the organics mixture with PMMA as pore former is more suitable for fabricating metal support. The burn-out should be carried at 400˚C and the furnace gas should be switched to reducing atmosphere above 450˚C since the metal can oxidize as low as ~520˚C. In terms of the oxidation behaviour, the oxidation reaction can occur at faster speed at 800˚C even though the weight change is 1.2% maximum after 12 hours. Based on this results, the investigated metal support (SS420L) should be suitable for operating temperature range between 600-700˚C, which are typical of intermediate temperature SOFC.

4.2 Determination of a Suitable Organics Mixture Composition

This study aimed at investigating the effect of individual organic components: binder (PVB), pore former (PMMA), and plasticizer (DOP). In order to measure the effect of pore former (PMMA), the precursor composition listed in Table 3-5 was used with SS430L 87wt%. The PMMA mass ratio among the organics mixture was varied from 1, 2, 3, 4 to 5 while the other organics (PVB and plasticizer) were kept at constant mass ratio of 1. Also SS430L was kept at 87wt%. From this analysis, all compositions were able to form fine powders and sintered to fabricate metal support pellets. However, for PVB:DOP:PMMA=1:1:1 and 1:1:5 the disk was warped and deformed after sintering and it was difficult to measure accurately the volume of these two sample cells. Since the highest and lowest PMMA contents caused fabrication problem, it was decided to keep the "middle" PMMA ratio of 3 in the subsequent studies on effects of PVB and DOP. For the effect of binder (PVB), organics mass ratio of PVB:DOP:PMMA=X:1:3 was used with 'X' being PVB content variation. For these measurements, the compositions shown in Table 3-6 were used. As the name implies, the role of the binder is to bind the particles together. Because of this, for high mass ratios of binder (i.e. 4 and 5), it was not possible to form powders; the precursor solution became a huge chunk and it was impossible to hand grind into fine powder form. Therefore, only ratios of 1:1:3, 2:1:3: and 3:1:3 could be used to fabricate the metal support. Even then, only PVB ratio of 1 was able to form flat disks and found to be the most suitable ratio.

Lastly, for the effect of plasticizer (DOP), organics mass ratios of PVB:DOP:PMMA=1:X:3 were used with 'X' being the DOP content variation (Table 3-7). However, for this test none of the precursor compositions worked except the 1:1:3 ratio. For the other ratios, the samples became thin film since the role of plasticizer is to make the composition more flexible and provide more plasticity. Compared to a fine powder these thin films would not break down to fine particles. Among all the organics composition tested, the ration of PVB:DOP:PMMA of 1:1:3 yielded the best result in the fabrication process and was thus selected as the most appropriate combination for the metal support fabrication. All results described in the rest of this thesis were obtained using PVB:DOP:PMMA mass ratio of 1:1:3

4.3 Sintering Results

The results of the relative green density and the relative sintered density were plotted for different SS430L solid loading samples from 3 batches of powder (C1, C2, S1). For each batch 6 metal disks per SS430Lwt% were used. Table 4-2 shows the number of disks made for each composition and for each batch.

Table 4-3 Number of disks made per batch per SS430Lwt%.

SS430L wt%	Ceramic Mortar (C1)	Ceramic Mortar (C2)	Stainless steel Mortar (S1)
80	6	6	6
85	6	6	6
87	6	6	6
90	6	6	6
95	6	6	6

For example, batch ‘C1’ with 80 wt% SS430L was used to make 6 disks to record green density, sintered density, and change in weight % before and after sintering. Then, the values from these 6 pellets were averaged for each analysis. This measurement process was repeated for the rest of SS430L wt% as well as for the other batches. Thus in total there were 18 samples per SS430Lwt% and 30 samples per batch. Overall, 90 disks (6 x15) were used for the three analysis including relative green density, relative sintered density, and change in weight percent before and after sintering.

After recording the relative green density for all three batches and for all SS430L solid loadings, Figure 4-5 is plotted. Figure 4-5, it shows a positive linear relationship between the relative green density and SS430L solid loadings.

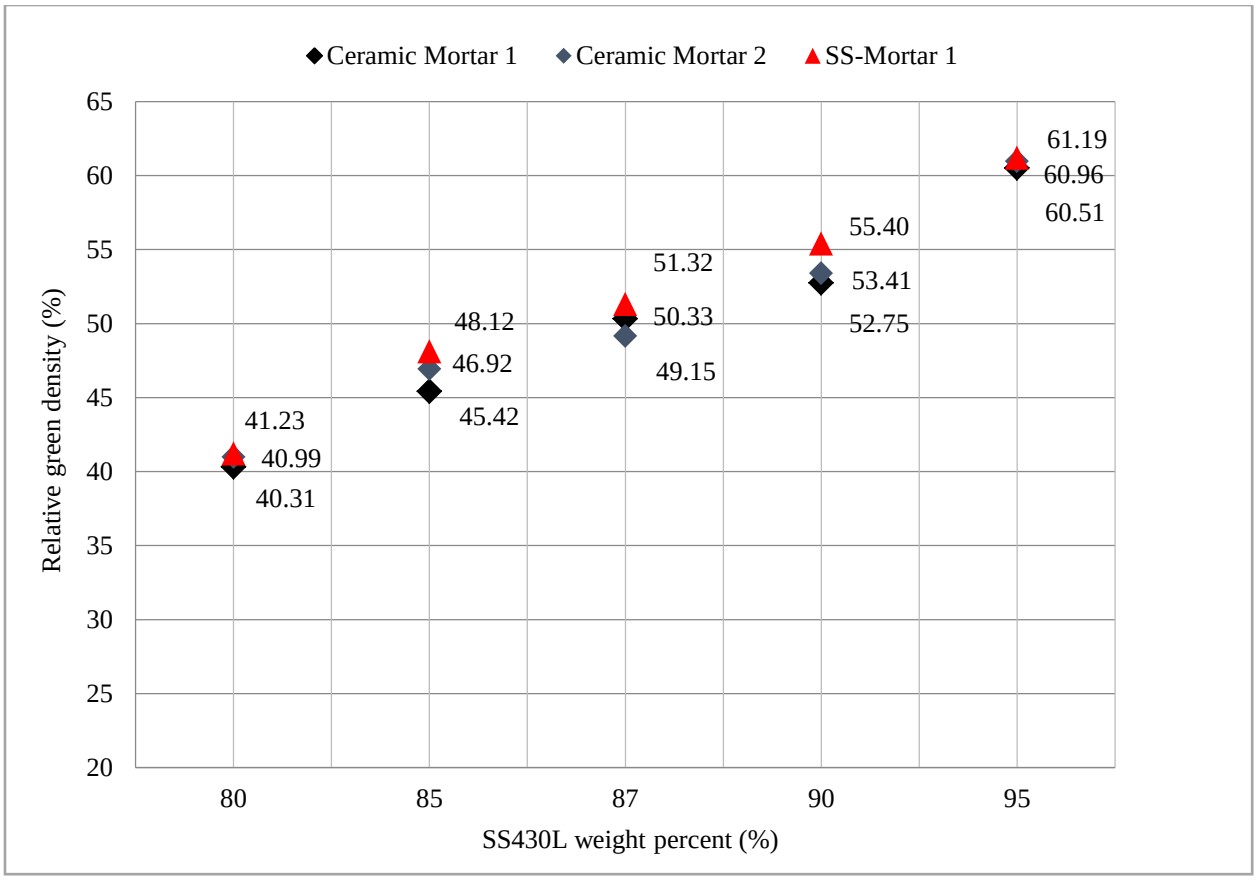

Figure 4-5 Average relative green density of different SS430Lwt% samples

As the metal content increases a higher green density is achieved with pressed green pellets. This implies that the powders compact more efficiently as the metal content is increased from 80 to 95wt%. The same trend is shown from all 3 batches, C1, C2 and S1. Samples from S1 have slightly higher value of average green density for all compositions compared to C1 and C2 samples. Statistical analysis (single-factor ANOVA) was conducted to verify if the difference in means is significant or not. The detailed calculations and results can be found in the Appendix 1. The ANOVA test verified that there is no significant difference in means for 80 and 95wt%. However ANOVA results for SS430L solid loadings of 85, 87, and 90wt% showed that the difference in means is significant. It was also attempted to measure the powder particle size distribution as another mean to verify the repeatability of the synthesis procedure. Laser diffraction analysis method was attempted but it was found not applicable due to the heavy density of the metal (optical particle size analyzer cannot use heavy metals). Therefore, only the green density measurement was used to assess the repeatability of the powder synthesis process.

The next analysis is between the relative sintered density and different SS430L solid loadings of the same disks that were used in the relative green density measurements.

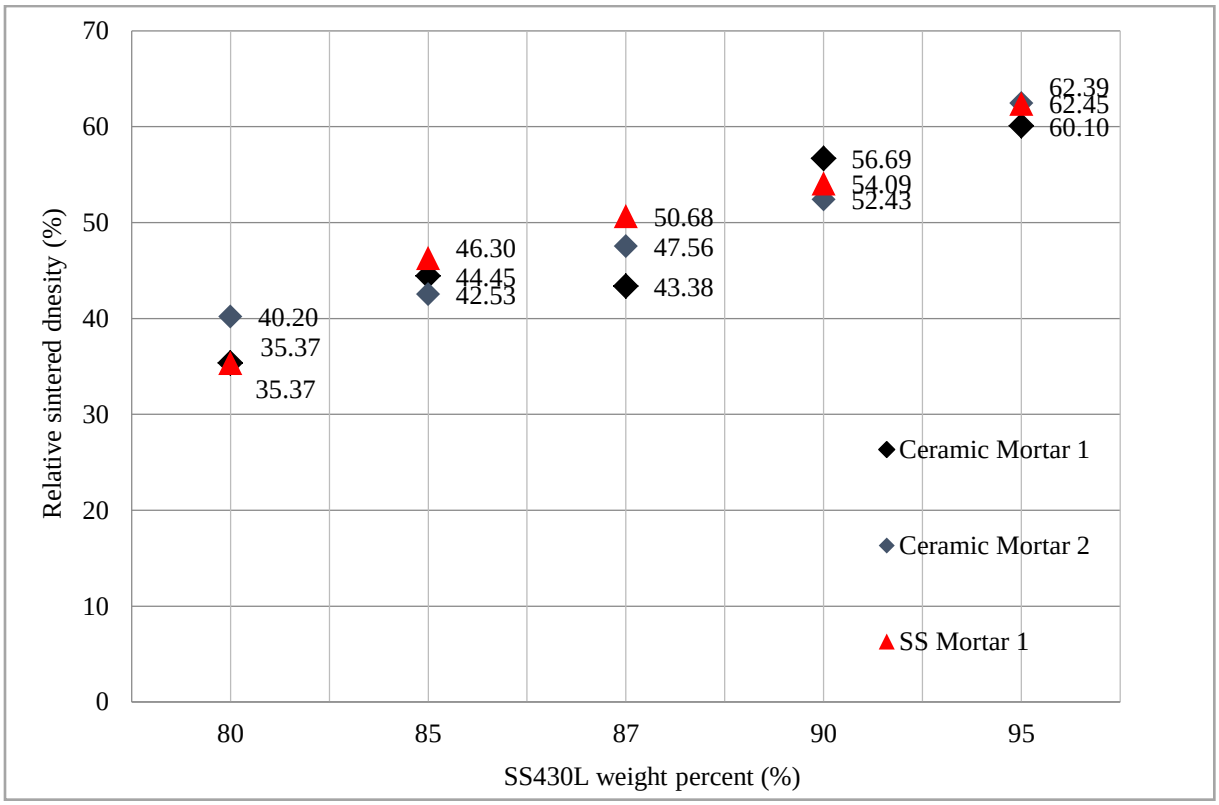

Figure 4-6 Average relative sintered density of different SS430L wt% samples

A similar linear trend between the relative sintered density and different SS430L solid loadings is shown in Figure 4-6. As the SS430L metal content increases the sintered density increases as well. Compared to Figure 4-5, the differences in the means of the three batches are more obvious in the sintered samples. In addition, there is no apparent difference in the type of mortars used since the variation using the same ceramic mortar gives similar variation as with the stainless steel mortar. As the next analysis, the means of 3 different batches were averaged to compare the relative green density and the relative sintered density. Figure 4-7 shows the comparison between the relative green and sintered densities of averaged 3 batches. The relative sintered density is lower than the green density for 80, 85, and 87wt% and similar or slightly higher for 90 and 95wt%. Here two phenomena can affect the relative density during the sintering process: 1) loss of the organics with the consequence of reducing the relative density and 2) shrinkage of the cell, which would increase the relative density. At lower SS430wt% loadings (i.e. higher

organics content), the effect of organics loss dominates, hence the reduction in relative density after sintering. As the SS430wt% increases, the reduction in relative density is less and less important, and at the highest SS430 loading, the relative density increased slightly after sintering, which was due predominantly to shrinkage of the cell. The percentage difference between the relative green density and the relative sintered density is -9.5, -5.1, -6.1, +1.0, and +1.2% for 80, 85, 87, 90, and 95wt% respectively. It is possible that having more metal content beyond 90wt% can provide further sintering due to efficient initial packing of the particles. For 90 and 95wt%, the relative green density is 55.40 and 61.19%, respectively. In other words, starting with a relative green density higher than 52.75% can improve the sintering process and thus result in higher relative sintered density. Whereas the lower metal content below 90wt% and relative green density lower than 51.32% results in less dense structures.

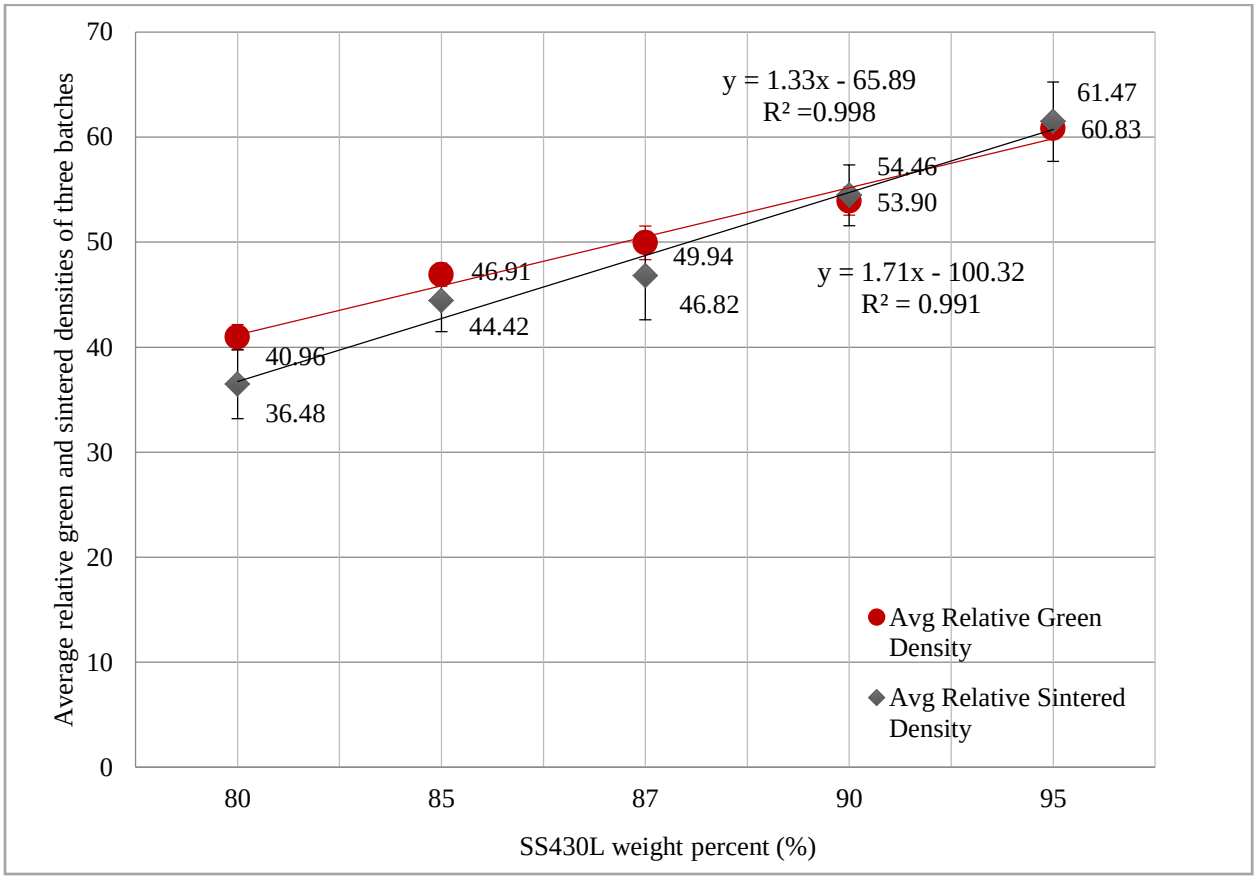

Figure 4-7 Average relative green and sintered densities for the three batches

The linear fit for the average relative green density is plotted with slope of 1.33 and y-intercept at -65.89 with standard errors of 0.0285 and 2.503 respectively. The linear fit for the average

relative sintered density has a slope of 1.71 and y-intercept at -100.32 with standard errors of 0.0957 and 8.377 respectively. The standard errors for slope and y-intercepts are slightly higher for the average relative sintered density than the average relative green density. This is due to the larger variation observed in the relative sintered density measurements.

The sintering behavior was also analyzed by measuring the change in weight of the metal support pellets before and after sintering. During the burn-out process in air, the organic contents are supposed to combust away leaving only the metal behind. Once the organics are completely burnt out, the remaining metal goes through the high temperature reducing atmosphere sintering process at 1100˚C. Thus it is expected that a certain change in weight will occur based on the different SS430L solid loadings. Figure 4-8 shows the results of change in weight percent for 3 batches of powders in varying SS430L contents.

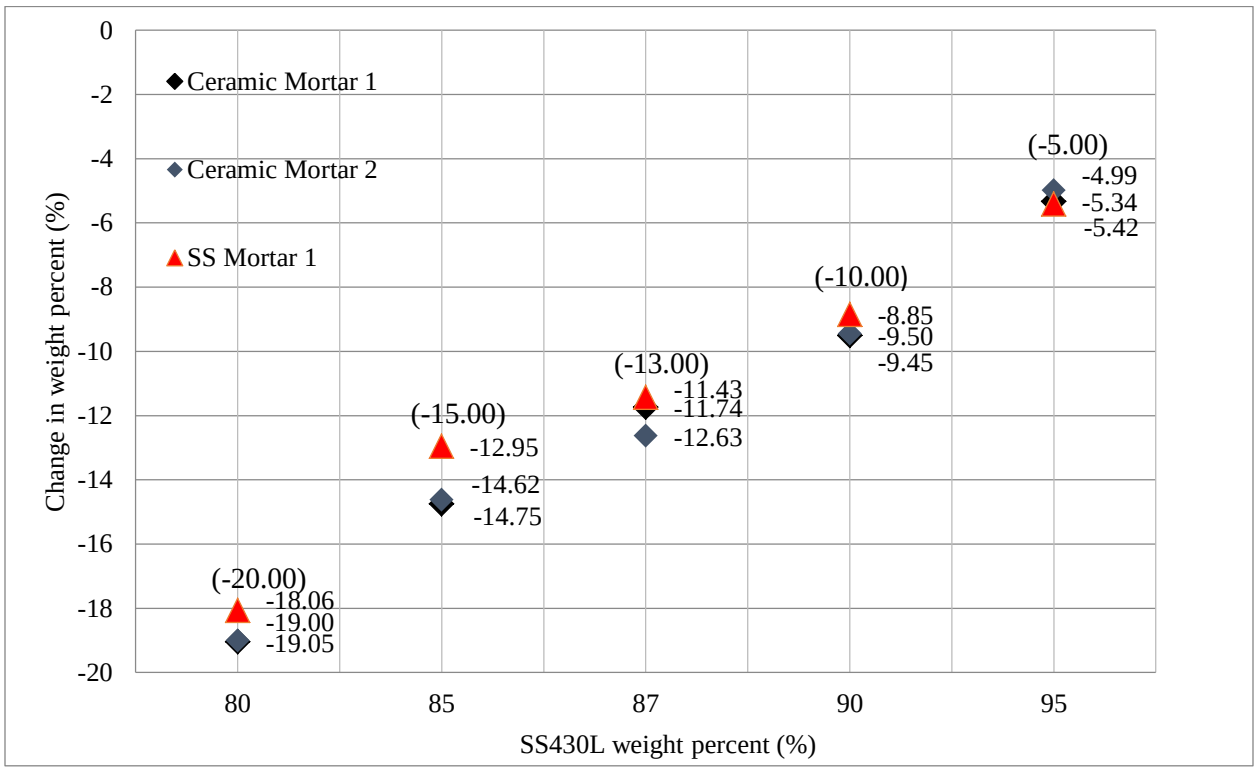

Figure 4-8 Change in weight percent before and after sintering for different SS430L wt% samples . The values in between brackets are expected weight changes, depending on the SS430 loading.

In figure 4-8, a linear trend is shown for all 3 batches of powders with varying SS430L wt% where, as expected, the higher the metal content, the lower the change in the weight percent before and after sintering. The values of change in weight percent before and after sintering are similar to those of the expected values. For example, for 80wt% metal sample, it is expected to burn-out 20wt% of the organics during the burn-out stage. As shown in the plot above, the change in weight percent values at 80wt% are 19.05, 19.00, and 18.06% for C1, C2, and S1, respectively. The margin of errors with change in weight percent varies from -6.73 to 9.70% for C1, 0.23 to 5.49 for C2, and -8.32 to 13.65 for S1 samples for all SS430Lwt% samples. Also, for 80, 85, 87, and 90wt% the change in weight percent is below the expected values whereas for 95wt% the change in weight is more than the expected values (expect C2). Based on this result, it is difficult to determine the cause of the error or variances. It is possible that the organic were not completely burnt-off and at the same time the metal was oxidized. Alternatively, the errors can be coming from the fabrication process when each composition was measured using the scale and the measurement error associated with the scale itself as well. Table 4-3 shows the analysis results of change in weight percent with means, standard deviation (Stdev), and percent error (% error).

Table 4-4 Analysis of change in weight percent before and after sintering

	Ceramic Mortar 1			**Ceramic Mortar 2**			**SS-Mortar 1**		
SS430L wt%	Means	Stdev	% error	Means	Stdev	% error	Means	Stdev	% error
80	-19.05	0.29	4.77	-19.00	0.46	4.98	-18.06	0.91	9.68
85	-14.75	0.90	1.64	-14.62	0.15	2.53	-12.95	0.47	13.65
87	-11.74	0.24	9.70	-12.63	0.71	2.84	-11.43	0.63	12.07
90	-9.50	0.90	4.96	-9.45	0.11	5.49	-8.85	0.44	11.45
95	-5.34	0.59	-6.73	-4.99	0.11	0.23	-5.42	0.17	-8.32

The percent errors vary from -6.73 to 9.70% for C1, from 0.23 to 5.49% for C2, and from -8.32 to 12.07 for S1. The percent errors for change in weight percent seem to be higher for S1 samples. The standard deviation values varies from 0.24-0.9 for C1, 0.11-0.71 for C2, and 0.17-0.91 for S1 which show similar ranges for all three batches.

Based on the sintering results analysis, the relationship between the relative green density and SS430L solid loadings, and the relationship between the relative sintered density and SS430L solid loadings were determined to be a positive linear fit. The change in weight percent of before and after sintering was investigated to compare the actual weight change values to the expected values. The actual weight change % is close to the expected values with errors of ~4.6% in average. The three batches of samples showed the same trend in all three measurements and it seems like there is no significant difference in between the use of ceramic mortar and stainless steel mortar.

4.4 Porosity Results

The porosity was measured using three methods. The first one is Archimedes method based on ASTM standard C373-88 which is labeled as ASTM (P1), the second method used optical analysis labeled as Optical (P2) and the last method was using the full density of solid SS430L from the reference value of 7.65g/cm^3 and labeled as Calculated (P3). The details of each method are mentioned in the experimental procedures.

In Figure 4-9 the results of using ASTM (P1) and Optical (P2) are included. Table 4-4 summarizes all porosity measurements for the three methods. For this study, four sets of measurements were made for porosity. The first set is for the powder made using ceramic mortar and using ASTM standard porosity measurements and is labeled C1-ASTM. The second set is for the powder made from C2 batch and using ASTM standard porosity measurements and is labeled C2-ASTM. The third set is for the powder made using stainless steel mortar and using ASTM porosity measurements and is labeled S1-ASTM. Last is for the powder made using stainless steel mortar using optical analysis and is labeled S1-Optical. In figure 4-9, the four measurements show that as the solid loading is increased the porosity decreases. For example, C1-ASTM (Ceramic 1 by ASTM porosity measurement) has the following results: porosities for SS430Lwt% of 80wt%, 85wt%, 87wt%, 90wt% and 95wt% are 61% (±0.025), 48% (±0.016%), 48% (±0.05%), 41% (±0.018%) and 36% (±0.05), respectively.

As expected, having more pore former in the mixture creates more pores during the burn-out stage, thus increasing the porosity of the metal support. It is difficult to say whether there is a

significant discrepancy between powders made with ceramic mortar vs. stainless steel mortar. The ASTM standard method and optical analysis method seem to have the same trend and similar values. As mentioned previously, there is no standard for porosity. However, further investigation through performance tests will better delineate the effect of porosity on performance. Performance evaluation is a part of future work.

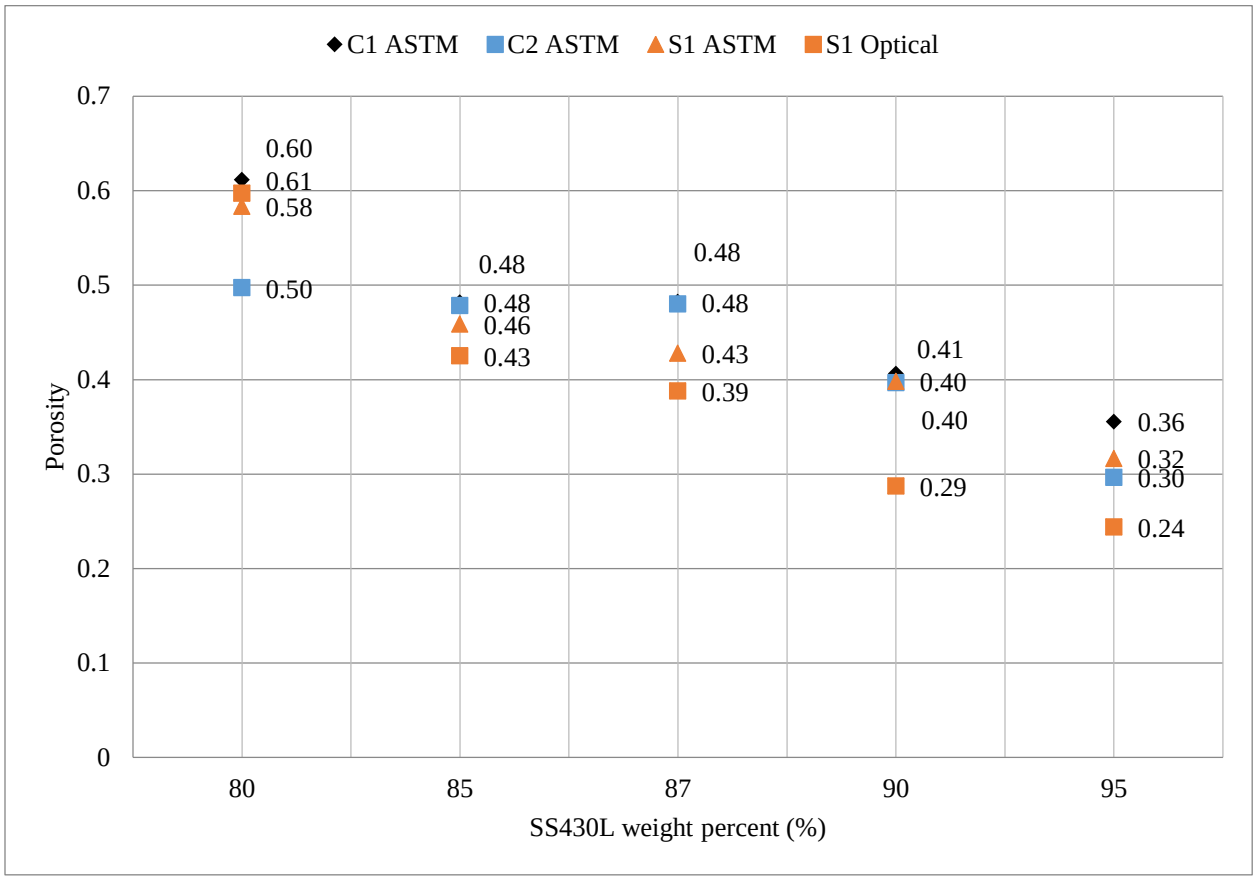

Figure 4-9 Porosity measurements of sintered SS430L samples

Table 4-5 Porosity measurement of sintered SS430L samples

Summary Table							
	ASTM (P1)			Optical (P2)	Calculated (P3)		
SS430L wt%	C1	C2	S1	S1	C1	C2	S1
80	0.61	0.50	0.58	0.60	0.65	0.60	0.65
85	0.48	0.48	0.46	0.43	0.56	0.57	0.54
87	0.48	0.48	0.43	0.39	0.57	0.52	0.49
90	0.41	0.40	0.40	0.29	0.43	0.48	0.46
95	0.36	0.30	0.32	0.24	0.40	0.38	0.38

As seen in Table 4-4, for all three measurement methods, including the Calculated (P3), the trend is the same such that increasing the solid content decreases the porosity for all three batch of powders. For the ASTM (P1) and Calculate (P3) measurements, the values from the three batches were averaged and standard deviation values were calculated, as seen in Table 4-5. For the optical analysis (P2), only S1 batch was measured but 2 samples per wt% was obtained.

Table 4-6 Average and standard deviation of porosity measurements

	ASTM for C1, C2, S1		**Optical for S1**		**Calculated for C1, C2, S1**	
SS430L wt%	Avg	Std.S	Avg	Std.S	Avg	Std.S
80	0.56	0.06	0.24	0.01	0.63	0.03
85	0.47	0.01	0.29	0.08	0.56	0.02
87	0.46	0.03	0.39	0.03	0.53	0.04
90	0.40	0.01	0.43	0.01	0.46	0.02
95	0.32	0.03	0.60	0.01	0.38	0.01

Measurement errors vary between 0.01-0.06 for ASTM(P1) methods, 0.01-0.08 for the Optical (P2) method and 0.01-0.04 for the Calculated (P3) method. Figure 4-10 shows the effect of relative density on porosity (based on ASTM method) for both green and sintered samples.

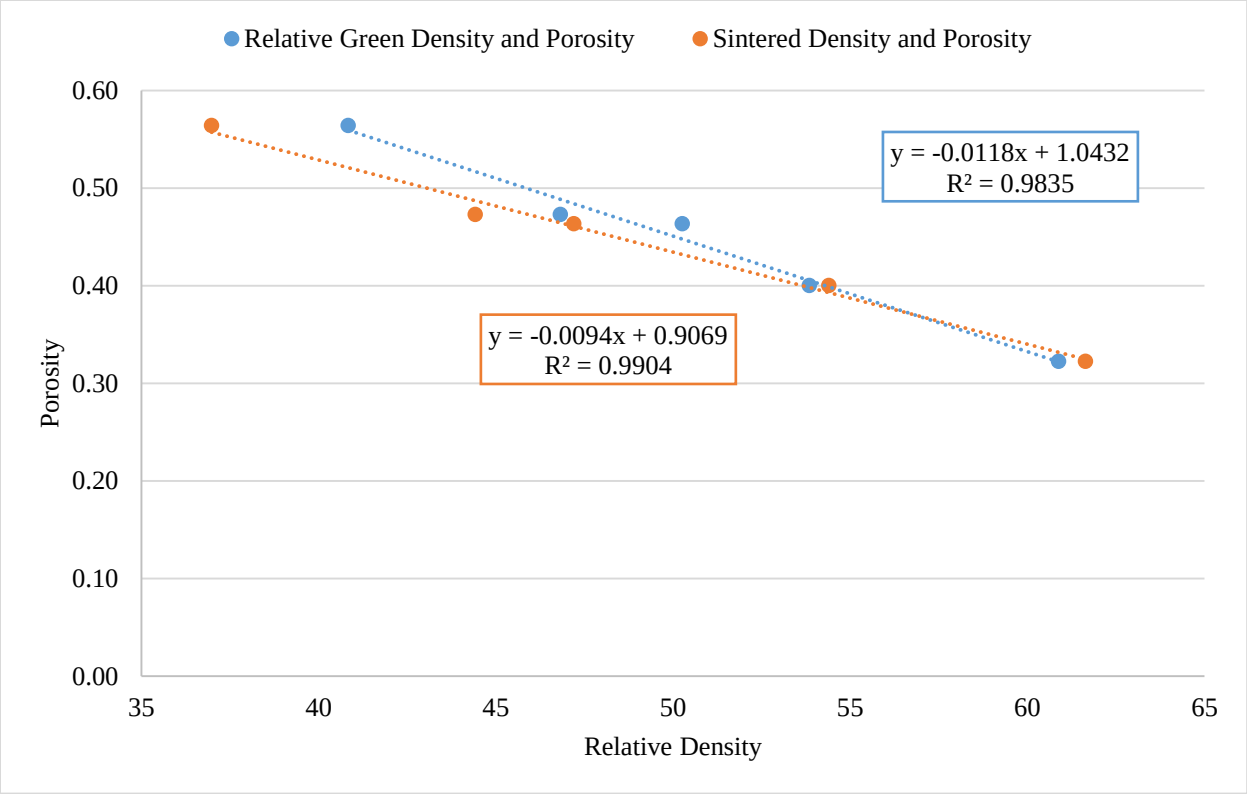

Figure 4-10 ASTM porosity values versus the average relative green density (blue) and the average relative sintered density (orange)

From figure 4-10, both the porosity versus the relative green density and the porosity versus the relative sintered density have negative linear relationship. Using this graph and linear fit equation, one can calculate the approximate porosity knowing the relative green density and the relative sintered density as below.

$$Porosity = -0.0118\ (\pm 0.00089)(relative\ green\ density) + 1.0432\ (0.0452) \quad (4.1)$$

$$Porosity = -0.0094\ (\pm 0.00054)(\text{relative sintered density}) + 0.9069\ (0.0266) \quad (4.2)$$

The standard error values for the slope and y-intercept are slightly lower for Equation 4.2 than Equation 4.1. Since the ASTM was measured for the sintered disks, the average relative sintered density measurements shows slightly better linear fit than the average green density. Nonetheless, both equations are quite similar to each other.

From the optical analysis, microstructure images were taken for different SS430L solid loadings and are shown in Figure 4-11.

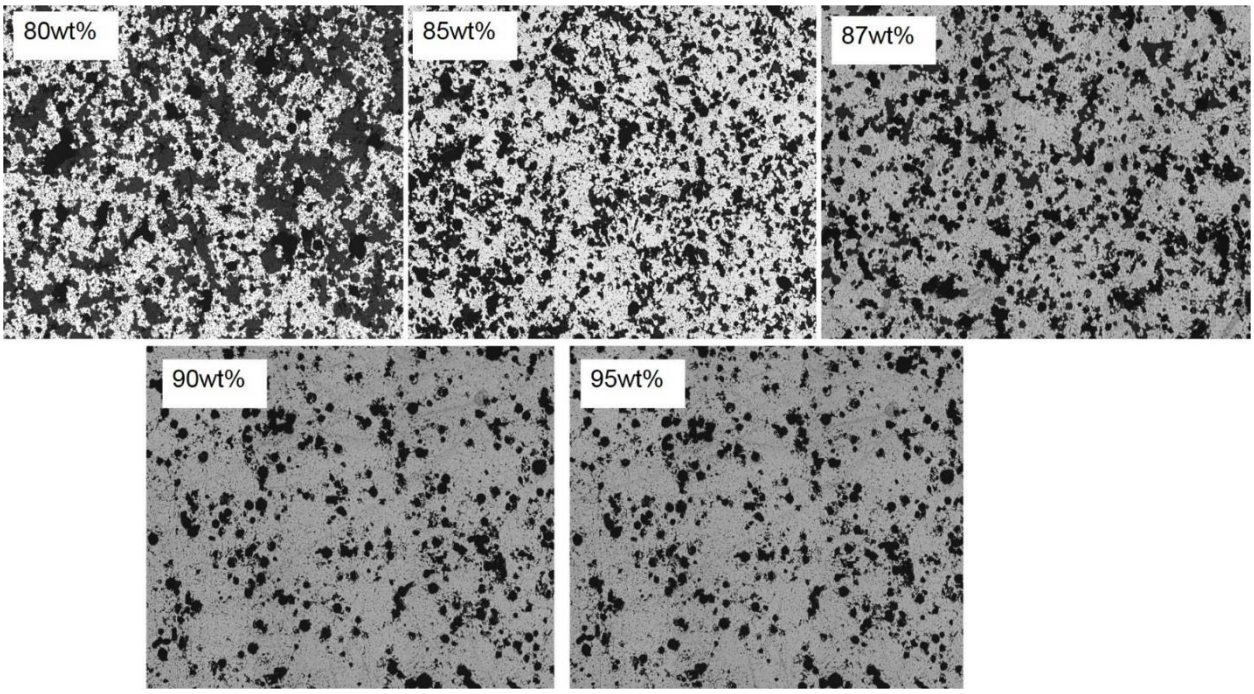

Figure 4-11 Optical analysis of different SS430Lwt% samples

These images were taken at 5x magnification. Based on these images, the increase in solid loading of SS430L wt% shows much less pores. For example the dark areas that represent pores is much less in 95wt% compared to 80wt%. Thus the overall trend is same for all three porosity measurements.

The next study measures porosity to investigate the effect of pore former (PMMA) and binder (PVB). For the study on the effect of PMMA, the powder compositions listed in Table 3-5 were used with SS430L 87wt%. The amount of PMMA mass ratio was varied from 1,2,3,4, to 5 while the other organics (PVB and plasticizer) were kept at constant mass ratio of 1. The organics mas ratio used can be written as: PVB:DOP:PMMA=1:1:X. Where 'X' shows the variation in PMMA contents. The metal disks were sintered the same way as mentioned before (Refer to the procedures in 3.1 and 3.2). In order to measure the porosity, ASTM (P1) and Calculated (P3) were used. In Figure 4-12 the porosity measurements are shown for varying amount of PMMA content.

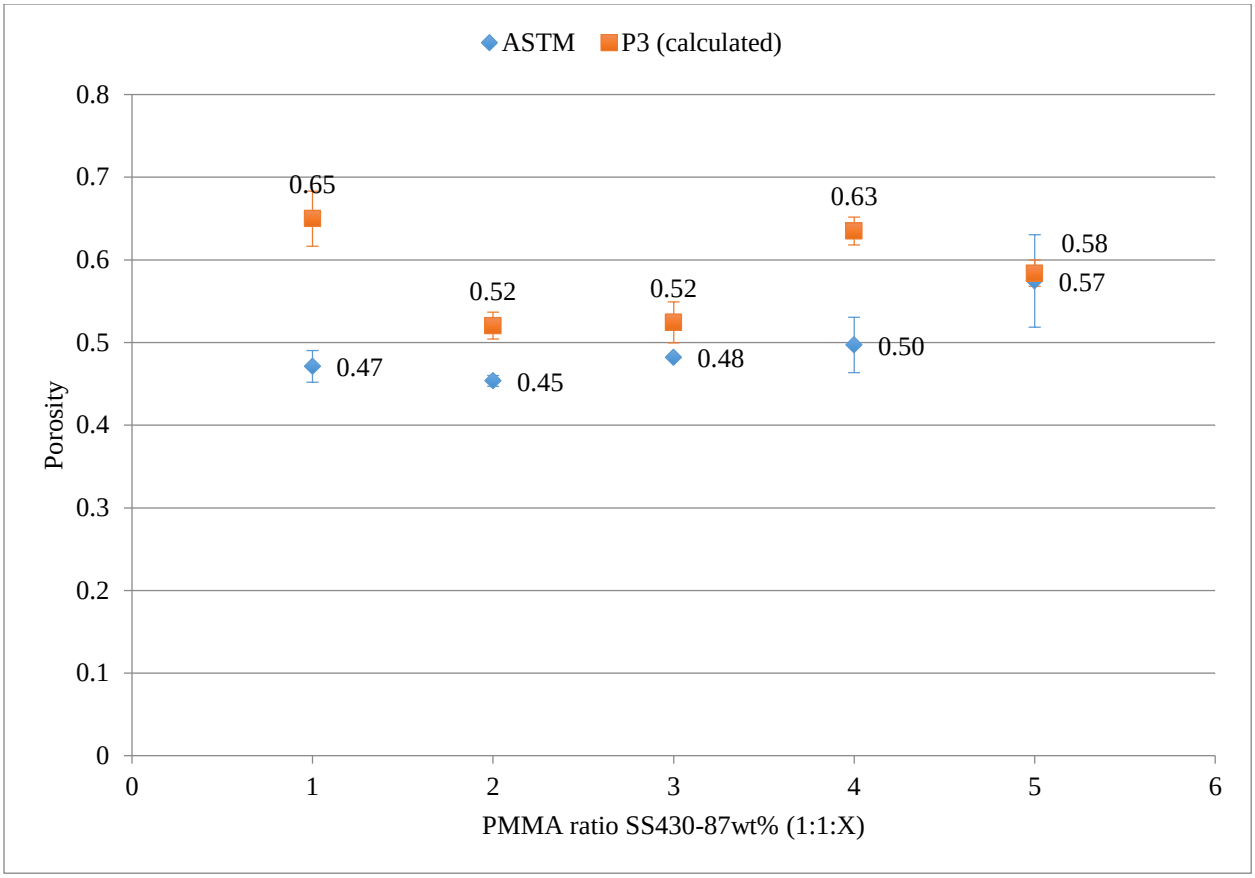

Figure 4-12 Effect of PMMA on porosity

Looking at the ASTM (P1) values, the increase in PMMA content increases the porosity except for the ratio 1:1:1. This trend is expected since the function of PMMA is used to make pores. From the ASTM (P1) values, the lowest porosity is 0.52 at ratio 1:1:2 and the highest porosity is 0.65 at 1:1:1. From the Calculated (P3) values seem to have the same trend where the lowest porosity is 0.45 at ratio 1:1:2 and the highest porosity is 0.57 at ratio 1:1:5. Both ratios 1:1:1 and 1:1:5 resulted in warped shape after sintering. This made the dimension measurements of the sintered disks inaccurate which affected the accuracy of both ASTM (P1) and Calculated (P3) methods. Also the difference between P1 and P3 is larger at the ratio of 1:1:1 due to more deformed shape. In order to achieve a flat disk, the ratio (1:1:3) was found to be the most suitable. Although the discrepancies within the measurements was kept relatively small, for varying PMMA ratios of 1, 2, 3, 4, and 5, the error bar values for the ASTM (P1) methods are ±0.019, ±0.007, ±0.00058, ±0.033, and ±0.056, respectively. For Calculated (P3) methods, the

error bar values are ±0.033, ±0.016, ±0.025, ±0.017, ±0.016 in the same order of varying PMMA amount.

The next study was to investigate the effect of binder, PVB. For these measurements, the compositions in Table 3-6 were used. The PVB content was varied for mass ratios of 1, 2 and 3 while keeping the plasticizer and PMMA at 1 and 3. Recall from section 4-2 that it was not possible to form fine powder for binder ratio above 3. Organics mass ratio of PVB:DOP:PMMA=X:1:3 was used with 'X' being PVB mass ratio. Also a constant weight percent of SS430L, 87wt%, was used. Figure 4-13 shows the effect of binder, PVB, content on the porosity measurements. ASTM (P1) and Calculated (P3) methods were used to measure the porosity.

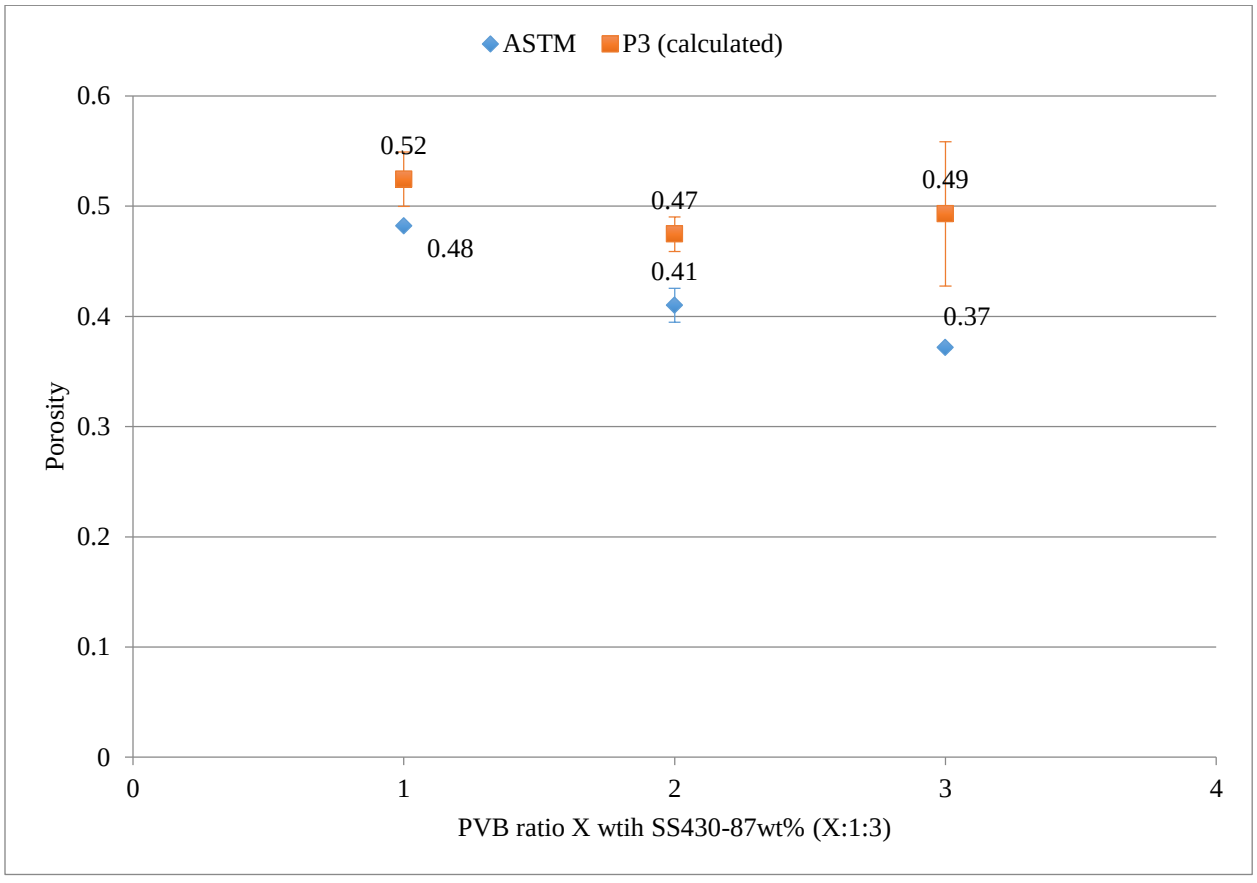

Figure 4-13 Effect of binder, PVB, on porosity

In Figure 4-13 the results shows that increasing binder content decreases the porosity. From the P3 measurements the porosity decreases from 0.52 for PVB ratio at 1 down to 0.47 for PVB ratio

at 2. However at PVB ratio 3, porosity increases slightly to 0.49. From the ASTM (P1) measurements, porosity decreases continuously in order of 0.48, 0.41 to 0.37 as PVB ratio increase from 1, 2, 3 respectively. Also, the discrepancies between P1 and P3 values increase as the binder contents increases. These discrepancies occur because increasing binder content deformed the metal pellet shape during sintering. Sintered metal pellets warped and expanded and it was difficult to accurately measure the diameter and height of these samples. Consequently the P3 values were not accurate and more discrepancies were shown with the error bars. For the PVB ratio of 1, 2, and 3 the error bar values of P3 measurements are ±0.025, ±0.016, and ±0.065 respectively. On the other hand the errors were much less when using ASTM (P1) method. For the PVB ratio of 1, 2, and 3, the error bar values are ±0.00059, ±0.015, and ±0.0016 respectively.

Lastly, a similar study was conducted to measure the effect of plasticizer (DOP) and different compositions of varying DOP precursor solutions were made as listed in Table 3-7. However, as mentioned before, appropriate quality of powder was not achieved for plasticizer ratio different than 1, and the porosity was, therefore, measured.

The overall assessment of the porosity measurements determined the relationship between the porosity and different solid loading of SS$30L samples. A linear fit between the porosity and the average relative green/sintered densities were determined. The effect of pore former, PMMA, and binder, PVB, were investigated through porosity measurements as well. As the name of these organics suggests, an increase in PMMA content increases the porosity whereas the increase in PVB content decreases the porosity from 0.48 for PVB ratio of 1 down to 0.37 for PVB ratio of 3. It was also observed that organics ratios other than PVB:DOP:PMMA=1:1:3 resulted in deformed shapes and some ratios failed at powder formation. PMMA ratios of 2, 3, 4 showed flat disks without any severe deformation after sintering. This implies that varying the PMMA content has a more flexibility and can be used to vary the porosity from 0.45 for PMMA ratio of 2 to 0.50 for ratio of 4 based on the ASTM method. Overall the PVB:DOP:PMMA ratio of 1:1:3 is found to be the most appropriate for metal support fabrication.

4.5 Coefficient of Thermal Expansion Results

The coefficient of thermal expansion was measured using a dilatometer in argon with sintered metal support samples with different SS430Lwt%. For this study, different solid loadings of SS430L wt%: 80, 85, 87, 90, and 95 were made with the ceramic mortar (C1) and the stainless steel mortar (S1). Metal supports were sintered as described in 3.3.4. In order to eliminate the effect of atmosphere on CTE measurements, argon was selected as an inert gas for this test. Two measurements were taken per SS430L solid loading and indicated with CTE1 being the first sample and CTE2 being the second sample as a repeat.

Figure 4-14 shows the dilatometer results of change in linear expansion over time for C1-CTE1 samples. Discrepancies between the measurements are present and it seems like there is no apparent consistency.

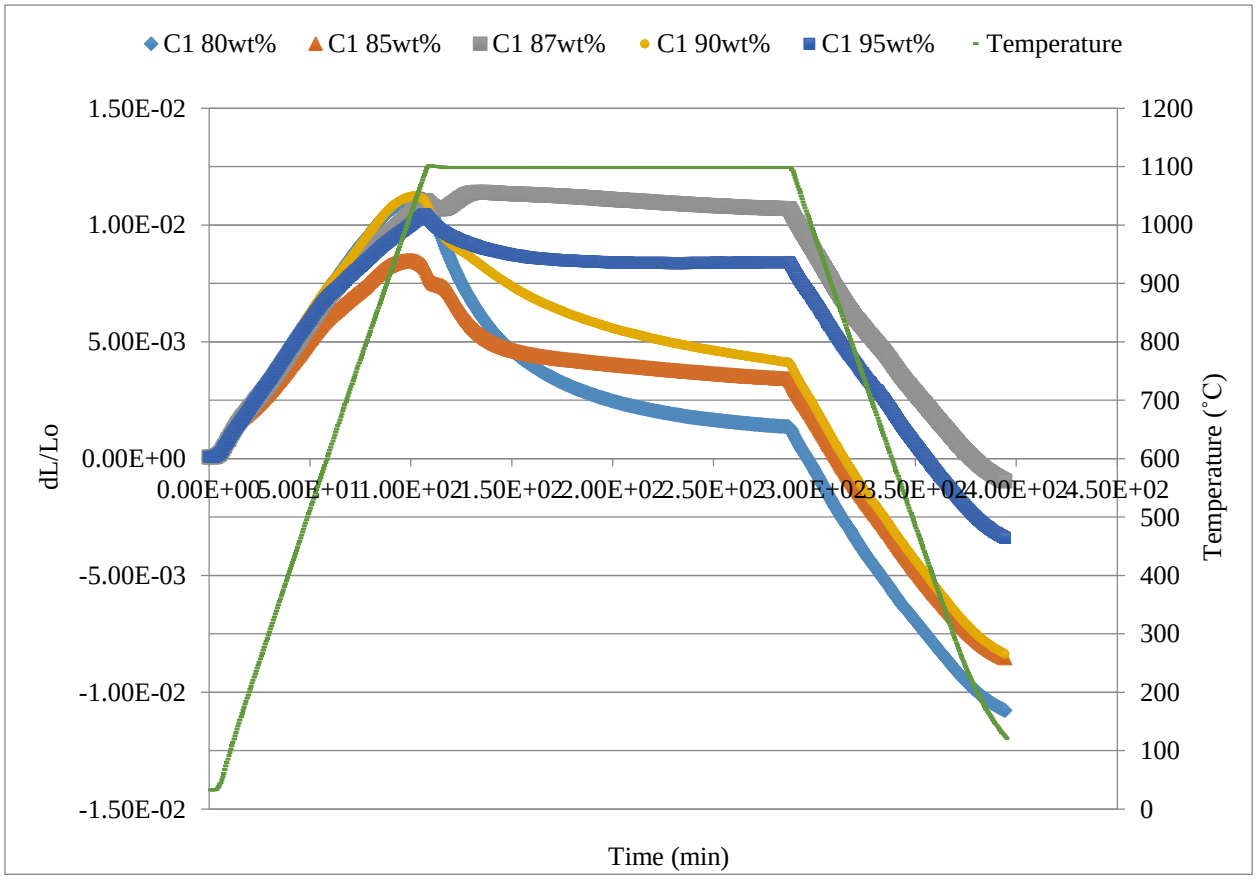

Figure 4-14 Dilatometer results of C1-CTE1 samples with different SS430Lwt%.

For comparison, the dilatometer results of change in linear expansion over time for S1-CTE2 samples are also shown in Figure 4-15.

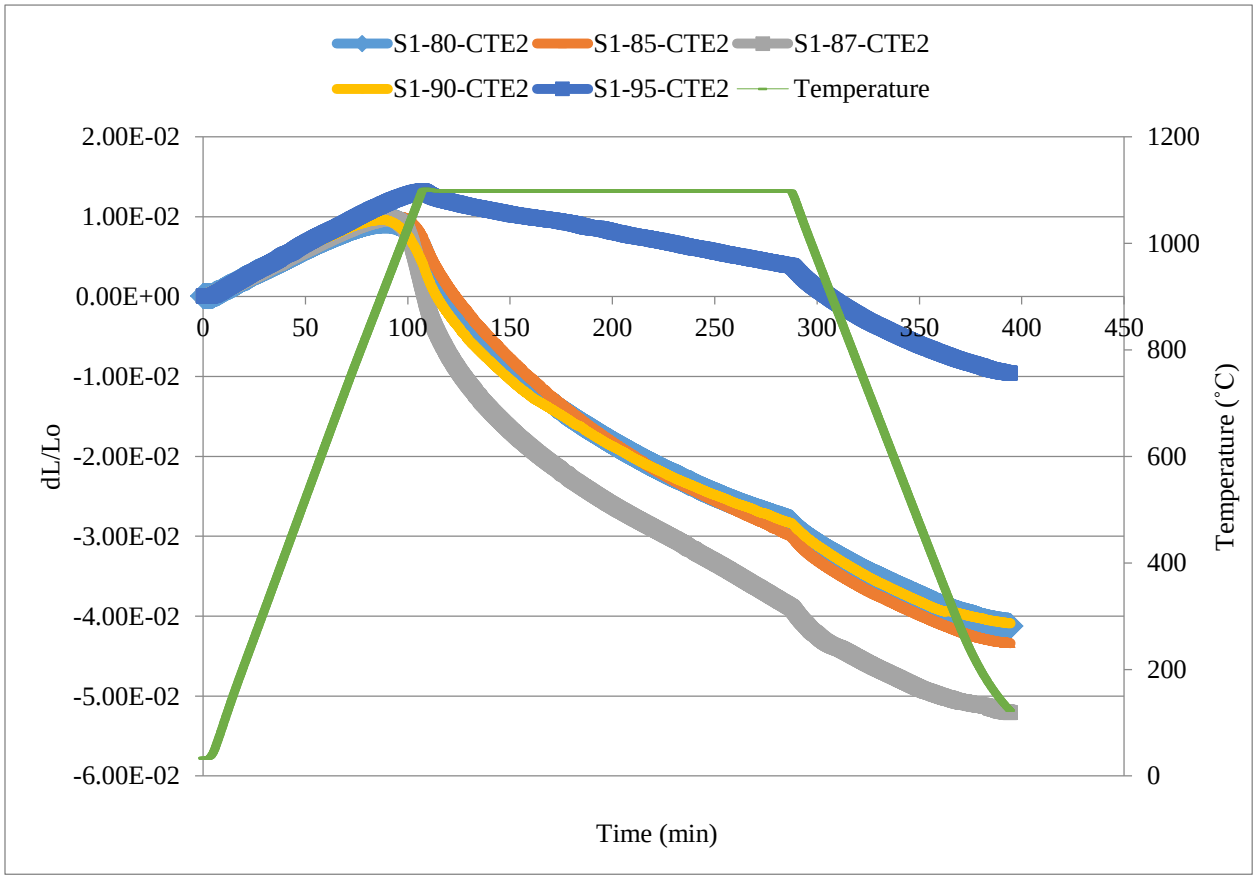

Figure 4-15 Dilatometer results of S1-CTE2 samples with different SS430Lwt%

Comparing S1-CTE2 to C1-CTE1 samples, discrepancies between the measurements are less in Figure 4-15 than Figure 4-14 and the results seem more consistent between S1-80, 85, and 90.

Table 4-7 shows the final CTE results calculated from 30-900˚C.

Table 4-7 CTE results of different SS430Lwt%

	C1 (Ceramic mortar 1)		S1 (Stainless steel mortar 1)	
SS430L wt%	CTE1 (ppm/K)	CTE2 (ppm/K)	CTE1 (ppm/K)	CTE2 (ppm/K)
80	10.9	11.9	10.8	10.9
85	9.5	9.3	10.9	12.6
87	10.9		12.0	11.2
90	11.0	12.0	11.6	11.0
95	12.2	10.5	11.0	13.1
100	13. 1			
YSZ, GDC (Tucker, 2010)	10-12			
SDC(FuelCellMaterials)	12.7			

It is difficult to say that there is a clear trend of how SS430Lwt% affects the CTE values. Since CTE is a physical property, it is expected that change in SS430L solid loadings will have minor effect on CTE. More importantly, it is critical to have similar CTE values to those of anode and electrolyte materials such as SDC to prevent warping and delamination of the layers. Comparing the CTE values of SDC (12.7 ppm/K) and metal support samples, they are all close to each other, albeit a bit lower for the fabricated porous metal supports.

It was found that the sintered metal support expands between 30-900˚C and there is change in slope (slight decrease) between 900-1100˚C, which indicates that there is one kind of shrinkage starting around 900˚C. After 3-4hours hold at 1100˚C most measurements plateaued and completed shrinkage which can be due to the further sintering. Based on these results, it was postulated that the shrinkage that initiates around 900˚C is possibly due to the phase change of the metal alloys transforming from ferrite to austenite or delta phase. Differential scanning calorimeter, DSC, analysis was done on SS430L powder to verify this.

Figure 4-16 shows the results of energy (mW/mg) observed in the DSC measurements for the SS430L powder. Argon gas was used as an inert atmosphere and the following temperature profile was used: room temperature to 1100˚C at ramping rate of 10˚C/min and cool down. The results shows that there is a distinctive energy peak around ~900-1000˚C which is the same range where the dilatometer results showed the change in slope for the linear expansion values. The DSC measurement was repeated on the same sample twice to see if this phase change

around ~900-1000˚C is repeatable or not. It was found that the phase change was indeed repeatable.

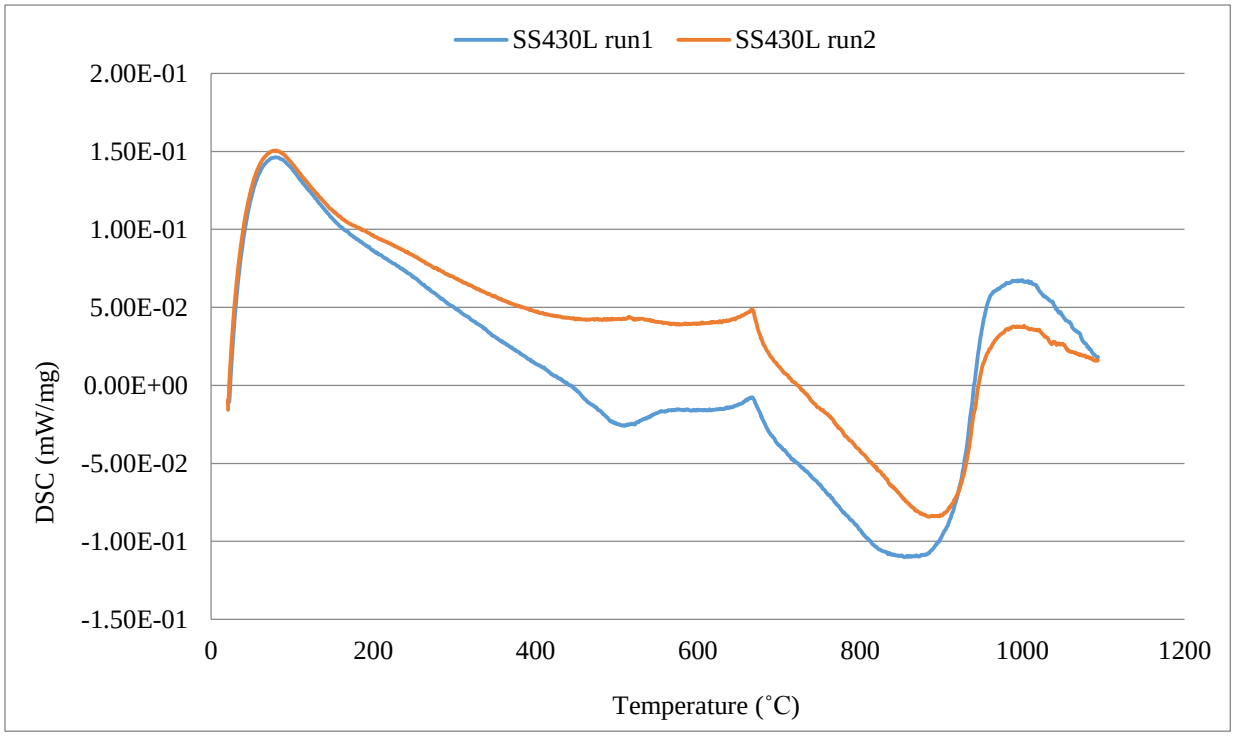

Figure 4-16 DSC results of SS430L powder

The magnitude of run1 and run2 are different (possibly due to oxidation of the sample during run 1) however the trend is the same. The DSC results was merely used to verify that there is a phase change of the FeCrSiC alloy occurring during the CTE measurements and it will likely occur each time the metal support is heated above 900˚C.

Figure 4-17 shows the pseudo phase diagram of Fe-Cr-C alloy with 17%Cr content which is very similar to SS430L composition (Fe:Cr:Si:C=82.6:16.5:0.5:0.02 wt%). At 900˚C near ~0 carbon wt%, there is a phase change present from alpha-iron phase (ferrite), to delta-iron and gamma-iron (Asutenite). Based on this phase diagram and the DSC results, the decrease in slope from dilatometer measurement at ~900˚C is not due to sintering but due to phase change of SS430L alloy.

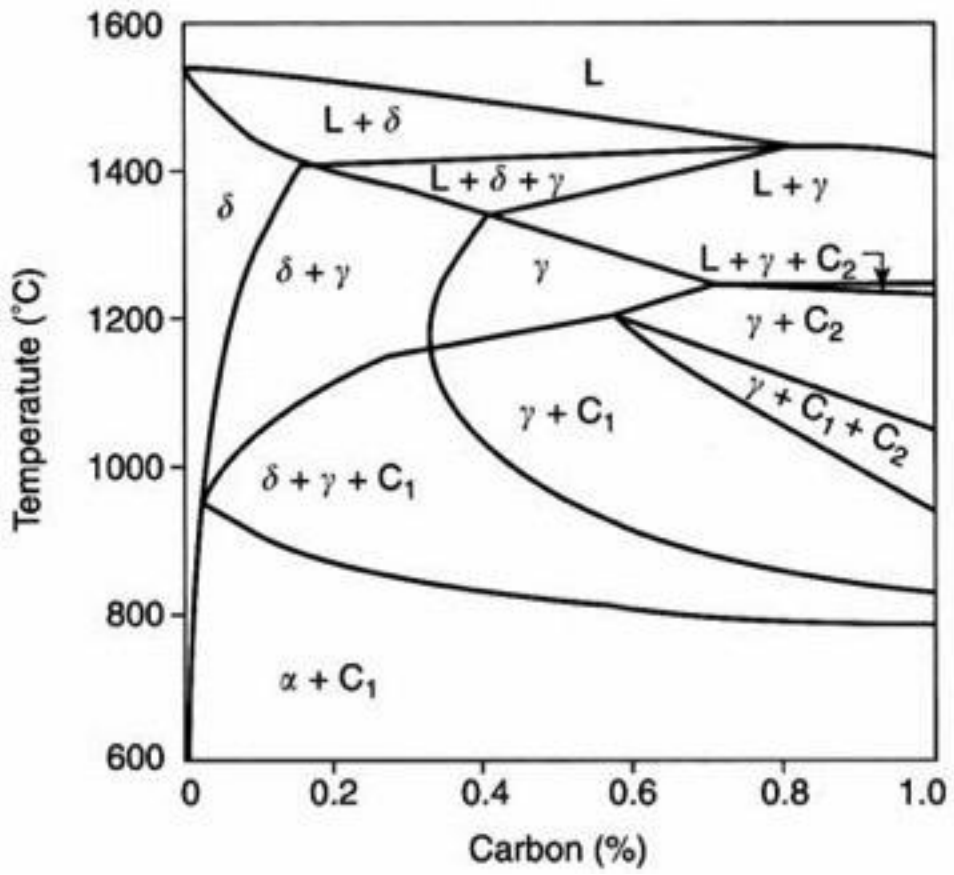

Figure 4-17 Fe-Cr-C pseudo phase diagram with 17wt%Cr (Lippold & Kotecki, 2005)

The CTE measurements showed that the sintered metal supports have similar CTE values to that of the anode and electrolyte material, SDC. The effect of different SS430L solid loadings presented discrepancies in the CTE values without significant trend. Future work includes the examination of the effect of sintering atmosphere on the CTE values of the metal support. This is important since the sintered metal support will be coated with the anode slurry and electrolyte slurry via vacuum slurry coating technique. Once the anode and electrolyte layers are deposited on the sintered metal support, a co-sintering process in reducing atmosphere up to 1100-1200˚C is required. Therefore the CTE values in this atmosphere can be useful for determining the co-sintering temperature profile and effect of reducing atmosphere.

4.6 Electronic Conductivity Results

Electronic conductivity of sintered metal support pellets were measured inside the SOFC testing station for operating temperatures ranging between 550 and 800°C. Higher electronic conductivity is expected from the metal support compared to the anode material (Ni+SDC) since metallic alloys have generally higher electronic conductivity than ceramics. In addition, most of the interconnect materials are made with metal alloys to have sufficient electronic conductivity to work as SOFC component. The effect of temperature on metal support electronic conductivity is evaluated and shown in Figure 4-18.

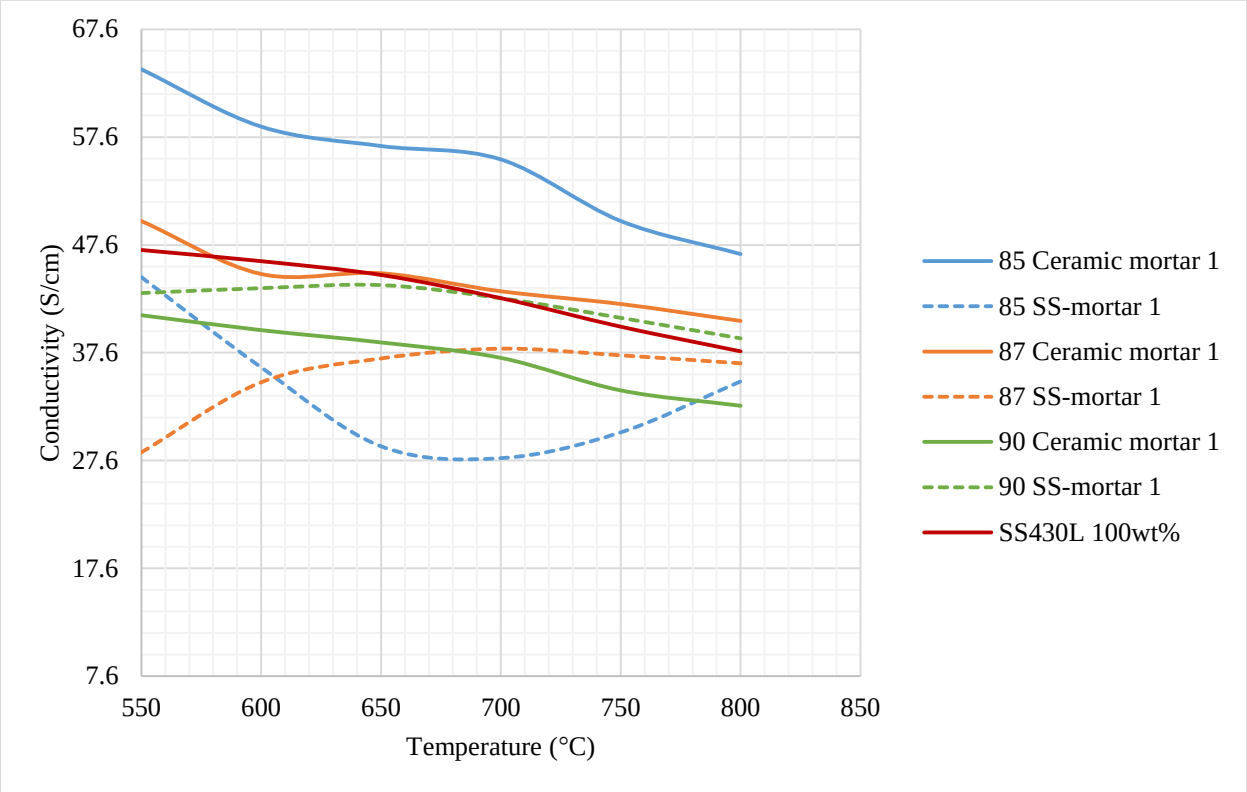

Figure 4-18 Electronic conductivity in argon for different SS430Lwt% samples

The electronic conductivity of different SS430Lwt% samples shows the same trend: as the temperature increases from 550˚C to 800˚C the conductivity decreases. The highest conductivity was measured from 85-ceramic mortar sample with 63.88 S/cm at 550°C and 55.53S/cm at 700°C. At 700°C the lowest conductivity is 27.84S/cm for 85-SS-mortar sample. The known value of stainless steel electronic conductivity is roughly 1.45×10^6 S/m at 20°C. In comparison, the results shown above are significantly lower by magnitude of $\sim 10^5$. However increase in

temperature is known to decrease the electronic conductivity of metals and the values shown above are much higher than that of ceramic electrode layers. It is possible that the particular fabrication method and the porous structure might have affected the electronic conductivity differently than the solid stainless steel. The next characterization is the analysis of the microstructure using SEM. It was found that a unique microstructure was obtained by the particular fabrication method that might have contributed to the much lower electronic conductivity of the sintered metal supports.

4.7 SEM Results

SEM images were taken for C1 batch with 80, 87, 90, and 95wt% SS430L samples. Figure 4-19 represents the SEM images at 100x magnification which show visible pores and microstructures. These images do not reflect the differences in porosity from lower solid loading sample to higher solid loading sample. However, the pore sizes of each sample seems to be similar to one another and this is because the same organic ratio was used for all samples

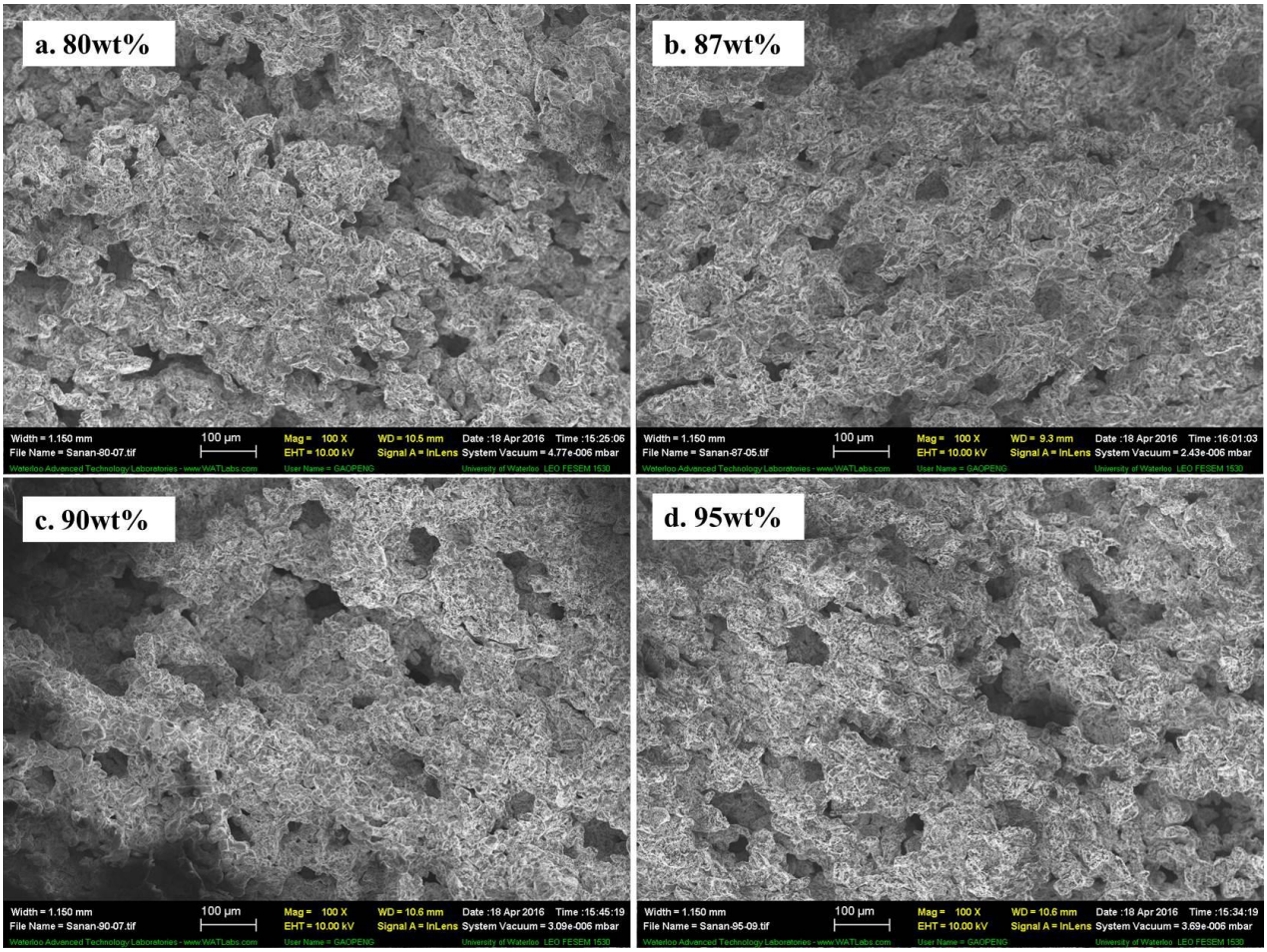

Figure 4-19 SEM of different C1 SS430Lwt% samples

SEM images show that brighter small particles are covering the whole surface of the porous metallic structure. At first this it was not clear what these particles were. So the same C1 samples were analyzed with EDX and these small particles were made of mostly Si, Cr and oxygen. On average, for all 5 different SS430L solid loadings the EDX results showed the composition of the substrate as Fe:Cr:Si:O=61.33:17.31:9.76:11.32 wt%. Higher Si and oxygen wt% implies that these white particles are likely silica oxide and chromium oxide. One should keep in mind that EDX is limited to certain areas where the analysis is performed thus the quantitative measurements have errors but at least it indicates a significant presence of the Si and Cr oxide scales. Based on the amount of these particles and how it was covering basically the entire surface, the use of the ceramic mortar was questioned since the mortar was made of silica oxide. There was a possibility that the use of the ceramic mortar contributed to increased Si content

during the hand grinding process. Thus the stainless steel mortar was used to see if these particles disappear.

Figure 4-20 shows the SEM images comparing the sintered samples from the ceramic mortar (C1) and the stainless steel mortar (S1). The SEM images were taken for C1:80 and 95wt% and S1:80 and 95wt% at higher magnification of x1000. Albeit the expectation, Figure 4-20 shows that both C1 and S1 samples are covered with the same particles. EDX was performed on S1 samples to determine chemical elements and it was again mostly Si and oxygen with 39.8 and 50.3 wt%, respectively. Unlike the prediction, the sintering results are the same for C1 and S1 powders. Since SS430L powder composition is Fe:Cr:Si:C=82.9:16.5:0.5:0.02 it is possible that Si and Cr diffuse to the surface during high temperature sintering and form oxide scales to prevent oxidation of iron. From the literature reviews it was commonly reported for SS430L that Cr is diffusive and chromia oxide scale is formed on the surface of metal particles to prevent oxidation. It was reported that formation of silica oxide can help the adhesion of chromia oxide scale to the surface of metal such that it assists on reducing oxidation of iron. It was also reported that Si varying from 0.017-0.05wt% is sufficient enough to produce SiO_2 layers in thin film or island structures between the metallic substrates and chromia scale (Jo et al., 2015). Since Si oxide scale is highly insulating it is not ideal for the SOFC application and desirable metal support layer should have minimum Si content if possible (Jablonski & Sears, 2013).

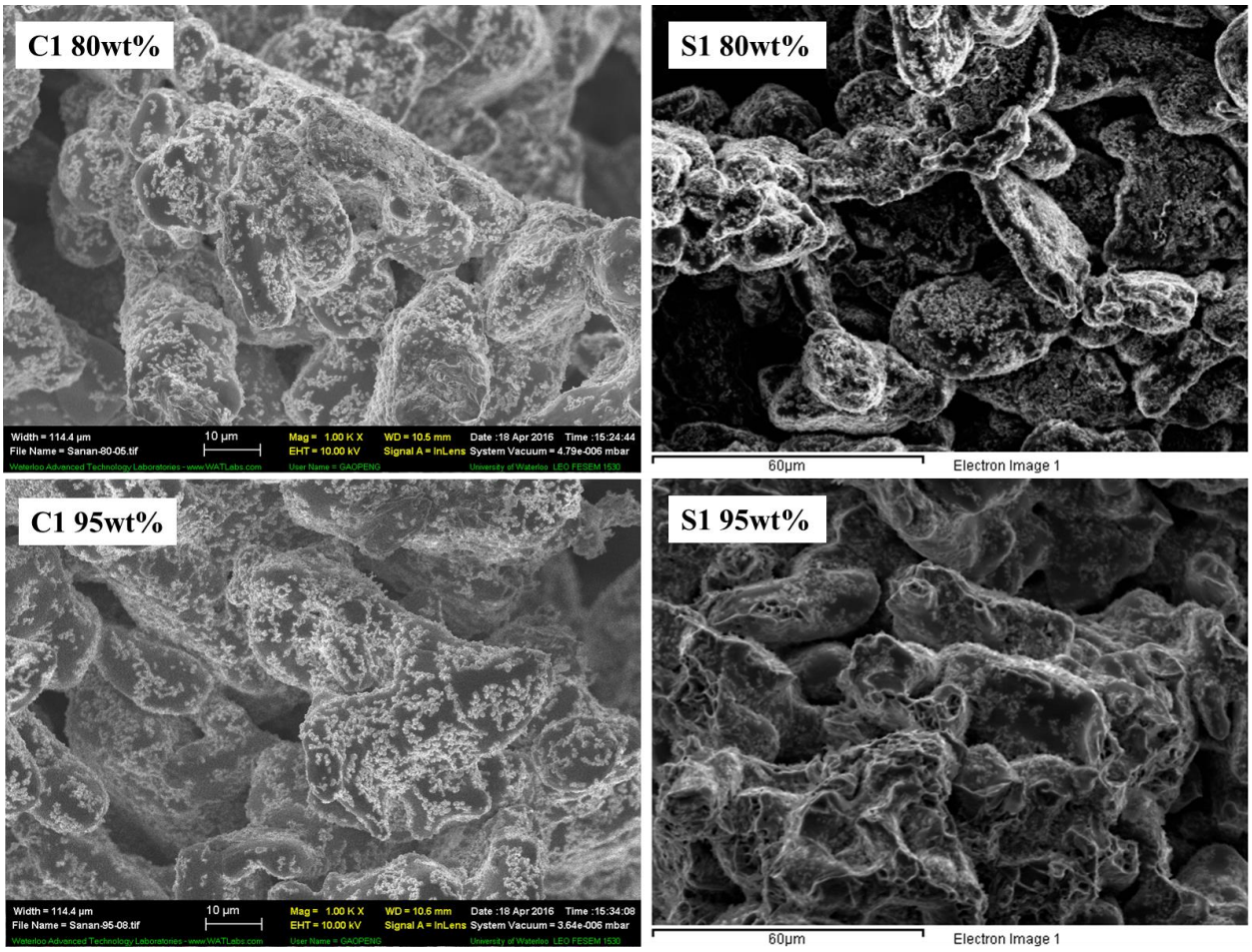

Figure 4-20 SEM of C1 and S1 with SS430L 80 and 95wt% samples.

Also SEM images were taken on polished surface of S1 95wt% that was used for the optical analysis in porosity measurements. Figure 4-21 shows the SEM and EDX image of the polished S1 95wt%. In Table 4-8, EDX chemical element analysis revealed that near the sintering neck, there is also higher content of Si and Cr of 4.58 and 40.63wt% present respectively. Si and Cr content decreases towards the inside of the particle which means that Si and Cr are more present on the surface level (sintering neck) in general and form oxide scale around the metallic substrate. Carbon content is also higher than the expected value (0.02 wt%) but the measurement environment was contaminated with carbon due to numerous use of carbon tapes and graphite coatings on samples.

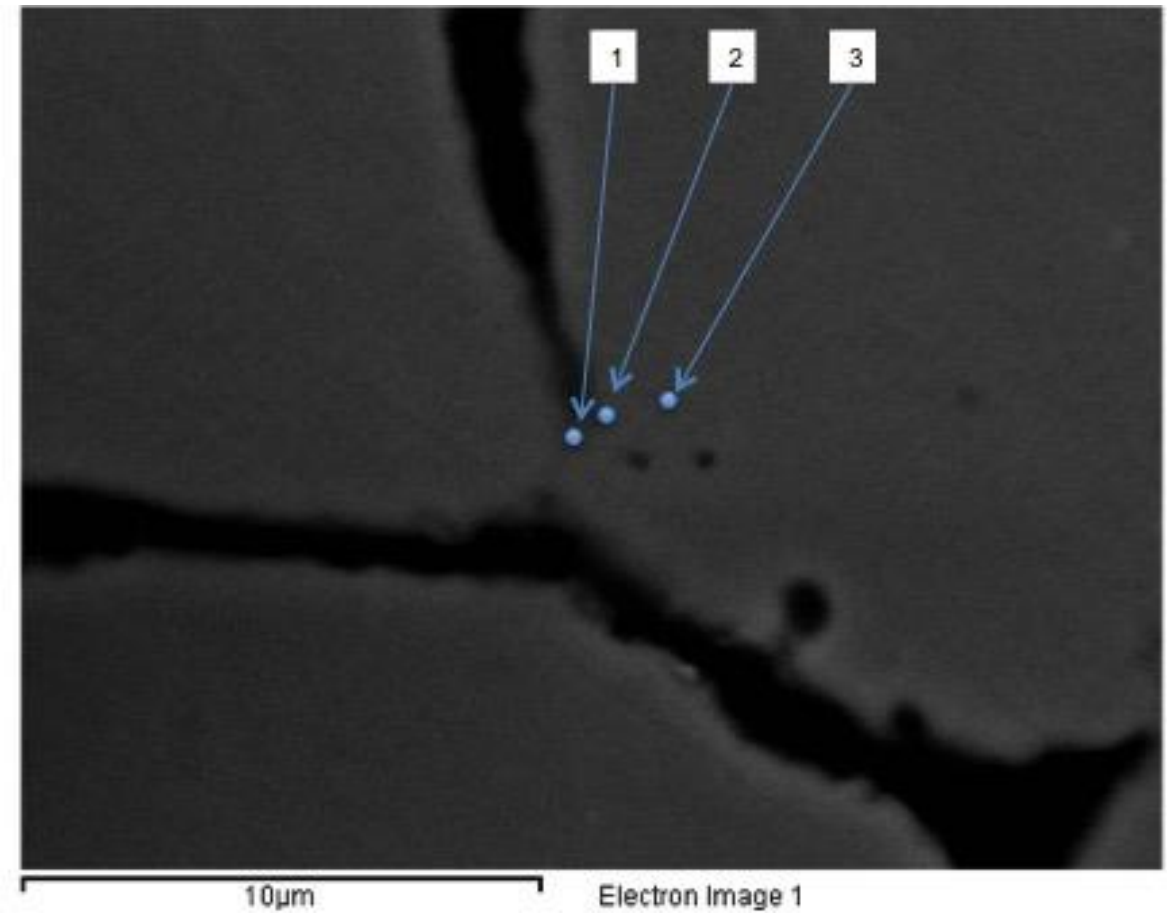

Figure 4-21 EDX analysis on polished S1-95wt% sample.

Table 4-8 EDX all element analysis in wt%

Spectrum	C(wt%)	O(wt%)	Si(wt%)	Cr(wt%)	Fe(wt%)	Total
1	9.22	2.05	4.58	40.63	45.53	100
2	4.78		1.49	18.97	74.76	100
3	4.02			14.76	81.22	100

Based on these results it was found that there were no differences in using the ceramic mortar versus the stainless steel mortar in terms of microstructures and the formation of oxide scales. The oxide scales composed of chromia oxide and silica oxide cover the entire surface of the porous metal support. During the sintering process, chromium and silicon tend to diffuse readily

towards the surface of the particles. These oxide scales are known to protect iron from oxidation. Due to this distinctive microstructure it is possible that the electronic conductivity measured in much lower value than the reference value. Oxide scales are known as poor electronic conductors and the sintered metal supports are covered with these scales. Thus the electronic conductivity is much lower than that of the pure stainless steel where oxide scales are not present.

Chapter 5 Conclusions

The aims of this thesis were:

1) Determine repeatable and appropriate fabrication method for the metal support layers and

2) Characterize the sintered metal supports to verify suitability for MSOFC application.

- In this study we investigated various solid loadings of SS430L contents to fabricate metal supports. In order to optimize the sintering profile, TGA analysis was conducted on the individual organics to determine a suitable burn-out temperature while limiting the oxidation of the metal. From these results, the use of graphite was determined to be not suitable as a pore former due to a high burn-out temperature of 700°C where the metal can be oxidized. Using the TGA, the oxidation behavior of the sintered metal support at various temperatures was examined. It was determined that an appropriate operating temperature for MSOFC is between 600-700°C to minimize oxidation.

- The effect of organics was studied to finalize the organics ratio and it was found that the organics ratio of PVB:DOP:PMMA=1:1:3 is the most suitable formula for fabricating flat disk-shaped metal supports without any deformation. Then the relative green density, the relative sintered density, change in mass before and after sintering of the metal support were investigated. From these results positive linear relationships were found between the relative densities and SS430L solid loadings as:

$$Rlative\ Green\ Density = 1.33(\pm 0.0285) * (SS430L\ wt\%) - 65.89(\pm 2.503)$$

$$Relative\ Sintered\ Density = 1.71(\pm 0.0957) * (SS430L\ wt\%) - 100.32(\pm 8.377)$$

- Porosity measurements quantified the porosity as a function of different SS430L solid loadings, and, as expected, showed that an increase in metal loading decreases the porosity. Furthermore, linear relationships between the porosity and the relative densities were determined.

$$Porosity = -0.0118\ (\pm 0.00089)(relative\ green\ density) + 1.0432\ (0.0452)$$

$$Porosity = -0.0094\ (\pm 0.00054)(\text{relative sintered density}) + 0.9069\ (0.0266)$$

- The effects of binder (PVB) and pore former (PMMA) were measured via porosity. It is shown that, as expected, an increase in PMMA content increases the porosity whereas an increase in PVB content decreases the porosity.
- The CTE measurements showed that differences in SS430Lwt% have minor effects on CTE values, although higher metal loadings seem to increase the CTE and a loading of 95wt% (C1-CTE1) leads to a CTE (12.2ppm/K) closest to that of SDC (12.7ppm/K). It was also found that there is shrinkage due to phase change of the metal from ferrite to austenite or delta phase at ~900-1000°C. The dilatometer measurements showed a decreasing slope of linear expansion between 900-1000°C. DSC results showed that there is a reversible energy release at the same temperature range of 900-1000°C confirming the phase change.
- The electronic conductivity measurement of the metal supports showed that the conductivity decreases as the temperature increases from 550 to 800°C. The highest conductivity was measured from 85-ceramic mortar sample with 64 S/cm at 550°C and decreased to 47/cm at 800°C.
- SEM images revealed microstructures of different SS430Lwt% samples and that there were no differences between the uses of the ceramic mortar vs. the stainless steel mortar. EDX analysis identified that there are oxide scales present all over the metal surface which are mainly silica oxide and chromia oxides. These components readily migrate to the surface during the sintering process and form a protective layer to prevent oxidation of iron, but at the same reduces the electronic conductivity of the metal support.

Chapter 6 Future work

Future work should involve two main parts:

The first one is to determine fabrication process of the complete cell with the metal support, anode, electrolyte, and cathode layers. For this process a vacuum slurry coating technique is proposed. Once the anode and electrolyte slurries are deposited on the metal support, it is co-sintered in reducing atmosphere to sinter and densify the electrolyte layer. Appropriate slurry compositions consisting of organics and solvents needs to be optimized to produce desired quality cells. After the co-sintering process cathode paste is applied on the sintered electrolyte side and can in-situ sintered inside the SOFC testing station.

The second part of the future work is performance testing of the entire cell. The same set-up as described in 3.3.6 can be used. For this experiment, the anode side receives hydrogen and/or potential hydrocarbon gases while the cathode side is in contact with air. Based on the performance testing, more results and analysis will be available and further improvements can be made.

References

Baek, S. W., Jeong, J., Kim, Y. M., Kim, J. H., Shin, S., & Bae, J. (2011). Metal-supported solid oxide fuel cells with barium-containing in-situ cathodes. *Solid State Ionics*, *192*(1), 387–393. http://doi.org/10.1016/j.ssi.2010.09.047

Blennow, P., Hjelm, J., Klemensø, T., Persson, Å. H., Ramousse, S., & Mogensen, M. (2011). Planar Metal-Supported SOFC with Novel Cermet Anode. *Fuel Cells*, *11*(5), 661–668. http://doi.org/10.1002/fuce.201100029

Blennow, P., Hjelm, J., Klemensø, T., Persson, Å., Srivastava, K. B. A. K., Frandsen, H. L., … Mogensen, M. (2009). Development of Planar Metal Supported SOFC with Novel Cermet Anode. *Journal of Chemical Information and Modeling* (Vol. 25, pp. 701–710). http://doi.org/10.1017/CBO9781107415324.004

Blennow, P., Hjelm, J., Klemenso, T., Ramousse, S., Kromp, A., Leonide, A., & Weber, A. (2011). Manufacturing and characterization of metal-supported solid oxide fuel cells. *Journal of Power Sources* (Vol. 196, pp. 7117–7125). http://doi.org/10.1016/j.jpowsour.2010.08.088

Blennow, P., Sudireddy, B. R., Persson, Å. H., Klemensø, T., Nielsen, J., & Thydén, K. (2013). Infiltrated SrTiO 3 :FeCr-based Anodes for Metal-Supported SOFC. *Fuel Cells*, *13*(4), 494–505. http://doi.org/10.1002/fuce.201200176

Fernández-González, R., Hernández, E., Savvin, S., Núñez, P., Makradi, A., Sabaté, N., … Ruiz-Morales, J. . (2014). A novel microstructured metal-supported solid oxide fuel cell. *Journal of Power Sources*, *272*, 233–238. http://doi.org/10.1016/j.jpowsour.2014.08.081

Franco, T., Brandner, M., Rüttinger, M., Kunschert, G., Venskutonis, A., & Sigl, L. S. (2009). Recent Development Aspects of Metal Supported Thin-Film SOFC T. *ECS Transactions* (Vol. 25, pp. 681–688). http://doi.org/10.1007/s13398-014-0173-7.2

Glasscock, J. A., Mikkelsen, L., Persson, Å. H., Pećanac, G., Malzbender, J., Blennow, P., … Hendriksen, P. V. (2013). Porous Fe21Cr7Al1Mo0.5Y metal supports for oxygen transport membranes: Thermo-mechanical properties, sintering and corrosion behaviour. *Solid State Ionics*, *242*, 33–44. http://doi.org/10.1016/j.ssi.2013.04.006

Hanifi, A. R., Torabi, A., Zazulak, M., Etsell, T. H., Yamarte, L., Sarkar, P., & Tucker, M. C. (2011). Improved redox and thermal cycling resistant tubular ceramic fuel cells. *ECS Transactions*, *35*(1), 409–418. http://doi.org/10.1149/1.3570016

Hui, R., Berghaus, J. O., Decès-Petit, C., Qu, W., Yick, S., Legoux, J.-G., & Moreau, C. (2009). High performance metal-supported solid oxide fuel cells fabricated by thermal spray. *Journal of Power Sources*, *191*(2), 371–376. http://doi.org/10.1016/j.jpowsour.2009.02.067

Hwang, C. S., Tsai, C. H., Hwang, T. J., Chang, C. L., Yang, S. F., & Lin, J. K. (2016). Novel Metal Substrates for High Power Metal-supported Solid Oxide Fuel Cells. *Fuel Cells*, (2), 244–251. http://doi.org/10.1002/fuce.201500216

Hwang, C. S., Tsai, C. H., Yu, J. F., Chang, C. L., Lin, J. M., Shiu, Y. H., & Cheng, S. W. (2011). High performance metal-supported intermediate temperature solid oxide fuel cells fabricated by atmospheric plasma spraying. *Journal of Power Sources*, *196*(4), 1932–1939. http://doi.org/10.1016/j.jpowsour.2010.10.029

J. Harrisa, and O. K. (2011). Performance of Metal-Supported Composite and Single-Phase Cathodes Based on LSCF and SSC J. Harris. *ECS Transactions* (Vol. 35, pp. 1927–1934).

Jablonski, P. D., & Sears, J. S. (2013). The impact of alloy chemistry on the formation of a silicon-rich subscale on two classes of ferritic steels. *Journal of Power Sources*, *228*, 141–150. http://doi.org/10.1016/j.jpowsour.2012.11.107

Jo, K. H., Kim, J. H., Kim, K. M., Lee, I. S., & Kim, S. J. (2015). Development of a new cost effective Fe-Cr ferritic stainless steel for SOFC interconnect. *International Journal of Hydrogen Energy*, *40*(30), 9523–9529. http://doi.org/10.1016/j.ijhydene.2015.05.125

Karczewski, J., Dunst, K. ., Jasinski, P., & Molin, S. (2015). High temperature corrosion and corrosion protection of porous Ni22Cr alloys. *Surface and Coatings Technology*, *261*, 385–390. http://doi.org/10.1016/j.surfcoat.2014.10.051

Klemenso, T., Nielsen, J., Blennow, P., Persson, A. ., Stegk, T., Hjalmarsson, P., … Ramousse, S. (2011). Development of Long-term Stable and High-performing Metal-supported SOFCs. *ECS Transactions* (Vol. 35, pp. 369–378).

Klemensø, T., Nielsen, J., Blennow, P., Persson, Å. H., Stegk, T., Christensen, B. H., & Sønderby, S. (2011). High performance metal-supported solid oxide fuel cells with Gd-doped ceria barrier layers. *Journal of Power Sources*, *196*(22), 9459–9466. http://doi.org/10.1016/j.jpowsour.2011.07.014

Knibbe, R., Wang, H.-J., Blennow, P., Thydén, K., Persson, Å. H., Mikkelsen, L., & Klemensø, T. (2013). Oxidation in ceria infiltrated metal supported SOFCs – A TEM investigation. *Journal of Power Sources*, *228*, 75–82. http://doi.org/10.1016/j.jpowsour.2012.11.051

Matus, Y. B., De Jonghe, L. C., Jacobson, C. P., & Visco, S. J. (2005). Metal-supported solid oxide fuel cell membranes for rapid thermal cycling. *Solid State Ionics*, *176*(5-6), 443–449. http://doi.org/10.1016/j.ssi.2004.09.056

Molin, S., Gazda, M., & Jasinski, P. (2011). Coatings for improvement of high temperature corrosion resistance of porous alloys. *Journal of the European Ceramic Society*, *31*(14), 2707–2710. http://doi.org/10.1016/j.jeurceramsoc.2011.02.007

Molin, S., Tolczyk, M., Gazda, M., & Jasinski, P. (2011). Stainless Steel/Yttria Stabilized Zirconia Composite Supported Solid Oxide Fuel Cell. *Journal of Fuel Cell Science and Technology*, *8*, 051019–1. http://doi.org/10.1115/1.4003994

Nielsen, J., Hjalmarsson, P., Hansen, M. H., & Blennow, P. (2014). Effect of low temperature in-situ sintering on the impedance and the performance of intermediate temperature solid oxide fuel cell cathodes. *Journal of Power Sources*, *245*, 418–428. http://doi.org/10.1016/j.jpowsour.2013.06.067

Nielsen, J., Klemensø, T., & Blennow, P. (2012). Detailed impedance characterization of a well performing and durable Ni:CGO infiltrated cermet anode for metal-supported solid oxide fuel cells. *Journal of Power Sources*, *219*, 305–316. http://doi.org/10.1016/j.jpowsour.2012.07.031

P. Blennow, T. Klemensø, Å. H. Persson, K. Brodersen, A. K. Srivastava B. R. Sudireddy, S. Ramousse, M. M. (2011). Metal-supported SOFC with Ceramic-based Anode. *ECS Transactions* (Vol. 35, pp. 683–692).

Rose, L., Kesler, O., Decès-Petit, C., Troczynski, T., & Maric, R. (2009). Characterization of Porous Stainless Steel 430 for Low- and Intermediate-Temperature Solid Oxide Fuel Cell (SOFC) Substrates. *International Journal of Green Energy*, *6*(6), 638–645. http://doi.org/10.1080/15435070903372510

Ruiz-Morales, J. C., Pe??a-Mart??nez, J., Canales-V??zquez, J., Marrero-L??pez, D., Savaniu, C., & N????ez, P. (2009). Cost-effective microstructural engineering of solid oxide fuel cell components for planar and tubular designs. *Journal of the American Ceramic Society*, *92*(1), 276–279. http://doi.org/10.1111/j.1551-2916.2008.02857.x

Ruiz-Morales, J. C., Pena-Martinez, J., Canales-Vazquez, J., Marrero-Lopez, D., Savaniu, C., & Nunez, P. (2010). Performance of a novel type of electrolyte-supported solid oxide fuel cell with honeycomb structure. *Journal of Power Sources*, *195*(2), 516–521. http://doi.org/10.1016/j.jpowsour.2009.08.017

Toor, S. ., & Croiset, E. (2015). C with hydrogen as fuel (4). Even with the use of doped oxides of cerium, mostly with samarium or gadolinium, the fabrication costs are high. Ceria needs a temperature of approximately 1400. *ECS Transactions* (Vol. 68, pp. 387–394).

Tucker, M. ., Cheng, L., & DeJonghe, L. . (2011). Cathode Contact Materials for Solid Oxide Fuel Cells. In *ECS Transactions* (Vol. 35, pp. 2625–2630). The Electrochemical Society. http://doi.org/10.1007/s13398-014-0173-7.2

Tucker, M. C. (2010). Progress in metal-supported solid oxide fuel cells: A review. *Journal of Power Sources*, *195*(15), 4570–4582. http://doi.org/10.1016/j.jpowsour.2010.02.035

Tucker, M. C., Lau, G. Y., Jacobson, C. P., DeJonghe, L. C., & Visco, S. J. (2007). Performance of metal-supported SOFCs with infiltrated electrodes. *Journal of Power Sources*, *171*(2), 477–482. http://doi.org/10.1016/j.jpowsour.2007.06.076

Tucker, M. C., Lau, G. Y., Jacobsona, C. P., DeJonghe, L. C., & Visco, S. J. (2007). Metal Supported SOFCs. *ECS Transactions* (Vol. 7, pp. 279–284).

Villarreal, I., Jacobson, C., Leming, A., Matus, Y., Visco, S., & De Jonghe, L. (2003). Metal-Supported Solid Oxide Fuel Cells. *Electrochemical and Solid-State Letters*, *6*(9), A178.

http://doi.org/10.1149/1.1592372

Waldbillig, D., & Kesler, O. (2009). Characterization of metal-supported axial injection plasma sprayed solid oxide fuel cells with aqueous suspension plasma sprayed electrolyte layers. *Journal of Power Sources*, *191*(2), 320–329. http://doi.org/10.1016/j.jpowsour.2009.01.084

Wang, Z., Berghaus, J. O., Yick, S., Decès-Petit, C., Qu, W., Hui, R., … Ghosh, D. (2008). Dynamic evaluation of low-temperature metal-supported solid oxide fuel cell oriented to auxiliary power units. *Journal of Power Sources*, *176*(1), 90–95. http://doi.org/10.1016/j.jpowsour.2007.10.002

Yang, S. F., Shie, Z. Y. J., Hwang, C. S., Tsai, C. H., Chang, C. L., & Huang, T. . (2015). Ni-Mo Porous Alloy Fabricated as Supporting Component For Metal-Supported Solid Oxide Fuel Cell and Cell Performance. *ECS Transactions*, *68*(1), 1849–1855.

Yoshida, H., & Inagaki, T. (2006). Effects of additives on the sintering properties of samaria-doped ceria. *Journal of Alloys and Compounds*, *408-412*(December 2004), 632–636. http://doi.org/10.1016/j.jallcom.2004.12.155

Appendix 1: Statistical Analysis

Statistical analysis was performed on the average green densities of different SS430L solid loadings. For this analysis ANOVA-single factor test, t-test with unequal variances, and F-test with two sample variances were conducted. ANOVA-test was used to determine if there are any significant differences in the means of the average green densities between the three batches: C1, C2, and S1. A null hypothesis is that all three means are equal meaning that the average green densities of C1, C2, and S1 are equal. An alternative hypothesis is that at least one of the means is different. ANOVA table computes F-value, F-critical, and P-values. If F >F-critical than we can reject the null hypothesis and conclude that at least one of the means is different. Similarly, if P-value < significance level alpha value (0.05) then we can reject the null hypothesis. Significance level or alpha value is determined by the users and/or circumstances and 0.05 or 5% is most commonly used. However, ANOVA results do not show which means are different from one another. So, once the ANOVA test shows that the means are different, T-test is conducted to determine which means are different from one another. T-test can test the null hypothesis that the means of two batches are equal. Basically ANOVA-test is used when there are 3 and more means to compare whereas T-test is used to compare only 2 means. T-test computes t-Stat and t-Critical two-tail. If t-Stat < -t Critical two-tail or t Stat > t Critical two-tail, we reject the null hypothesis. For example if the results of C1 and C2 t-test showed t-Stat < -t Critical two-tail or t Stat > t Critical two-tail, then the average green densities between C1 and C2 are statistically different. Table A-1 shows the results of ANOVA-table for different SS430L solid loadings: 80, 85, 87, 90, and 95wt%.

Table A-1 Statistical analysis (ANOVA and T-test) of the green densities for different SS430L solid loadings

80 Solid Loading

SUMMARY

Groups	*Count*	*Sum*	*Average*	*Variance*	*Standard Deviation*
C1	6.0000	18.6690	3.1115	0.0002	0.0126
C2	6.0000	18.8121	3.1354	0.0042	0.0649
S1	6.0000	18.9265	3.1544	0.0230	0.1517

ANOVA

Source of Variation	*SS*	*df*	*MS*	*F*	*P-value*	*F crit*
Between Groups	0.0055	2.0000	0.0028	0.3039	0.7424	3.6823
Within Groups	0.1370	15.0000	0.0091			
Total	0.1425	17.0000				

F<F-Critical There is no difference in the means

P > 0.05 no difference in the means

85 Solid Loading

SUMMARY

Groups	*Count*	*Sum*	*Average*	*Variance*	*Standard Deviation*
C1	6.0000	20.9631	3.4938	0.0017	0.0417
C2	6.0000	21.5378	3.5896	0.0001	0.0118
S1	6.0000	22.0875	3.6812	0.0009	0.0303

ANOVA

Source of Variation	*SS*	*df*	*MS*	*F*	*P-value*	*F crit*
Between Groups	0.1054	2.0000	0.0527	56.6310	0.000000102	3.6823
Within Groups	0.0140	15.0000	0.0009			

	0.119					
Total	3	17.0000				

Results: F> F-crit There is difference in the means

P < 0.05 there is difference in the means

87 Solid Loading

SUMMARY

Groups	*Count*	*Sum*	*Average*	*Variance*	*Standard Deviation*
C1	6.0000	22.6493	3.7749	0.0142	0.1193
C2	6.0000	22.5610	3.7602	0.0066	0.0811
S1	6.0000	23.5574	3.9262	0.0095	0.0974

ANOVA

Source of Variation	*SS*	*df*	*MS*	*F*	*P-value*	*F crit*
Between Groups	0.1014	2.0000	0.0507	5.0199	0.0214	3.6823
Within Groups	0.1515	15.0000	0.0101			
Total	0.2529	17.0000				

Results: F> F-crit There is difference in the means

P < 0.05 there is difference in the means

90 Solid Loading

SUMMARY

Groups	*Count*	*Sum*	*Average*	*Variance*	*Standard Deviation*
C1	6.0000	24.2810	4.0468	0.0037	0.0605
C2	6.0000	24.5133	4.0855	0.0028	0.0530
S1	6.0000	25.4290	4.2382	0.0048	0.0691

ANOVA

Source of Variation	*SS*	*df*	*MS*	*F*	*P-value*	*F crit*
Between Groups	0.1224	2.0000	0.0614	16.3942	0.0002	3.6823

	8					
	0.056					
Within Groups	2	15.0000	0.0037			
	0.179					
Total	0	17.0000				

Results: F> F-crit There is difference in the means

P < 0.05 there is difference in the means

95 Solid Loading

SUMMARY

Groups	*Count*	*Sum*	*Average*	*Variance*	*Standard Deviation*
C1	6.0000	27.6914	4.6152	0.0038	0.0620
C2	6.0000	27.9802	4.6634	0.0058	0.0759
S1	6.0000	28.0864	4.6811	0.0046	0.0680

ANOVA

Source of Variation	*SS*	*df*	*MS*	*F*	*P-value*	*F crit*
Between Groups	0.0139	2.0000	0.0070	1.4677	0.2617	3.6823
Within Groups	0.0712	15.0000	0.0047			
Total	0.0851	17.0000				

F<F-Critical Threre is no difference in the means

P > 0.05 no difference in the means

Based on the ANOVA results, compositions 85, 87, and 90 solid loadings showed that there are differences in the means of the green density values between C1, C2, and S1 batches. Thus T-tests were performed on 85, 87, and 90 green density values to determine which means are different from one another. Table 5-2 shows the T-test results of 85, 87, and 90.

Table A-2 T-test results of 85, 87, and 90 wt% solid loadings on the green densities

85 Solid Loading

	C1	*C2*		*C2*	*S1*		*C1*	*S1*
t Stat	-5.4185		t Stat	-6.9106		t Stat	-8.9125	
P(T<=t) two-tail	0.0016		P(T<=t) two-tail	0.0005		P(T<=t) two-tail	0.0000	
t Critical two-tail	2.4469		t Critical two-tail	2.4469		t Critical two-tail	2.2622	
There is no difference in between the means C1 and C2			Means of C2 and S1 are different			Means of C1 and S1 are different		

87 Solid Loading

	C1	*C2*		*C2*	*S1*		*C1*	*S1*
t Stat	0.2498		t Stat	-3.2101		t Stat	-2.4071	
P(T<=t) two-tail	0.8083		P(T<=t) two-tail	0.0093		P(T<=t) two-tail	0.0369	
t Critical two-tail	2.2622		t Critical two-tail	2.2281		t Critical two-tail	2.2281	
There is no difference in between the means C1 and C2			Means of C2 and S1 are different			Means of C1 and S1 are different		

90 Solid Loading

	C1	*C2*		*C2*	*S1*		*C1*	*S1*
t Stat	-1.1794		t Stat	-4.2950		t Stat	-4.2950	
P(T<=t) two-tail	0.2655		P(T<=t) two-tail	0.0020		P(T<=t) two-tail	0.0020	
t Critical two-tail	2.2281		t Critical two-tail	2.2622		t Critical two-tail	2.2622	
There is no difference in between the means C1 and C2			Means of C2 and S1 are different			Means of C1 and S1 are different		

Based on the T-test results the difference in the green density means occur between C2 and S1 samples and between C1 and S1 samples. There is no difference in green density means between C1 and C2 samples for all 85, 87, and 90 wt% solid loadings. This implies that the use of ceramic mortar and stainless steel mortar can create statistical difference in the green density values even though on the graph Figure 4-5 shows that all values are similar to each other for C1, C2, and S1.

Appendix 2: ASTM Standard

Designation: C373 – 88 (Reapproved2006)

Standard Test Method for Water Absorption, Bulk Density, Apparent Porosity, and Apparent Specific Gravity of Fired Whiteware Products[1]

This standard is issued under the fixed designation C373; the number immediately following the designation indicates the year of original adoption or, in the case of revision, the year of last revision. A number in parentheses indicates the year of last reapproval. A superscript epsilon (ε) indicates an editorial change since the last revision or reapproval.

1. Scope

1.1 This test method covers procedures for determining water absorption, bulk density, apparent porosity, and apparent specific gravity of fired unglazed whiteware products.

1.2 *This standard does not purport to address all of the safety concerns, if any, associated with its use. It is the responsibility of the user of this standard to establish appropriate safety and health practices and determine the applicability of regulatory limitations prior to use.*

2. Significance and Use

2.1 Measurement of density, porosity, and specific gravity is a tool for determining the degree of maturation of a ceramic body, or for determining structural properties that may be required for a given application.

3. Apparatus and Materials

3.1 *Balance,* of adequate capacity, suitable to weigh accurately to 0.01 g.

3.2 *Oven,* capable of maintaining a temperature of 150 ± 5°C (302 ± 9°F).

3.3 *Wire Loop, Halter, or Basket* , capable of supporting specimens under water for making suspended mass measurements.

3.4 *Container*—A glass beaker or similar container of such size and shape that the sample, when suspended from the balance by the wire loop, specified in 3.3, is completely immersed in water with the sample and the wire loop being completely free of contact with any part of the container.

3.5 *Pan,* in which the specimens may be boiled.

3.6 *Distilled Water.*

4. Test Specimens

4.1 At least five representative test specimens shall be selected. The specimens shall be unglazed and shall have as much of the surface freshly fractured as is practical. Sharp edges or corners shall be removed. The specimens shall contain no cracks. The individual test specimens shall weigh at least 50 g.

5. Procedure

5.1 Dry the test specimens to constant mass (Note 1) by heating in an oven at 150°C (302°F), followed by cooling in a desiccator. Determine the dry mass, *D*, to the nearest 0.01 g.

NOTE 1—The drying of the specimens to constant mass and the determination of their masses may be done either before or after the specimens have been impregnated with water. Usually the dry mass is determined before impregnation. However, if the specimens are friable or evidence indicates that particles have broken loose during the impregnation, the specimens shall be dried and weighed after the suspended mass and the saturated mass have been determined, in accordance with 5.3 and 5.4. In this case, the second dry mass shall be used in all appropriate calculations.

5.2 Place the specimens in a pan of distilled water and boil for 5 h, taking care that the specimens are covered with water at all times. Use setter pins or some similar device to separate the specimens from the bottom and sides of the pan and from each other. After the 5-h boil, allow the specimens to soak for an additional 24 h.

5.3 After impregnation of the test specimens, determine to the nearest 0.01 g the mass, *S*, of each specimen while suspended in water. Perform the weighing by placing the specimen in a wire loop, halter, or basket that is suspended from one arm of the balance. Before actually weighing, counterbalance the scale with the loop, halter, or basket in place and immerse in water to the same depth as is used when the specimens are in place. If it is desired to determine only the percentage of water absorption, omit the suspended mass operation.

5.4 After the determination of the suspended mass or after impregnation, if the suspended mass is not determined, blot each specimen lightly with a moistened, lint-free linen or cotton cloth to remove all excess water from the surface, and determine the saturated mass, *M*, to the nearest 0.01 g. Perform the blotting operation by rolling the specimen lightly on the wet cloth, which shall previously have been saturated with water and then pressed only enough to remove such water as will drip from the cloth. Excessive blotting will introduce error

[1] This test method is under the jurisdiction of ASTM Committee C21 on Ceramic Whitewares and Related Products and is the direct responsibility of Subcommittee C21.03 on Methods for Whitewares and Environmental Concerns.

Current edition approved Feb. 15, 2006. Published February 2006. Originally approved in 1955. Last previous edition approved in 1999 as C373 – 88 (1999). DOI: 10.1520/C0373-88R06.

by withdrawing water from the pores of the specimen. Make the weighing immediately after blotting, the whole operation being completed as quickly as possible to minimize errors caused by evaporation of water from the specimen.

6. Calculation

6.1 In the following calculations, the assumption is made that 1 cm^3 of water weighs 1 g. This is true within about 3 parts in 1000 for water at room temperature.

6.1.1 Calculate the exterior volume, V, in cubic centimetres, as follows:

$$V = M - S \quad (1)$$

6.1.2 Calculate the volumes of open pores V_{OP}, and impervious portions V_{IP}, in cubic centimetres as follows:

$$V_{OP} = M - D \quad (2)$$

$$V_{IP} = D - S \quad (3)$$

6.1.3 The apparent porosity, P, expresses, as a percent, the relationship of the volume of the open pores of the specimen to its exterior volume. Calculate the apparent porosity as follows:

$$P = [(M - D)/V] \times 100 \quad (4)$$

6.1.4 The water absorption, A, expresses as a percent, the relationship of the mass of water absorbed to the mass of the dry specimen. Calculate the water absorption as follows:

$$A = [(M - D)/D] \times 100 \quad (5)$$

6.1.5 Calculate the apparent specific gravity, T, of that portion of the test specimen that is impervious to water, as follows:

$$T = D/(D - S) \quad (6)$$

6.1.6 The bulk density, B, in grams per cubic centimetre, of a specimen is the quotient of its dry mass divided by the exterior volume, including pores. Calculate the bulk density as follows:

$$B = D/V \quad (7)$$

7. Report

7.1 For each property, report the average of the values obtained with at least five specimens, and also the individual values. Where there are pronounced differences among the individual values, test another lot of five specimens and, in addition to individual values, report the average of all ten determinations.

8. Precision and Bias

8.1 This test method is accurate to ±0.2 % water absorption in interlaboratory testing when the average value recorded by all laboratories is assumed to be the true water absorption. The precision is approximately ±0.1 % water absorption on measurements made by a single experienced operator.

9. Keywords

9.1 apparent porosity; apparent specific gravity; bulk density; fired whiteware products; water absorption